Development of Λ baryons reconstruction and its application to the search for a stable hexaquark at Belle II

Dissertation submitted
for the award of the title
"Doctor of Natural Sciences"
to the
Faculty of Physics, Mathematics and
Computer Science (FB 08)
of the Johannes Gutenberg-Universität Mainz

Bianca Scavino
born in Moncalieri (TO)

Mainz, May 2022

Development of Λ baryons reconstruction and its application to the search for a stable hexaquark at Belle II

1. Reviewer:
2. Reviewer:

Date of the defense: July, 27$^{\text{th}}$ 2022

Bianca Scavino
Belle II Collaboration
Institut für Kernphysik
Johannes Gutenberg-Universität
Johann-Joachim-Becher-Weg 45
D-55128 Mainz
bscavino@uni-mainz.de

JOHANNES GUTENBERG UNIVERSITÄT MAINZ

JG|U

Belle II

Claude Monet, *Water Lilies*
National Museum of Western Art, Tokyo

Acknowledgements

Abstract

QCD-motivated models for hadrons predict a wide variety of exotic hadrons, with structures more complex than the quark-antiquark mesons and the three-quark baryons of the ordinary hadron classification. Among these, one of the most intriguing cases refers to the H dibaryon, an elusive six-quark state with the quark content of two Λ baryons first suggested by R. L. Jaffe in 1977. The search for a stable double strange hexaquark, which, in recent years, was put forward to also be a dark matter candidate, is part of the Belle II physics program. In the coming years, a fraction of the Belle II data taking period will be dedicated to run at the energy of the $\Upsilon(3S)$ resonance. This $b\bar{b}$ resonance decays primarily via three gluons, in which $s\bar{s}$ quark pairs are produced with roughly the same probability as $u\bar{u}$ and $d\bar{d}$ pairs, making it particularly well suited for searches for multiquark states with nonzero strangeness.

This thesis describes a feasibility study for the search for a stable double strange six-quark state S produced in $\Upsilon(3S)$ decays, $\Upsilon(3S) \to S\Lambda\Lambda n\pi_s$ (with n = 0,2, 4, 6, and 8). The predictions obtained for the channel with n=0 are compared with an existing result from the BaBar collaboration, while the other channels represent a novel measurement. In order to obtain optimal results, an integral part of the work is the optimization of the Belle II tracking package for displaced vertices with a focus on Λ baryon reconstruction, a key element in the stable hexaquark analysis. After the optimization, the algorithms and selections developed for Λ baryons were extensively tested using Belle II data collected at the $\Upsilon(4S)$ resonance. Finally, a look at the future is taken. Given that the beam background level measured at Belle II in the first data taking periods turned out to be higher than initial estimates, the possible effect of increased background on performance deterioration, both on tracking in general and on the hexaquark analysis in particular, is assessed and discussed in detail.

The work presented in this thesis is intended to prepare a measurement where the tools and the analysis procedures developed, as well as the critical points observed, will be used on the $\Upsilon(3S)$ Belle II data to set a new limit on the possible observation of such an exotic state.

Contents

List of Figures

List of Tables

Acronyms

ARICH Aerogel Ring-Imaging CHerenkov

BC Best Candidate

BW backward

CDC Central Drift Chamber

CI Credibility Interval

CKF Combinatorial Kalman Filter

CL Confidence Level

DAF Deterministic Annealing Filter

DEPFET DEPleted Field Effect Transistor

DM Dark Matter

DR Damping Ring

DSSD Double-sided Silicon Strip Detector

ECL Electromagnetic CaLorimeter

EFT Effective Field Theory

FastBDT Fast Boosted Decision Tree

FOM Figure Of Merit

FW forward

FWHM Full Width Half Maximum

HAPD Hybrid Avalanche Photo-Detector

HER High-Energy Ring

IP Interaction Point

KLM K_L and Muon detector

LER Low-Energy Ring

linac linear accelerator

LQCD Lattice Quantum ChromoDynamics

MC Monte Carlo

MCP Micro-Channel Plate

PID Particle IDentification

PMT PhotoMultiplier Tube

POCA Point Of Closest Approach

PXD PiXel Detector

QCD Quantum ChromoDynamics

QED Quantum ElectroDynamics

QFT Quantum Field Theory

QM Quantum Mechanics

ROE Rest Of Event

RPC Resistive Plate Chamber

RT RecoTrack

SiPM Silicon PhotoMultiplier

SM Standard Model

SVD Silicon Vertex Detector

TOP Time Of Propagation

UL upper limit

VXD VerteX Detector

Considerate la vostra semenza:
fatti non foste a viver come bruti,
ma per seguir virtute e canoscenza.

(Consider your origin:
you were not made to live as brutes,
but to follow virtue and knowledge.)

Dante Alighieri

1 Preface

Since ancient times, curiosity and thirst for knowledge have always been characteristics of the human species. In all spheres of culture, from art to literature, as well as philosophy and science, the ability to wonder, the thirst for knowledge, and the courage to challenge the unknown have driven mankind to overcome the limits set by convention and always push towards new horizons. Many discoveries in science, technology, and medicine in the past centuries have completely revolutionized our understanding of the world and our lifestyle.

For much of the history of the natural sciences people have contemplated the true nature of matter. In this context, this thirst for knowledge has been the thread that led mankind over the centuries from the original concept of *atom* as a fundamental, indestructible particle (Democritus, 5th century BC) to the postulation of the Standard Model as we know it today (mid-1970s). All everyday objects that can be touched are ultimately composed of *atoms* in their modern meaning, i.e. the smallest unit of ordinary matter that forms a chemical element — which are not indivisible but composed of various subatomic particles. To date, our knowledge on the subject is all but complete, and there are numerous questions still waiting to be answered.

Until few years ago, despite being no obvious reason for composite subatomic particles to be confined solely to the states in which they commonly occur, namely

standard mesons and baryons, there was no experimental evidence for exotic states, i.e. hadrons with an unusual number or species of components. The discovery of these exotic particles, particularly successful in the last few years [1–3], together with the measurement of their properties, continues to provide important information for testing the limits of the model we use to describe our world and, once more, pushes our knowledge towards new horizons. This thesis is embedded in this framework: the search for an exotic state, an hexaquark, i.e. a hypothetical particle composed of six quarks, in the context of the particle physics experiment Belle II. The work can be divided in two main parts: the optimization of the Belle II tracking package for displaced vertices with a focus on Λ baryon reconstruction; and the subsequent sensitivity studies for the search for a stable double strange six-quark state using these improved tools. The Λ play a key role in the stable hexaquark analysis. This work is intended to prepare a measurement where the tools and the analysis procedures developed, as well as the critical points observed, will be used on the Belle II data to set a new limit on the possible observation of such an exotic state.

After a general introduction focusing on strongly interacting systems and hadron classification in Chapter 2, Chapter 3 presents a review — both from a theoretical and an experimental point of view — on the main topic of the thesis, the exotic double strange six-quark state *uuddss*. Chapter 4 describes the Belle II experiment. Chapter 5 provides details about the Belle II tracking software and the reconstruction of charged tracks, introducing the challenges it has to deal with and its performance in simulation. The first part of Chapter 6 describes the algorithm for the reconstruction of displaced vertices and its performance, while the second part is devoted to the description of an optimized selection for Λ baryons. Chapter 7 represents the central part of the thesis: it presents a sensitivity study for the search of a stable double strange six-quark at the Belle II experiment. Chapter 8 is devoted to test the displaced vertices (more specifically Λ baryons) reconstruction performance in data. Chapter 9 attempts to project the hexaquark analysis into the future, describing possible challenges and perspectives once the needed dataset will be collected. Finally, Chapter 10 summarizes the procedures and the results presented in the dissertation.

2

Strongly interacting systems

The strong interaction is one of the four known fundamental forces, the others being the electromagnetic, the weak, and the gravitational forces. It is responsible for binding together quarks, fundamental constituents of matter, within a nucleon; on a larger scale, the same interaction is responsible for the formation of atomic nuclei, binding together protons and neutrons. This latter effect, known as nuclear force or residual strong force, is nothing other than the residuum from the strong interaction between quarks and the elementary particles acting as exchange particles between them, gluons.

In the broader depiction of all the fundamental constituents of nature and their interactions, the strong force expounded by Quantum ChromoDynamics (QCD) is described together with the electroweak interaction in the Standard Model (SM). After a brief overview of the SM in Section 2.1, the rest of the chapter will be devoted to introducing some key concepts of QCD (Section 2.2). A general introduction to the theory will be given in Section 2.2.1; Section 2.2.2 will summarize existing nonperturbative QCD approaches, briefly presenting methods that will be used in the rest of the dissertation. Finally, Section 2.2.3 will be devoted to present the classification of strongly interacting particles.

In this chapter the natural units $\hbar = c = 1$ are used for convenience. The value of charge is indicated in units of e, the elementary charge.

2.1 Introduction to the Standard Model

The SM of elementary particles is the theory that currently best describes the fundamental constituents of matter and their interactions. It includes three of the four fundamental forces that govern the universe, leaving out gravity from the picture. Although it has demonstrated huge successes in providing experimental predictions, it leaves some phenomena unexplained — such as dark matter or the baryon asymmetry — and thus it falls short when it comes to be a complete theory of fundamental interactions.

According to the SM, matter is composed of fermions, spin-$\frac{1}{2}$ particles satisfying the Fermi-Dirac statistics [4,5] and the Pauli exclusion principle [6]. Fermions are further classified as leptons and quarks. Charged leptons (electron e, muon μ, and tau τ) interact both electromagnetically and weakly, while neutral leptons, called neutrinos (ν_e, ν_μ, ν_τ) interact only weakly. In total there are six types of leptons that can be organized in three generations of charged-neutral doublets:

$$\begin{pmatrix} e \\ \nu_e \end{pmatrix}, \qquad \begin{pmatrix} \mu \\ \nu_\mu \end{pmatrix}, \qquad \begin{pmatrix} \tau \\ \nu_\tau \end{pmatrix}. \tag{2.1}$$

Quarks are the fundamental constituents of hadrons, the strongly interacting particles. Unlike leptons, they carry color charge, which causes them to engage in the strong interaction as well. As in the case for leptons, there are a total of six quark types (also known as flavors) divided in up-type (u, c, t), with electric charge equal to $\frac{2}{3}$, and down-type (d, s, b), with electric charge equal to $-\frac{1}{3}$. Also in the case of quarks, a natural classification in doublets is possible:

$$\begin{pmatrix} u \\ d \end{pmatrix}, \qquad \begin{pmatrix} c \\ s \end{pmatrix}, \qquad \begin{pmatrix} t \\ b \end{pmatrix}. \tag{2.2}$$

The value of the mass increases among generations from left to right in Eq. (2.1) and Eq. (2.2) for both leptons and quarks. For every fermion in the SM there is a corresponding antiparticle. Antileptons and antiquarks differ from the corresponding leptons and quarks only in some of the quantum numbers that have equal magnitude but opposite sign.

Interactions between particles are modeled as the exchange of gauge bosons of the theory. In the SM the gauge bosons, having spin equal to 1, are vector bosons, and obey to the Bose-Einstein statistics [7]. There are four types of gauge bosons: photon, Z, W, and gluons. The photon (γ), is the massless boson that mediates the electromagnetic force. It interacts with all charged particles.

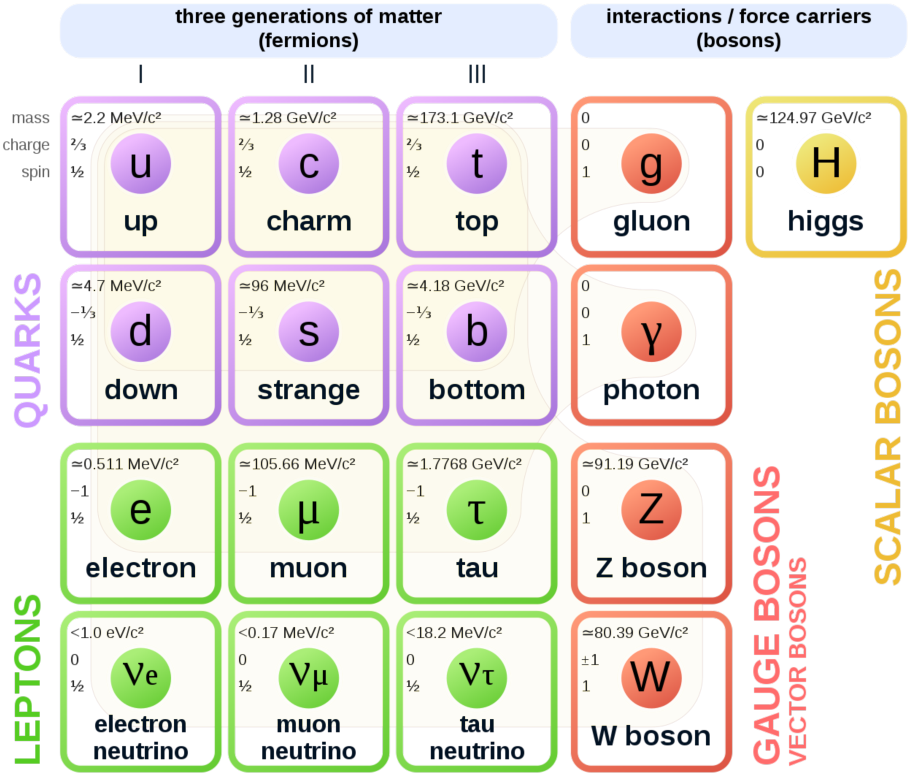

Figure 2.1: Elementary particles of the SM [10]. For each particle, mass, charge, spin, and name are given. For fermions, the mass hierarchy goes from left (lighter particles) to right (heavier particles).

Photons themselves do not carry electric charge, so they do not self-interact. W^+, W^- and Z^0 are the three massive bosons mediating the weak interaction. Gluons (g) are massless bosons that mediate the strong interaction, and they exist in 8 different color states. Gluons carry color charge, so unlike photons they can interact with themselves. All the massive particles in the SM acquire mass through a spontaneous symmetry breaking and the interaction with the spin-0 Higgs boson, the only scalar boson provided for in the SM [8, 9]. Figure 2.1 represents the 17 fundamental particles just described (12 fermions and 5 bosons) that constitute the SM, and reports their main properties as well: mass, charge, and spin.

Mathematically speaking, the SM is a non-abelian Quantum Field Theory (QFT) based on the gauge group of symmetry:

$$U(1)_Y \otimes SU(2)_L \otimes SU(3)_c, \tag{2.3}$$

where Y denotes the hypercharge, L the chiral component and c the color charge. The model includes a unified description of electromagnetic and weak interactions

within the electroweak theory, which possesses the symmetry group $U(1)_Y \otimes SU(2)_L$, and the theory of QCD, describing the strong interaction phenomena and possessing symmetry group $SU(3)_c$. The $U(1)_Y \otimes SU(2)_L$ subgroup gets broken down to the $U(1)_{EM}$ subgroup of Quantum ElectroDynamics (QED) thanks to the Higgs mechanism, leading to the massive W and Z bosons mediating the weak interaction.

A comprehensive review of the SM can be found in Ref. [11].

2.2 Quantum ChromoDynamics

2.2.1 Basic concepts

QCD is the gauge field theory that describes the strong interactions of colored quarks and gluons, and it is based on the gauge group $SU(3)_c$, the Special Unitary group in 3 complex dimensions. The three degrees of freedom of the symmetry group were historically labeled as *color charge* in analogy to the three colors used in the RGB additive color model: red, green, and blue.

Each flavor of quark belongs to the fundamental representation (**3**) and contains a triplet of fields, ψ. The antiquark field belongs to the complex conjugate representation ($\bar{\mathbf{3}}$) and contains as well a triplet of fields, $\bar{\psi}$. The two fields can be written as:

$$\psi = \begin{pmatrix} \psi_1 \\ \psi_2 \\ \psi_3 \end{pmatrix}, \qquad \bar{\psi} = \begin{pmatrix} \bar{\psi}_1^* \\ \bar{\psi}_2^* \\ \bar{\psi}_3^* \end{pmatrix}. \tag{2.4}$$

The gauge boson of the theory, the gluon, contains an octet of fields and belongs to the adjoint representation (**8**). A common way to represent it is making use of the Gell-Mann matrices λ_a:

$$\mathbf{A}_\mu = A_\mu^a \lambda_a. \tag{2.5}$$

The color charge of each of these fields is fully specified by their representations. Quarks can assume one of the three values or color charges (red, green, or blue); antiquarks can take one of the three anticolors (antired, antigreen, or antiblue). Gluons belong to the octet obtained combining one color and one anticolor charge, in a superposition of states given by the Gell-Mann matrices. No singlet gluon exists, being QCD based on $SU(3)_c$.

The QCD lagrangian, determining the dynamics of quarks and gluons, can be

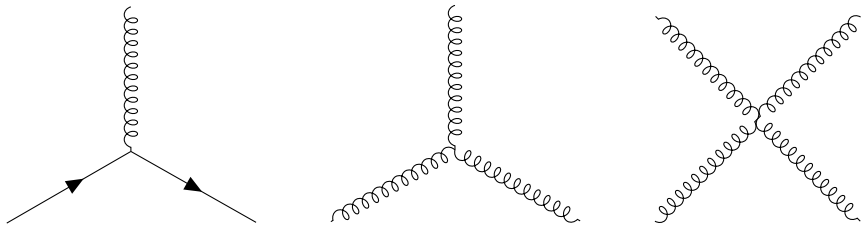

Figure 2.2: The three physical QCD interaction vertices: a quark may emit/absorb a gluon; a gluon may emit/absorb a gluon; two gluons may directly interact. The solid lines represent quarks, and the curly lines represent gluons.

written as:

$$\mathcal{L}_{\text{QCD}} = \sum_{quarks} \bar{\psi}_i^a \left[i \left(\gamma^\mu D_\mu\right)_{ij}^{ab} - m\,\delta_{ij}\delta^{ab} \right] \psi_j^b - \frac{1}{4} G_{\mu\nu}^a G_a^{\mu\nu}, \tag{2.6}$$

where γ^μ are the Dirac matrices, D_μ represents the gauge covariant derivative, and $G_{\mu\nu}^a$ represents the gauge invariant gluon field strength tensor. In the notation used here, the color charge is represented by roman indices a, b, c, while i, j represent the Dirac spin indexes. In QCD, the gauge covariant derivative is defined as:

$$D_\mu := \partial_\mu - i\frac{g_s}{2} G_\mu^\alpha \lambda_\alpha, \tag{2.7}$$

where g_s is the coupling constant of the strong interaction. It is common in QCD, in analogy to QED, to use the following notation:

$$\alpha_s(\mathcal{Q}^2) \equiv \frac{g_s^2(\mathcal{Q}^2)}{4\pi}, \tag{2.8}$$

defining the strong coupling constant α_s, dependent on the momentum transfer $\mathcal{Q}$. The gluon field strength tensor is given by:

$$G_{\mu\nu}^a = \partial_\mu \mathcal{A}_\nu^a - \partial_\nu \mathcal{A}_\mu^a + g_s f^{abc} \mathcal{A}_\mu^b \mathcal{A}_\nu^c, \tag{2.9}$$

with f^{abc} being the structure constants of SU(3).

According to the rules of QFT, and the associated Feynman diagrams, the QCD Lagrangian in Eq. (2.6) gives rise to three physical [1] interaction vertices, shown in Fig. 2.2: a quark may emit (or absorb) a gluon, a gluon may emit (or absorb) a gluon, and two gluons may directly interact. The associated interaction terms are all controlled by the coupling parameter of the theory: the three-line vertices are proportional to g_s, while the four-lines vertex is proportional to g_s^2.

[1] In this context, Faddeev–Popov ghost fields [12] and their effects are not taken into account.

Despite its fairly simple structure, the QCD lagrangian in Eq. (2.6) has a very rich dynamical content. In particular, the non-abelian character of the color field has profound consequences for the strong force: it becomes strong at low energy (or equivalently at long distance), and weak at high energy (or short distance). Such behavior gives rise to the two outstanding properties of QCD: asymptotic freedom and color confinement. The weakness of the color force at high energy is the responsible for asymptotic freedom, or in other words for the interactions between quarks and gluons to become asymptotically weaker as the energy scale increases, and provides an explanation for the quasi-free behavior of strongly interacting particles in the parton model of hadrons. Naively, asymptotic freedom can be understood as the net result of two opposite effects in the vacuum: color charge screening, carried out by virtual quark-antiquark pairs, and color charge anti-screening, carried out by virtual gluons. It is possible to demonstrate that the main contribution among these two depends on the number of different quark flavors N_f and on the number of different colors N_c accounted for in the theory. For QCD, the prevalence of anti-screening effect is established as long as $11\,N_c > 2\,N_f$ [9]; according to present knowledge there exist three colors and six quark flavors, providing a justification for the asymptotic freedom. The strength of the color force at low energy leads to the confinement of quarks and gluons, the phenomenon due to which color-charged particles cannot be isolated and directly observed. Thanks to this property, as two color charges are pulled apart, at some point it becomes energetically favorable for a new quark–antiquark pair to appear, rather than producing an isolated color charge. This is profoundly different to what happens in QED, where the electric field between electrically charged particles decreases rapidly as those particles are separated. In contrast to asymptotic freedom, that can be demonstrated exactly, because of the strongly non-linear nature of the color field, quark confinement is difficult to prove mathematically.

2.2.2 Non-perturbative QCD approaches at a glance

The dependence of $\alpha_s(\mathcal{Q}^2)$ — defined in Eq. (2.8) — on the momentum transfer $\mathcal{Q}$ encodes the underlying dynamics of hadron physics, from color confinement to asymptotic freedom. QCD does not provide a single approximation method which is applicable to all length scales. Instead, the most suitable theoretical frameworks for QCD predictions depend on the energy scale of the phenomenon that one wants to study. For hard processes, with a large momentum transfer, the coupling α_s is small and they can be successfully described using perturbation theories; for soft processes, with a small momentum transfer, this is no

longer true, and different solutions need to be employed in this so-called non-perturbative regime. Probing the internal structure of hadrons falls into this latter category. Among the different methods to address such processes, it is common to find phenomenological approaches, Effective Field Theories (EFTs), and Lattice Quantum ChromoDynamics (LQCD).

Phenomenological approaches: one viable option is to assume a function describing the potential based on phenomenological arguments such as available data or lattice computations. Since they rely on an assumed potential, phenomenological models are not a systematic approach. Nevertheless, they can be useful especially in particular regimes. One example where potential models are widely used is the computation of the mass of quarkonium states, namely flavorless mesons composed of a heavy quark and its own antiquark. More precisely, the word *quarkonium* refers to charmonium ($c\bar{c}$ states) and bottomonium ($b\bar{b}$ states) [2], leaving out from the definition lighter quark–antiquark states. The assumption in this case is that, because of their heavy masses, the motion of the quarks that comprise the quarkonium state is non-relativistic, making possible a description in terms of a static potential.

Effective Field Theories: EFTs are approximations relying on the idea of separate physics at different scales. The philosophy and basic principles of this approach are very generic, and EFTs represent a widely used method in many different areas of physics [13,14]. In a certain approximation, physics at scales much different from the one of interest becomes irrelevant and can be neglected; EFTs can be built by leveraging hierarchies between these quantities. An EFT includes the appropriate degrees of freedom to describe physical phenomena occurring at a chosen length scale, while ignoring substructure and degrees of freedom at shorter distances. Short-distance quantum fluctuations associated with much smaller length scales are absorbed into the coefficients of the various operators in the EFT. From this point of view, it is perceivable that EFTs work best when the separation between the length scale of interest and the length scale of the underlying dynamics is large. In general, EFTs are a good description of some regimes of interest in QCD, but they cannot describe or make predictions beyond those specific regimes.

Lattice QCD: LQCD is a systematically-improvable non-perturbative formulation of QCD [11, 15]. It considers spacetime as a finite, discretized, Euclidean

[2] The mass of the top quark t is too high to allow the formation of a $t\bar{t}$ bound state.

grid, called indeed *lattice*. In this formulation, fields representing quarks are defined at lattice sites, while the gluon fields are defined on the links connecting neighboring sites. When taking the lattice space infinitely large and reducing the spacing between its sites to zero, continuum QCD is recovered. LQCD is based on complex numerical algorithms derived from a mathematical analogy between Feynman paths in Quantum Mechanics (QM) and *steps* in the Markov Chain Monte Carlo algorithm [16]. Although in principle it provides a way to solve the theory to the desire precision without any assumption, as the lattice spacing decreases the required computational cost increases dramatically. The typical outcomes of LQCD computations are predictions about properties of composite particles (such as their masses and lifetimes). These properties, when computed for experimentally well-known states, have to match data in order to support further predictions.

2.2.3 Hadron classification

In particle physics, the term *hadron* refers to all composite subatomic particles that experience the strong interaction. Hadrons are bound states of quark and gluon fields. Since gluons carry color charge as their only quantum number, the total quantum numbers of strongly interacting particles result exclusively from those of their constituent quarks (also known as valence quarks). The classification scheme for hadrons in terms of their quantum numbers is based on the quark model [17, 18].

As already mentioned in Section 2.1, quarks and their antiparticles are fermions with spin-$\frac{1}{2}$. By convention, quarks are assigned positive parity $P = +1$ and additive baryon number $\mathcal{B} = +\frac{1}{3}$, while antiquarks are assigned negative parity P = -1 and baryon number $\mathcal{B}$ = -$\frac{1}{3}$. All the additive quark quantum numbers are reported in Table 2.1. By convention, the quark flavor (I_z, S, C, B, or T) has the same sign as its charge Q; in this way antiquarks have opposite flavor sign with respect to quarks. The quark's additive quantum numbers are related to its charge via the generalized Gell-Mann-Nishijima formula [11]:

$$Q = I_z + \frac{\mathcal{B} + S + C + B + T}{2}. \tag{2.10}$$

Although quarks carry color charge, as a consequence of color confinement (see Section 2.1) the only states that occur macroscopically — hadrons — are the singlets of $SU(3)_c$; in other words all hadrons are color neutral states, thus have zero total color charge. One natural classification for hadrons is to divide

Table 2.1: Additive quantum numbers for the three generations of quarks.

		d	u	s	c	b	t
Q	electric charge	-1/3	+2/3	-1/3	+2/3	-1/3	+2/3
$\mathcal{B}$	baryon number	+1/3	+1/3	+1/3	+1/3	+1/3	+1/3
I	isospin	1/2	1/2	0	0	0	0
I_z	isospin (z-component)	+1/2	-1/2	0	0	0	0
S	strangeness	0	0	-1	0	0	0
C	charm	0	0	0	+1	0	0
B	bottomness	0	0	0	0	-1	0
T	topness	0	0	0	0	0	+1

them into integer and half-integer spin particles. *Mesons*, hadrons composed of $q\bar{q}$ pairs, represent the first group; *baryons*, hadrons made of an odd number of quarks, with a minimum of three, represent the latter.

2.2.3.1 Ordinary hadrons

When the quark model was first postulated in the 1960s, it was meant to be a way to organize the known states in a meaningful way. It was originally built on the assumption of three quark flavors. In this scenario, quarks lie in the fundamental representation ($\mathbf{3}$) of flavor $\mathrm{SU}(3)_f$, and antiquarks lie in the complex conjugate representation ($\overline{\mathbf{3}}$). The scheme obtained with this representation was sufficient to fit all composite bosons and fermions known back then. Furthermore, the discovery of new states predicted by such a model contributed to its success. Despite the introduction of more quark flavors, from three to six, the model did not lose its validity, and still today it is widely used to describe ordinary mesons and baryons.

Mesons: In the simplest possible configuration, mesons are bound states of a quark and an antiquark ($q\bar{q}$); they are bosons with baryon number $\mathcal{B} = 0$. Figure 2.3 shows the meson nonets obtained when considering three flavors (u, d, s), for the two spin configurations $J = 0$ and $J = 1$. Mesons are classified in J^P (or[3] J^{PC}) multiplets. In this notation, P represents the meson parity and C its charge conjugation. The meson spin is given by the relation $|l - s| \leq J \leq |l + s|$, with l being the orbital angular momentum of the $q\bar{q}$ state and s being equal either

[3] C is defined only for mesons made of a quark and its own antiquark.

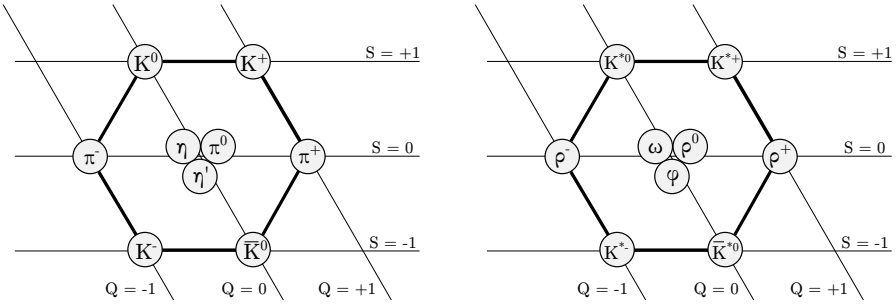

Figure 2.3: Meson nonets for J = 0 (on the left) and J = 1 (on the right) in the case of three quark flavors (*u, d, s*). In these schemes, mesons are arranged according to their charge Q and strangeness S.

to 0 (antiparallel quark spins) or 1 (parallel quark spins). The meson parity is given by the relation $P = (\text{-}1)^{l+1}$; its charge conjugation, when defined, is given by $C = (\text{-}1)^{l+s}$. In the quark model, some J^{PC} configurations are forbidden for mesons. As an example, states with parity $P = (\text{-}1)^J$ (also referred as *natural spin parity*), according to the previous rules must have $s = 1$, and hence, CP must be equal to $+1$. Thus, mesons with natural spin parity and $CP = -1$ are forbidden in such model. They may still exist, but will not find a collocation in the model itself and therefore fall into the category of exotic states. Some examples of such configuration are: 0^{+-}, 1^{-+}, 2^{+-}, 3^{-+}.

Baryons: Baryons are fermions with baryon number $\mathcal{B} = \pm 1$, composed of three quarks (qqq) or three antiquarks ($\bar{q}\bar{q}\bar{q}$). Figure 2.4 shows the baryon octet, arranging spin-$\frac{1}{2}$ baryons, and decuplet, arranging spin-$\frac{3}{2}$ baryons, in the three quark flavors (*u, d, s*) scenario $\text{SU}(3)_f$. Baryons, as well as mesons, can be classified in J^P multiplets. Consisting of three quarks, baryons spin vectors can add to a vector of length $s = 1/2$ (with two relative projections: $s_z = +\frac{1}{2}$, $\text{-}\frac{1}{2}$) or $s = \frac{3}{2}$ (with four relative projections: $s_z = +\frac{3}{2}$, $+\frac{1}{2}$, $\text{-}\frac{1}{2}$, $\text{-}\frac{3}{2}$). As in the case of mesons, the total angular momentum J is given by the combination of the spin s and the orbital angular momentum l by the relation $|l - s| \leq J \leq |l + s|$, and the parity P is given by $P = (-1)^{l+1}$. Baryons obey the Pauli exclusion principle. Since the color-related part of the baryon wave function must be a $\text{SU}(3)_c$ singlet, the remaining parts have to be completely symmetric:

$$|\, qqq \,\rangle_A = |\, \text{color} \,\rangle_A \, |\, \text{space, spin, flavor} \,\rangle_S. \tag{2.11}$$

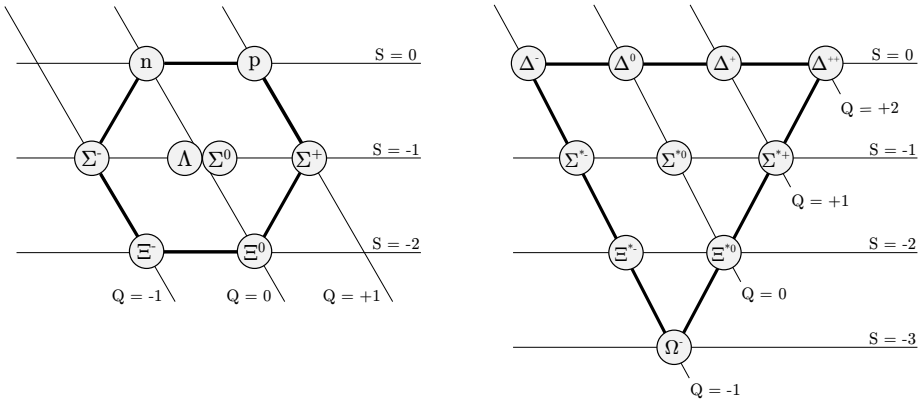

Figure 2.4: Baryon octet (on the left) and decuplet (on the right) in the case of three quark flavors (*u, d, s*). In the octet spin-$\frac{1}{2}$ baryons find their collocation, while in the decuplet spin-$\frac{3}{2}$ baryons. In these schemes, baryons are arranged according to their charge Q and strangeness S.

2.2.3.2 Exotic hadrons

As QCD developed, and essentially absorbed the quark model, it became apparent that there was no obvious reason to have only quark-antiquark and three-quark combinations: as long as the final configuration is color-neutral, there is no additional QCD-driven limit to the number of quarks constituting one hadron [4]. The adjective *exotic* is nowadays used when referring to hadrons consisting of more than three valence quarks, or with explicit valence gluon content. Analogous to ordinary hadrons, exotic hadrons are classified as being either bosons, like ordinary mesons, or fermions, like ordinary baryons; thus it is possible in literature to come across the more specific terms exotic mesons and exotic baryons.

In the absence of a rigorous analytical method for making first-principle calculations of the spectrum of non-standard hadrons, simplified models — motivated by the color structure and other general features of QCD — have been developed and are commonly used to explore the exotic sector. In this section some of these phenomenological approaches are introduced. The color structure of QCD suggests the existence of different categories of non-standard hadronic particles, that can be grouped in two main classes: multiquark states and structures with valence gluons. Figure 2.5 shows a graphical representation of the most common scenarios for exotics. Each of these scenarios would deserve a chapter by itself, but it would go far beyond the scope of this dissertation. In the follow-

[4] It is actually fair to note that Gell-Mann proposed the existence of multiquark states already in 1964, when introducing for the first time his classification model for mesons and baryons [17].

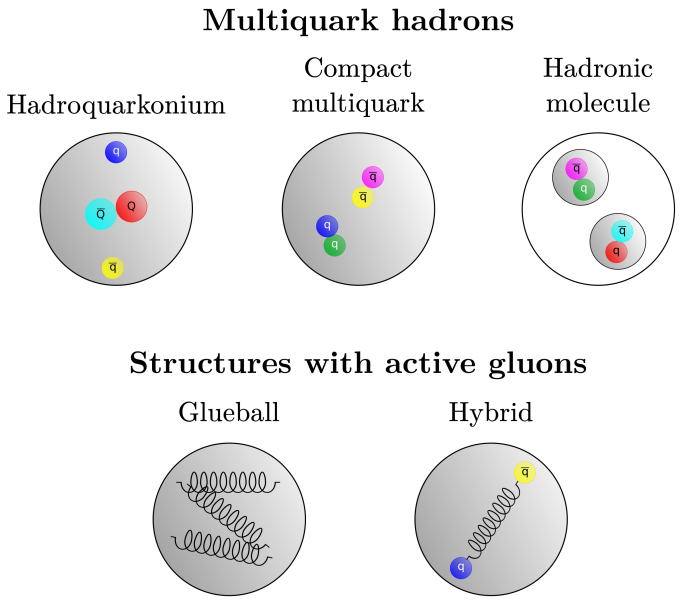

Figure 2.5: Graphical representation of common exotic hadrons. Upper case $Q\bar{Q}$ inside the Hadroquarkonium (top left sketch) represents its quarkonium core composed of heavy quarks ($c\bar{c}$ or $b\bar{b}$ quarks).

ing paragraphs a small introduction is given, together with specific references for each topic. Comprehensive reviews of exotic states in general can be found in Refs. [19–21].

Multiquark hadrons: Hadrons made of more than three valence quarks belong to the exotic family. According to the actual number of constituent quarks it is possible to distinguish several multiquark groups; the most common among them are *tetraquarks* (from Greek *tetra-*, *four*) composed of four quarks, *pentaquarks* (from Greek *penta-*, *five*) made from five quarks and *hexaquark* (from Greek *hexa-*, *six*) composed of six quarks. A priori, a system consisting of more than three valence quarks is a complicated object, and it is unclear whether or not any kind of clustering occurs in it. One way to approach this problem is to focus on possible substructures and investigate their implications. In this perspective, existing multiquarks models include *hadroquarkonia* [22, 23], *compact multiquarks* [24, 25] and *hadronic molecules* [26].

Hadroquarkonium consists of a compact quarkonium core surrounded by an excited light-quark cloud. The model was triggered by experimental observations: many heavy exotic candidates (such as $\psi(4360)$, $\psi(4660)$, or $Z_c(4430)$ [27–29]) contain in the final state a quarkonium and light quarks. In such a hadroquarkonium scenario, a force analogous to the Van der Waals force could be responsible

for the binding of the core with the cloud.

Compact multiquarks refer to multiquark states that contain as building blocks diquarks and/or antidiquarks. Diquarks [30] are quark-quark pairs qq clustering together and forming colored-states [5]. Two or more of these states can then combine to form color-neutral hadrons, with more than three valence quarks and thus exotics [31].

Hadronic molecules are aggregate states of two hadrons. The basic idea behind this description is a generalization of nuclei with the replacement of nucleons with mesons and baryons. Exploiting the similarities with light nuclei it is possible to derive some properties of such states.

Structures with active gluons: Because of its non-abelian structure, and the peculiarity of gluons to couple among themselves, QCD predicts the existence of isoscalar mesons which contain only gluons, the glueballs [32].

When allowing constituent gluons — together with constituent quarks and antiquarks — the quark model can be extended with the introduction of hybrids. The term *hybrid* conventionally refers to quark-antiquark mesons with excited gluonic degrees of freedom. In this framework, different theories have been proposed, with substantial differences among them. Two examples of models involving hybrids are the flux tube model [33] and the constituent gluon model [34].

[5] In $SU(3)_c$ qq states can be either in the $\bar{\mathbf{3}}$ or in the $\mathbf{6}$ representation.

3

uuddss hexaquark

Among the plethora of exotic states that have been predicted exploiting the properties of the quark model, one of the most advertised cases refers to the six-quark state *uuddss*. Its very long history dates back to 1977, when R. L. Jaffe first predicted the existence of an object with the quark content of two Λ baryons and called it *H dibaryon* [35]. Despite the absence of any experimental evidence so far, the H dibaryon is still today an appealing topic, mainly thanks to a renewed theoretical effort [36,37] and recent LQCD results [38–40]. From the experimental point of view there are still open possibilities to be explored, together with the opportunity to improve the current upper limits on its existence. Apart from its historical importance, being one of the first six-quark states suggested and so far not yet discovered or ruled out, the H dibaryon could represent an excellent Dark Matter (DM) candidate [37]. The central part of this dissertation will focus on a search for this double strange particle to be performed at the Belle II experiment, and on the expected sensitivity that could be reached with the future data sample to be collected at the $b\bar{b}$ resonances below the $B\bar{B}$ threshold ($\Upsilon(nS)$ with n = 1, 2, 3). These narrow $b\bar{b}$ resonances decay primarily via three gluons [11], in which $s\bar{s}$ quark pairs are produced with roughly the same probability as $u\bar{u}$ and $d\bar{d}$ pairs. This characteristic makes such states particularly well suited for searches for multiquark states with nonzero strangeness.

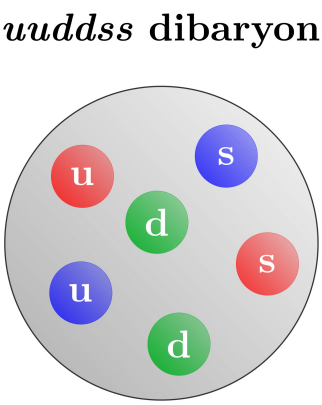

Figure 3.1: Graphical representation of the *uuddss* dibaryon.

Technically speaking, the term *dibaryon* denotes any object with baryon number $\mathcal{B} = 2$. From a constituent point of view, the requirement is that the difference between the number of valence quarks and antiquarks must be equal to six. In principle, as discussed in Section 2.2.3.2, the structure of a multiquark state may have different configurations: a dibaryon may be of molecular type or being a spatially compact object. The models that will be considered and expanded on in this chapter describe the *uuddss* dibaryon as a spatially compact object. Along the lines of Fig. 2.5, Fig. 3.1 shows a pictorial representation of such a multiquark structure.

In this chapter, a review of the *uuddss* hexaquark — both from a theoretical and an experimental point of view — will be given. The theoretical part (Section 3.1) will focus specifically on three substantially different models and their implications (Sections 3.1.1 to 3.1.3); for each of them, references to related theories will be provided as well. To conclude the first half of the chapter, an entire subsection will then be devoted to LQCD results (Section 3.1.4). In the experimental part (Section 3.2) a summary on searches and their results will be given.

3.1 Theoretical review

3.1.1 Jaffe's dibaryon

In 1977 R. L. Jaffe, making use of the quark bag model [41] (today often referred as MIT bag model), predicted the existence of a stable, spin and isospin singlet $I\,(J^P) = 0\,(0^+)$, double strange S $= -2$ six-quark state with quark content

uuddss, and named it H [35]. According to Jaffe's calculations, the hyperfine interaction of such a state should be larger than the same quantity for two separated baryons, and for this reason it should exist. The model predicted the mass of the H dibaryon, M_H, to be in the range $M_H \in [2055, 2230]$ MeV/c^2. The lower limit $M_{H,min}$ can be written as the sum of a proton (m_p), an electron (m_e), and a Λ baryon (m_Λ) mass ($M_{H,min} = m_p + m_e + m_\Lambda = 2055$ MeV/c^2), thus making the H dibaryon a non-stable object. Moreover, the upper limit $M_{H,max}$ can be written as twice the mass of a Λ baryon ($M_{H,max} = 2m_\Lambda = 2230$ MeV/c^2), forbidding the H dibaryon to decay strongly into two Λ baryons. As a result, the H dibaryon predicted by Jaffe would decay predominantly by non-leptonic weak decay. Jaffe's work initiated an era of many theoretical predictions involving the existence of dibaryons, not solely limited to double strangeness content [42–55]. Two interesting reviews about the history of search for dibaryons can be found in Refs. [56, 57].

Jaffe's prediction was based on simplified symmetry considerations, with the assumption of a color-magnetic interaction V_{c-m} between quarks generating a hyperfine-splitting [35]:

$$V_{c-m} = -\sum_{i>j} (\lambda_i \cdot \lambda_j)\,(\sigma_i \cdot \sigma_j)\,M(m_i R,\, m_j R), \tag{3.1}$$

where $\lambda_{i(j)}$ and $\sigma_{i(j)}$ represent the color and the spin operator of the $i(j)$-th quark, respectively, and $M(m_i R,\, m_j R)$ denotes a short range spatial interaction between quarks i and j, that conserves the flavor.

The main limitation of models based on Eq. (3.1) is the assumption of unbroken SU(3)$_f$ symmetry. After Jaffe's work, other theorists provided different calculations based on various models, often including more realistic considerations. In particular, accounting for SU(3)$_f$ symmetry breaking introduces a severe reduction of the resulting binding energy [58–60]. More generally, the development of different models led to very different predictions about the H dibaryon mass, extending from deeply bound states (below Jaffe's original lower limit) to unbound states, in some cases refuting the possible existence of such a stable state [49, 61–64].

It is worth noting that Jaffe returned several times to the H dibaryon subject in his work after the very famous first manuscript from 1977. In 1995, together with G. Baym *et al.* [65], he suggested a metastable H dibaryon (with $M_H < m_p + m_\Lambda$) as possible *cygnet*, a neutral particle originating from the condensed star in Cygnus X-3 and responsible for initiating high energy muon showers [66].

In 1997, together with S. V. Bashinsky [67], he considered an unbound six-quark H dibaryon (with $M_H > 2m_\Lambda$), trying to link its possible manifestation with a description to the interplay between quark states and hadronic thresholds, and elaborating about promising reactions to be studied for a search in such a scenario. Making use of the P-matrix formalism [68], the conclusion they drew was to rely on quasi-elastic secondary scattering [1] as most promising reactions in the search for such a state, in the case of M_H situated very close to one two-baryon threshold (like, for example, $\Lambda\Lambda$, $\Xi^- p$, $\Xi^0 n$, $\Sigma^0\Sigma^0$, or $\Sigma^+\Sigma^-$).

3.1.2 Kochelev's stable dibaryon

In 1999 N. I. Kochelev revived and elaborated on the idea of a stable H dibaryon [69]. In such a work it is argued that, in the context of the H dibaryon mass calculation, it is crucial to take into account the instanton interaction between quarks [70]. Despite few authors before him accounted for such effects [61, 71], his argument is that in these cases the mass of the H dibaryon was overestimated. Considering the instanton-induced interaction in the simple quark constituent model, any hadron mass m_h can be written as [69]:

$$m_h = N_U U + N_S S + \Delta m_{inst}. \tag{3.2}$$

In Eq. (3.2), $N_{U(S)}$ and $U(S)$ represent the number of light (strange) quarks and their constituent masses, respectively, and Δm_{inst} the contribution to the hadron mass induced by instanton interactions. As can be deduced from Eq. (3.2), a strong interaction with vacuum (and so a large attraction between quarks) could lead to a large reduction of the hadron mass. In the case of the H dibaryon, taking advantage of its wave function dissociation [71] and of a previous study on baryons mass splitting induced by instantons [72], Kochelov determined the instanton contribution to the H dibaryon mass to be:

$$\Delta m_{H,inst} = -1048 \text{ MeV/c}^2, \tag{3.3}$$

leading to a H dibaryon mass value of:

$$M_H = 1718 \text{ MeV/c}^2. \tag{3.4}$$

The so-obtained mass M_H is smaller than the sum of two nucleon masses ($2m_N = 1876$ MeV/c^2), thus making the H dibaryon an absolutely stable particle. Accord-

[1] For example, producing a NΞ pair and then observing it scattering into two Λ.

ing to the author, the existence of such a stable H dibaryon could have crucial consequences in cosmology, providing an explanation for ultra-high energy cosmic ray events [73] observed above the GZK cut-off [73, 74]. Admitting the existence of some sort of ultra-high energy cosmic H dibaryons source, their interaction with nuclei in the Earth's atmosphere, and their subsequent photodisintegration into two Λ baryons, would be a natural explanation of the anomalous events observed above the GZK cut-off.

3.1.3 Farrar's dibaryon

Along the lines of a deeply bound hexaquark, G. R. Farrar — for the first time in 2003 and a few years later in a more mature paper — noted that an absolute stable H dibaryon is a potentially optimal DM candidate [36, 75]. The disagreement with Kochelov's interpretation of a deeply bound H as possible messenger particle accounting for ultra-high energy cosmic rays is unmistakable [75]. Instead, the idea suggested in the manuscripts is that a possible DM candidate may be provided by QCD itself (therefore not requiring physics beyond the SM), in the form of a stable *uuddss* six-quark state. Such a state was renamed S by the author [2], standing for Sexaquark, Singlet, Scalar, Strong, and Stable [36]. Assuming a scenario with DM composed of approximately equal numbers of u, d, and s quarks, the measured ratio of dark matter to ordinary matter could be explained with the Boltzmann distribution in the quark gluon plasma with a few other assumptions. These considerations, applied to a stable and compact H dibaryon with mass $M_H \in [1860, 1880]$ MeV/c^2, lead to an agreement between prediction and measurement within its 15% uncertainty [76]. In this scenario, the $SU(3)_f$ singlet H dibaryon size is much smaller with respect to octet baryons ($r_H \approx 0.15-0.4$ fm compared to $r_N = 0.9$ fm), and consequently does not bind to nuclei. Depending on its mass M_H, a deeply bound H would be absolutely stable if $M_H < 2(m_e + m_p) \simeq 1878$ MeV/c^2 (as a consequence of baryon number conservation), or metastable if $M_H < (m_e + m_p + m_\Lambda) \simeq 2055$ MeV/c^2, with its lifetime being longer than the age of the universe [77]. As observed by the author, the case of a very light H dibaryon, light enough to be produced with a pion, seems to be ruled out: rare occurrences of pion production from nucleon fusion processes like [3] $\{n\,n\} \to H\,\pi^0$ or $\{p\,n\} \to H\,\pi^+$ should have been already observed by the Super-Kamiokande experiment [78]. This last consideration suggests a possible lower limit on the H mass $M_H \gtrsim 2m_N - m_\pi \simeq 1.7$ GeV/c^2 [36]. As a matter of

[2] For consistency, in the rest of the chapter it will also be referred as H dibaryon.
[3] Curly brackets denote that protons p and neutrons n are inside a nucleus.

fact, such a stable state would have eluded detection in the various experiments carried out in the years prior to Farrar's publication [36]. Before that, no experiment specifically searched for a stable and compact H, mostly assuming the H to be a loosely bound state, while experiments directly searching for long-lived neutral states explicitly excluded the region below 2 GeV/c^2 because of neutron-induced background [79] (for an exhaustive review of the experiments searching for H dibaryon please refer to Section 3.2). In Farrar's work [36], two strategies are suggested for the possible discovery of a stable H dibaryon, targeting different existing experiments:

- the study of the exclusive Υ decay reactions:
  $\Upsilon\ [\rightarrow gluons] \rightarrow H\,\bar{\Lambda}\,\bar{\Lambda}$ or $\bar{H}\,\Lambda\,\Lambda\ (+\,\pi_s$ and/or $\gamma_s)$;

- the search for characteristic decay chains after H annihilation on beam pipe or detector material:
  $\bar{H} + N \rightarrow \bar{\Xi}^{0\,(+)} + X$, $\bar{H} + N \rightarrow \bar{\Lambda} + K^{0\,(+)} + X$.

The common approach is to search for final states with apparent baryon number and strangeness violation ($\Delta\mathcal{B} \neq 0$ and $\Delta\mathrm{S} \neq 0$). In both cases, there is no direct observation of the H (or $\bar{H}$), but the mass M_H should possibly be measurable via missing mass in the former case, and via energy-momentum conservation in the latter.

The cosmological implications of a possible stable six-quark state are not universally accepted. C. Gross *et al.* argue that, for the model to reproduce the cosmological DM abundance, the H mass should be equal to 1.2 GeV/c^2; as already noted, though, the nuclear stability forbids dibaryon mass values $M_H \lesssim$ 1.7 GeV/c^2 [80]. According to E. W. Kolb and M. S. Turner, a possible stable H dibaryon in the mass range $M_H \in [1860, 1890]$ MeV/c^2, where nuclear stability is ensured, could explain only a fraction of DM, since its abundance would not be enough [81]. Finally, S. D. McDermott, S. Reddy, and S. Sen., studying a possible stable H dibaryon in the context of proto-neutron stars, concluded that such a state is incompatible with the stability of neutron stars and with the observed supernova explosions [82].

3.1.4 *uuddss* dibaryon in LQCD

Trying to establish whether the existence of the H dibaryon is a prediction of QCD has always been a fertile ground for LQCD. Early lattice studies — that compared to the more recent times suffered from finite-size effects, relatively large

values of unphysical quark masses, and low statistics — produced inconclusive and contradicting results on this topic: while some claimed the existence of a bound state [83–85], others ruled out this possibility providing evidence for an unbound H dibaryon state [86–89].

In more recent times, LQCD calculations with regard to the H dibaryon made use of two different formalisms, both common in LQCD when it comes to studying two-baryon systems: the Luscher's method [90, 91] and the HAL QCD method [92–94]. Results on the H dibaryon based on the first approach were obtained by the NPLQCD collaboration [40, 95–97], and by the Mainz group [38, 98]. The alternative approach has been employed by the HAL QCD collaboration [39, 99–101]. Depending on the methodology and/or the value of the pion mass employed in the calculations, the results for the binding energy B_H vary considerably, with estimates ranging from a few MeV up to 75 MeV. Among the most recent results, in 2020 the HAL QCD collaboration studied the $\Lambda\Lambda$ interaction close to the physical point ($m_\pi = 146$ MeV/c^2 and $m_K = 525$ MeV/c^2), using $N_f = 2{+}1$ flavors [39]. Such a system, according to their result, is only weakly attractive and does not sustain a bound or resonant dihyperon. In 2021 the Mainz group, using the Luscher's method, suggested the existence of a weakly bound H dibaryon, with binding energy $B_H = 3.97 \pm 1.16_{stat} \pm 0.86_{syst}$ MeV [38]. Such a value of binding energy is substantially lower with respect to previous lattice calculations [40, 95–101]. One common limit of both results is that the lattice simulation was not performed exactly at the physical point. For this and other reasons both these calculations are not yet conclusive, and some omitted effects still remain to be addressed in the future.

3.2 Experimental review

As it is often the case in physics, interest in the possible existence of the H dibaryon did not only excite the theoretical community, but almost immediately after its original formulation, it expanded into the experimental field. Since then numerous experiments have been carried out hunting for such a state.

When searching for an hypothetical particle, one needs to consider the possible decay channels of such an object. In case of the H dibaryon, its binding energy — and thus its mass with respect to the $\Lambda\Lambda$ threshold — plays a fundamental role. A bound H dibaryon, with $M_H < 2m_\Lambda$, could only decay via weak interaction; the dominant decay channel would then be $H \to \Lambda N\pi$, with a narrow resonance structure. An H dibaryon above the $\Lambda\Lambda$ threshold would

decay strongly, predominantly via $H \to \Lambda\Lambda$, and the width of such a candidate is expected to be broad. In general, the broader a resonance is, the harder it is to uniquely identify it in experiments, being more difficult to distinguish the resonance from non-resonant background processes. Finally, a stable H dibaryon — being neutral and indeed stable — would escape any detection, and in such a case its existence could manifest itself as a peak around its mass in the missing mass spectrum of a fully exclusive measurement.

Especially in the early stage of the experimental hunt for the H dibaryon, many of the searches have been performed in nuclear reactions in which the H is expected to be produced in nuclei. After an early period of controversial claims about its existence [4] — none of which withstood critical examinations — the first important experimental result on the H dibaryon arose from the observation of the so-called "NAGARA" event [103, 104], which exhibits the unambiguous signature of the double-Λ hypernucleus ${}^{6}_{\Lambda\Lambda}$He produced via Ξ^- capture in emulsion. The existence of double-Λ hypernuclei is intimately related to the existence of the H dibaryon, and in particular with the upper limit of its mass. In fact, a possible H dibaryon with a mass M_H less than twice the Λ hyperon mass in a nucleus is expected to be formed from two Λ hyperons in the nucleus. As a consequence, the existence of a double-Λ hypernucleus with binding energy in the nucleus $B_{\Lambda\Lambda}$ can be interpreted as a lower limit for the mass of the H dibaryon, according to [103]:

$$M_H > 2m_\Lambda - B_{\Lambda\Lambda}. \tag{3.5}$$

From the analysis of the NAGARA event, $B_{\Lambda\Lambda}$ was found to be $B_{\Lambda\Lambda} = 6.93 \pm 0.16$ MeV, leading to a lower limit for the mass of the H dibaryon, in the bound scenario, of $M_H > 2224$ MeV/c^2 at a 90% Confidence Level (CL).

In 1998, the KEK-PS E224 collaboration searched for a possible H dibaryon in the (K^-,K^+) reaction with a nuclear target [105]. Studying the reaction ^{12}C $(K^-, K^+)\Lambda\Lambda X$, they reported an enhancement in the $\Lambda\Lambda$ invariant mass spectrum at the $\Lambda\Lambda$ threshold. The same result was confirmed a few years later with a follow-up experiment — with improved statistics — by the KEK-PS E522 collaboration [106]. Nonetheless, it was not possible for them to determine with certainty if such a threshold enhancement was a signal of the existence of the H dibaryon or if it could simply be explained by the $\Lambda\Lambda$ final state interaction. The BNL E836 collaboration performed a search for H dibaryon on a different target (a liquid helium target), using the reaction ^{3}He $(K^-, K^+)Hn$ [107]. No evidence for H production was found and cross section limits were established in binding

[4] For a complete review of early experiments see Ref. [102].

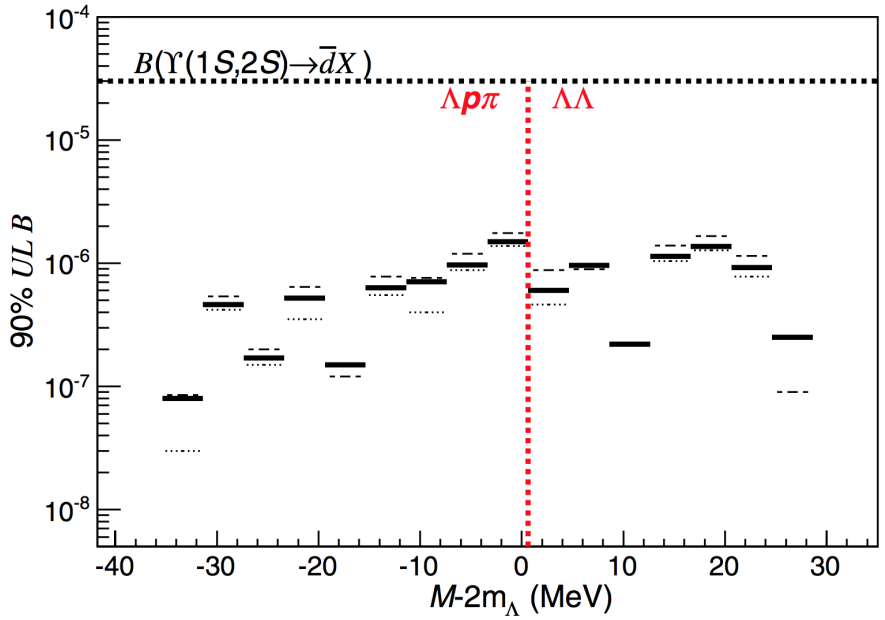

Figure 3.2: Branching-fraction upper limits (UL B) at 90% CL for $B(\Upsilon(1S,2S) \to HX)$ for a narrow H dibaryon as a function of $M_H - 2m_\Lambda$, obtained by the Belle collaboration [109]. The vertical dotted red line indicates the $M_H = 2m_\Lambda$ threshold. The limits below this threshold are for the decay channel $H \to \Lambda p\pi$, those above are for $H \to \Lambda\Lambda$. For each mass bin, the upper limit is shown as solid horizontal bars, while the $+1\sigma$ ($+2\sigma$) value from the fitted signal yield is shown as dotted (dashed) bar. For some bins these assume negative values and are not shown in the plot. The horizontal dotted black line indicates the average PDG value for $B(\Upsilon(1S,2S) \to \bar{d}X)$.

energy range $B_H \in [50, 380]$ MeV.

Apart from nuclear reactions, other interesting possibilities for H dibaryon searches are available at B-Factories [108] running at narrow Υ resonances. As briefly mentioned in this chapter's introduction, decays of narrow $b\bar{b}$ resonances are in fact well suited for searches for multiquark states with non-zero strangeness. In 2013, the Belle collaboration performed a search for H dibaryon production in inclusive $\Upsilon(1S)$ and $\Upsilon(2S)$ decays [109]. An 80 MeV/c^2-wide region around the $2\,m_\Lambda$ threshold was scanned in two decay channels: $H \to \Lambda\, p\, \pi^-$ (below threshold) and $H \to \Lambda\Lambda$ (above threshold). No indication of a H dibaryon was found, and upper limits for the branching fraction in the order of 10^{-6} with 90% CL were set. Figure 3.2 shows the resulting 90% upper limits as function of $M_H - 2m_\Lambda$ for the decay channels $H \to \Lambda p\pi^-$ and $H \to \Lambda\Lambda$. If compared to the measured branching fractions for inclusive $\Upsilon(1S)$ and $\Upsilon(2S)$ decays to antideuterons ($\bar{d}$) [5], these H dibaryon limits are located more than an order of magnitude below them.

[5] $B(\Upsilon(1S) \to \bar{d}\,X) = (2.9 \pm 0.3) \times 10^{-5}$, $B(\Upsilon(2S) \to \bar{d}\,X) = (3.4 \pm 0.6) \times 10^{-5}$ [110, 111].

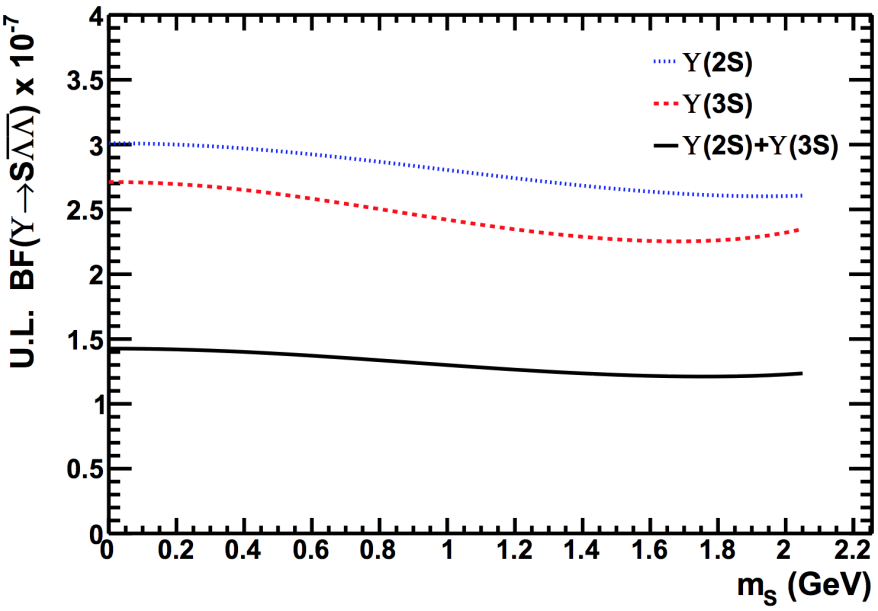

Figure 3.3: The 90% CL upper limits on the $\Upsilon(2S, 3S) \to H\bar{\Lambda}\bar{\Lambda}$ branching fraction for the $\Upsilon(2S)$ and $\Upsilon(3S)$ datasets, as well as the combined sample, obtained by the BaBar collaboration [112]. On both axis labels, S refers to the H dibaryon.

The deuteron is itself a six-quark state with rather low binging energy, and being composed of a proton and a neutron it could be seen as the H dibaryon's non-strange twin. This comparison with antideuterons suggests that, if a H dibaryon exists in such a mass range, its dynamical properties have to be very different when compared to deuterons; also, below the $\Lambda\Lambda$ threshold a possible $\Lambda p\pi^-$ decay mode of the H dibaryon is strongly suppressed.

In a recent paper, the BaBar collaboration published the result of the first search for a stable hexaquark [112], following the theoretical model from Farrar (see Section 3.1.3). Using $\Upsilon(2S)$ and $\Upsilon(3S)$ events, they probed the whole stable mass region $M_H \in [0, 2.05]$ GeV/c^2 for a possible H dibaryon produced in narrow Υ decays in combination with two Λ baryons by searching for a bump in the recoil mass squared against the $\Lambda\Lambda$ system. No evidence of such events was observed and a 90% confidence level limit on the combined $\Upsilon(2S, 3S) \to H\bar{\Lambda}\bar{\Lambda}$ branching fraction in the order of 10^{-7} was set. The results obtained by the BaBar collaboration are shown in Fig. 3.3 for the $\Upsilon(2S)$ and $\Upsilon(3S)$ datasets separately, as well as for the combined sample.

An alternative method to access hadron-hadron interactions is offered by heavy-ion collisions. Thanks to the large number of hyperons produced in such interactions — achieved by hadronization from the quark-gluon plasma — they offer the possibility to study $\Lambda\Lambda$ correlation and allow to search for the H dibaryon.

In such experiments, the stability of possible resonances (and thus the binding energy B) is expressed in terms of the sign of the scattering length a_0. A possible $\Lambda\Lambda$ bound state would exhibit a positive a_0 value ($a_0 > 0$); on the contrary, $a_0 < 0$ would imply the absence of a bound state.

The $\Lambda\Lambda$ correlation, the scattering length $a_{\Lambda\Lambda}$ and the effective range $r_{\Lambda\Lambda}$ have been studied at RHIC in Au-Au collisions at 200 GeV [113, 114]. An improved analysis [114] gave different results from those in the original paper [113], reporting a slightly attractive interaction and thus excluding the existence of a bound state in the $\Lambda\Lambda$ system. However, because of some feed-down corrections related to Σ^0 decays, these results are not sufficient to completely exclude the existence of a bound state [115]. The ALICE collaboration searched for the H dibaryon in the decay channel $H \rightarrow \Lambda p\pi^-$ in the mass region $M_H \in [2.200, 2.231]$ GeV/c^2, using central Pb-Pb collisions at $\sqrt{s_{NN}} = 2.76$ TeV [116]. In this analysis no significant signal in the invariant mass distribution has been observed and an upper limit was estimated with the assumption of a binding energy of 1 MeV.

In conclusion, despite a huge effort from the experimental community, to date no hard evidence, able to undoubtedly prove the existence of a H dibaryon, has been found. On the other hand, notwithstanding that stringent upper limits for its production in various processes exist, no experiment performed so far has been able to completely rule out the possibility of its existence.

4

The Belle II experiment

The Belle II experiment [117] represents the only next-generation B Factory in operation to date. After the huge success of the first generation B Factories — namely its predecessor Belle [118] and the BaBar experiment [119] — and their extraordinary contribution to many sectors of particle physics [108], following an initial commissioning phase the Belle II experiment has finally started to collect data on its journey towards and possibly beyond the SM frontiers. A key element in achieving these ambitious goals is to collect much higher luminosities with respect to the existing datasets. This requires upgrades to both the accelerator and the detector.

In this chapter a general overview of the SuperKEKB accelerator and of the Belle II detector with its relative subsystems will be given. Because of their relevance to the subjects covered in this dissertation, the tracking related subdetectors are described in more details. Except where explicitly stated otherwise, the information presented in this chapter is taken from Refs. [120, 121], and an in-depth description of every specific subsystem can be found there.

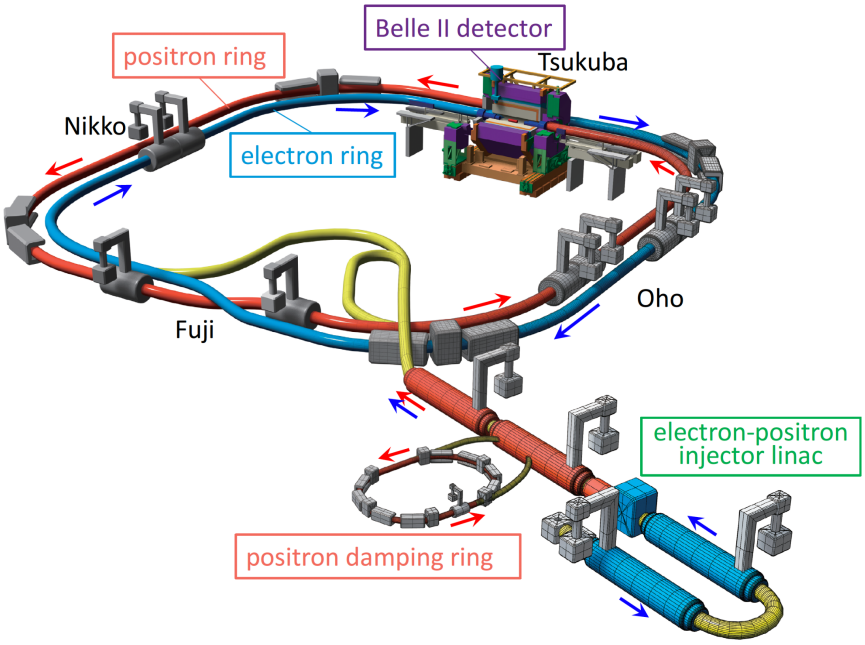

Figure 4.1: Schematic view of the SuperKEKB collider. The Belle II detector is located in the experimental cave named *Tsukuba*, around the only interaction point of the electron and positron beams. Figure taken from Ref. [122].

4.1 SuperKEKB

SuperKEKB is a double-ring asymmetric e^+e^- collider, located at the KEK (High Energy Accelerator Research Organization) laboratory [123] in Tsukuba, Japan. The accelerator is designed to collide beams of electrons and positrons at the center-of-mass energy in the region of the Υ resonances. The allowed center-of-mass energy ($\sqrt{s}$) ranges from 9.46 GeV, just below the $\Upsilon(1S)$ resonance, to 11.24 GeV, just above the $\Upsilon(6S)$ resonance. As for the previous B factories, the vast majority of the data will be collected at the $\Upsilon(4S)$ — located just above the $B\bar{B}$ threshold and thus decaying more than 90% of the time in a pair of B mesons [11]. A fraction of the data taking will be devoted, in addition, to different energies. It is foreseen to collect data at higher ($\Upsilon(5,6S)$) as well as lower energies ($\Upsilon(3S)$) [124]. In particular, the three narrow resonances $\Upsilon(nS, n \leq 3)$ represent a fertile ground for studying bottomonium transitions, physics beyond the SM, and searches for exotic states, and the central part of this dissertation falls into the latter category.

The design instantaneous luminosity of SuperKEKB is 8×10^{35} cm^2 s^{-1}, 40 times larger than the recorded peak luminosity of its predecessor KEKB [125]. This challenging goal motivated a substantial upgrade to the accelerator complex. Figure 4.1 shows a schematic view of SuperKEKB. The collider complex consists

Table 4.1: KEKB's machine parameters compared to SuperKEKB's. The listed parameters are, in order: the beam energies (E), twice the collision angle (2ϕ), the vertical beam–beam parameters ($\xi_{x,y}$), the vertical beta function (β^*_y), the beam currents (I), the beam sizes ($\sigma^*_{x,y}$), and the design instantaneous luminosity ($\mathcal{L}$). All parameters refer to the IP. Values taken from Ref. [122].

	KEKB LER (e^+) / HER (e^-)	SuperKEKB LER (e^+) / HER (e^-)
E [GeV]	3.5 / 8.0	4.0 / 7.0
2ϕ [mrad]	22	83
ξ_x	0.127 / 0.102	0.0028 / 0.0012
ξ_y	0.129 / 0.090	0.088 / 0.081
β^*_y	5.9 / 5.9	0.27 / 0.30
I [A]	1.64 / 1.19	3.60 / 2.60
σ^*_x [μm]	147 / 170	10.1 / 10.7
σ^*_y [nm]	940 / 940	48 / 62
$\mathcal{L}$ [10^{35} cm^{-2} s^{-1}]	0.211	8

of a 7 GeV High-Energy Ring (HER) for electrons, a 4 GeV Low-Energy Ring (LER) for positrons, and an injector linear accelerator (linac) with a 1.1 GeV positron Damping Ring (DR). SuperKEKB has only one Interaction Point (IP), where the two beams collide at a finite angle ϕ of ± 41.5 mrad. The method to increase the luminosity of SuperKEKB is based on a design known as *nano beam* scheme, first suggested by P. Raimondi for SuperB, a proposed high-luminosity electron-position collider near Rome (Italy) that never saw the light [126].

4.1.1 Nano beam scheme

The essential elements in the *nano beam* scheme — and thus in the SuperKEKB's luminosity increase with respect to KEKB — are a reduction in the beta function at the IP and an increase in the beam currents.

For a collider, the luminosity $\mathcal{L}$ can be written as [122]:

$$\mathcal{L} = \frac{\gamma_\pm}{2er_e}\left(1+\frac{\sigma^*_y}{\sigma^*_x}\right)\left(\frac{I_\pm \xi_{y\pm}}{\beta^*_y}\right)\left(\frac{R_\mathcal{L}}{R_{\xi_y}}\right). \tag{4.1}$$

In this equation $\gamma_\pm$ represents the Lorentz factor, e and r_e the electron charge and classical radius, respectively, and $\sigma^*_{x,y}$ the horizontal and vertical beam sizes at the IP; $I_\pm$ represents the beam current, while $\xi_{y\pm}$ and β^*_y are the vertical beam–beam

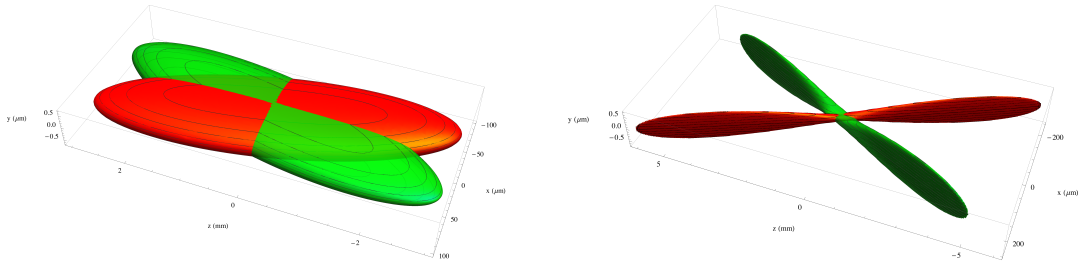

Figure 4.2: Schematic view of KEKB (left panel) and SuperKEKB collision scheme, also referred to as nano beam scheme (right panel). Note that the axes scales for the two panels are different. Figure taken from Ref. [127].

parameters and the vertical beta function at the IP, respectively. The suffix $\pm$ distinguishes the positron $(+)$ from the electron $(-)$ beam. Finally, $R_{\mathcal{L}}$ and R_{ξ_y} are a luminosity and a vertical beam-beam correction factor, respectively, that account for geometrical losses, and whose ratio can be approximately considered equal to 1. In SuperKEKB, the vertical beta function at the IP β_y^* is reduced by a factor of 20 with respect to KEKB, while the current I is increased by a factor of 2 both for the electron and the positron beam. This can be inferred from Table 4.1, where the main parameters of the two accelerator complexes are summarized. A schematic view of the old collision scheme of KEKB and the new nano beam scheme of SuperKEKB is shown in Fig. 4.2.

As an inevitable price to pay for the increase in luminosity, the background level in the Belle II detector is expected to increase as well. This motivated upgrades to the existing Belle detector, that will be introduced in the next section (Section 4.2). Because of its strong impact on track finding, the topic of beam-induced background will be further explored in the next chapter (Section 5.1.1).

4.1.2 SuperKEKB commissioning and running phases

The beam commissioning of SuperKEKB took place in three phases, *phase 1, phase 2* and *phase 3*. In phase 1, carried out in 2016, no final focusing system and no Belle II detector were installed. In this phase no beam collisions were performed. The main goals of this first period were to monitor the beam background levels in order to ensure that they were safe to install Belle II and to provide a first feedback for the optimization of the accelerator parameters. To achieve these goals the BEAST II detector system was used [128]. During phase 2, that took place in 2018, both the final focusing and the positron damping ring were in place. As for the Belle II detector, it was installed with the exception

of the vertex detectors (pixel and silicon detectors, which will be described in detail in the next section). Special detectors for background measurements were installed in their place close to the interaction region. The main goals of this phase were to measure beam background during collisions and to ensure the radiation safety of Belle II to run at higher luminosity with the final vertex detectors installed, without damaging them. Phase 3 officially started in march 2019, with the vertex detectors installed. Due to a delay in the production of the pixel detector, currently only half of its design setup is installed. The installation of the missing part is foreseen during the next long shutdown of the experiment.

The design peak luminosity of SuperKEKB (8×10^{35} cm^2 s^{-1}) is a goal to be achieved over time through the gradual increase of beam currents and the optimization of the accelerator parameters [124], and currently has not yet been reached. Later in this thesis a distinction is made between *early phase 3* and *nominal phase 3*. Early phase 3 refers to the current experiment conditions, with the pixel detector only partially installed and an instantaneous luminosity lower than the design value. Nominal phase 3 refers to future experiment conditions, with the full installation of the pixel detector and the designed value of instantaneous luminosity.

4.2 The Belle II detector

The Belle II detector is a general purpose spectrometer built around the only IP of SuperKEKB. Due to the accelerator upgrade, a major upgrade took place with the detector when compared to its predecessor Belle [129] as well. Some major components — and in particular the outermost ones — were kept from the previous experiment, with only modifications to the electronics and readout systems, while some subdetectors were newly developed. The choice of keeping the outermost components determined the space for the design of the new devices. The challenge of the detector upgrade was to maintain — and possibly improve — the good performance of the Belle detector in a new experimental environment with higher physics rate and much higher background levels.

Belle II has an approximate cylindrical symmetry around the z-axis [1], while it has a significant forward (FW) / backward (BW) asymmetry to improve the solid angle acceptance in the boost (FW) direction. In its new design, it is composed of the following subdetectors (listed from the innermost to the outermost):

[1] By convention the z-axis is set along the bisector of the angle between the direction of the electron beam and the reverse direction of the positron beam.

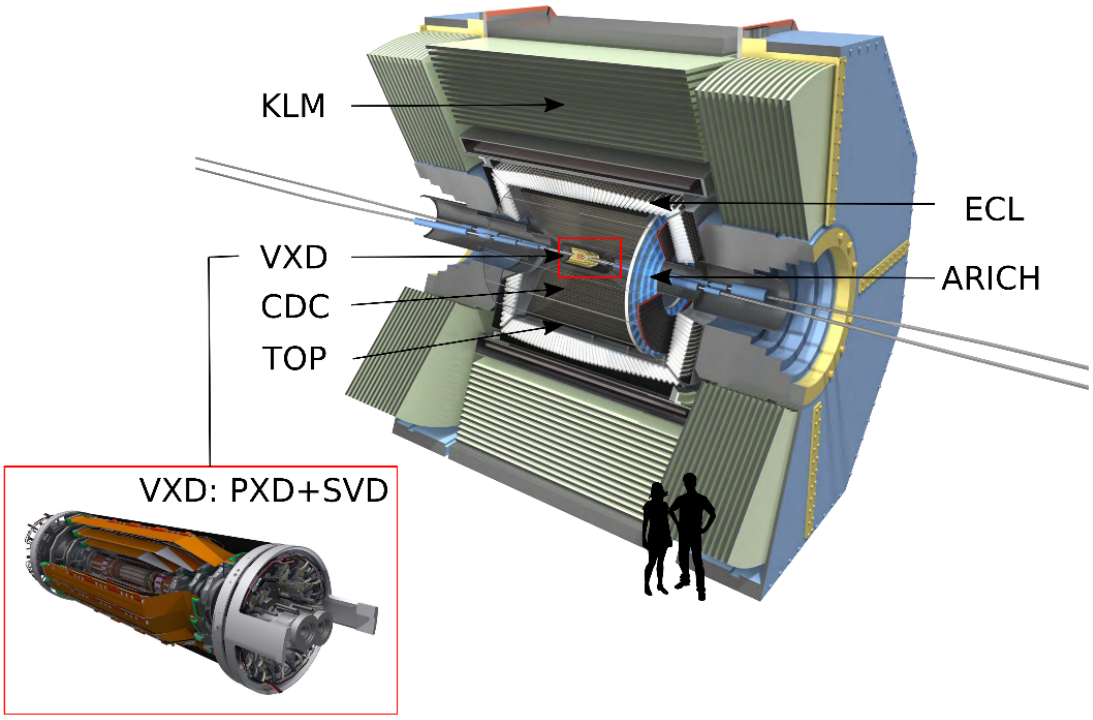

Figure 4.3: Schematic view of the Belle II detector. The red box on the bottom left is an enlargement of the central region, showing a more detailed view of the two innermost detectors, PXD and SVD, together referred to as VXD. Figure adapted from Ref. [117].

- a PiXel Detector (PXD),
- a Silicon Vertex Detector (SVD),
- a Central Drift Chamber (CDC),
- a Time Of Propagation (TOP) counter,
- an Aerogel Ring-Imaging CHerenkov (ARICH),
- an Electromagnetic CaLorimeter (ECL),
- a K_L and Muon detector (KLM).

The two innermost subsystems, PXD and SVD, together are often referred to as VerteX Detector (VXD). A schematic view of the Belle II detector is given in Fig. 4.3.

4.2.1 Tracking detectors

In Belle II, there are three dedicated subdetectors used for the reconstruction of charged tracks: PXD, SVD, and CDC. Their polar angle acceptance is $\theta \in$

$[17°, 155°]$. One of the key points of the experiment is that tracks from B meson decays need to be reconstructed with sufficient precision. In order to compensate for the smaller boost of SuperKEKB compared to KEKB ($\beta\gamma = 0.28$ instead of 0.42), the impact parameter resolution needs an improvement of a factor 2. Furthermore, the inner detector must be sufficiently radiation hard (because of the high track density of the environment) while its material budget is kept to a minimum (in order to reduce multiple scattering). Such requirements influenced the final choice of the VXD design and technology.

PXD: the PXD is a pixel detector based on the DEPleted Field Effect Transistor (DEPFET) concept [130]. Such technology allows for very thin sensors (in principle down to $\sim 50\,\mu$m [2]), with the readout electronics located outside the acceptance region, and thus not contributing to the material budget. The DEPFET sensors are organized into *ladders*, planar modules which compose the two PXD layers. In its final concept, the PXD consists of two cylindrical active detector layers, coaxial with the beam line. An overlapping in ϕ of the modules composing each layer (8 modules for the first layer, 12 for the second) ensures an overall coverage of nearly 100% within the acceptance. The inner layer (L1) is placed very close to the beam line, at a radius of 14 mm, while the second layer (L2) is at a radius of 22 mm. The size of the single pixels varies according to their position. For L1 it was chosen to be 50×55 μm^2 for the 256 pixels closest to the IP, 50×60 μm^2 for the those further out. For L2, instead, the pixels dimensions are 50×70 μm^2 and 50×85 μm^2, respectively [131]. The choice of installing two PXD layers instead of only using silicon strips was driven by the fact that the latter cannot be operated too close to the IP (~ 20 mm) because of the high occupancy — which translates to fake hits due to combinatorics. With their much finer segmentation, pixel detectors naturally have a smaller occupancy. Given a readout time of 20 μs at final luminosity, the occupancy is expected to be less than $\sim 3\%$. If this value is exceeded, PXD data has to be truncated due to data transfer limitations. Regarding the radiation hardness, the PXD modules are designed to withstand the expected 20 Mrad radiation dose during 10 years of operation of the experiment. Unfortunately, at the beginning of Belle II physics data taking (March 2019), because of technical problems in the ladder assembly, only half of the planned PXD was installed: the full L1 layer and two ladders of L2 layer. The full installation is expected to take place during the first long shut down of the experiment. A schematic view of the detector is shown in Fig. 4.4.

[2] In Belle II the thickness of the PXD active region is 75 μm.

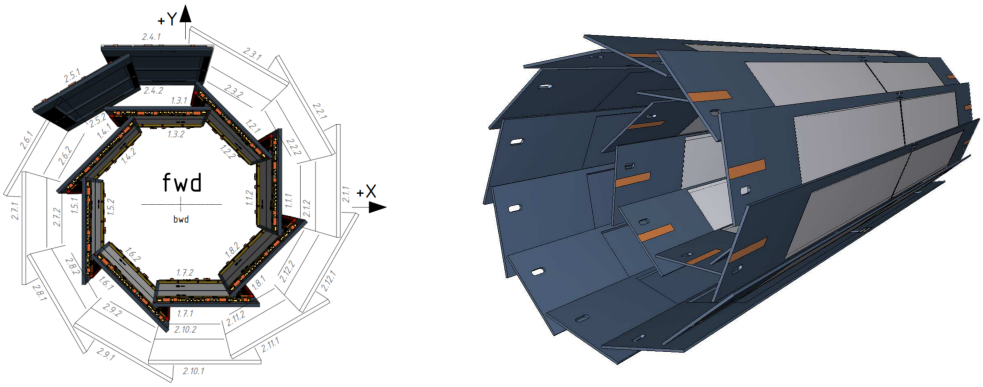

Figure 4.4: Schematic view of the PXD. In the left panel, the position of the 40 PXD modules (20 ladders) in the beam direction (xy plane) is shown. Currently only the colored modules are installed. In the right panel, a CAD rendering of the two PXD layers is shown. The light gray surfaces represent the sensitive DEPFET pixels. Figures taken from Refs. [121, 132].

Its main specifications are summarized in Table 4.2.

Table 4.2: Specifications of the Belle II PXD [133].

Layer	Radius (mm)	Ladders	Sensors	Pixels/Sensor $r\phi \times z$	Pitch $r\phi \times z$ (μm $\times\mu$m)
1	14	8	16	250 × 768	50×(55 to 60)
2	22	12	24	250 × 768	50×(70 to 85)
Sum		20	40	7 680 000	

SVD: the Belle II silicon strip detector comprises of four layers of Double-sided Silicon Strip Detectors (DSSDs), located at radii of 39 mm (L3), 80 mm (L4), 104 mm (L5), and 135 mm (L6). Each layer is made of several ladders (the exact numbers are quoted in Table 4.3). These, in turn, are composed of two (L3) to five (L6) modules. A module is the union of the silicon sensor, a hybrid circuit to host the readout chips, and a pitch adapter (which brings the signal from the sensor to the chips). Various types of sensors, characterized by different shapes and strip pitches, are employed to achieve the best performance. For the same reason, the most forward sensors of L4, L5, and L6 are slanted towards the z-axis. As in the case of the PXD, the detector design provides for a partial overlap of adjacent sensors — 8 to 10%, depending on the layer — to improve the coverage. One key feature to suppress background hits is the usage of a readout chip with a fast shaping time, in the order of 50 ns. For this, the SVD inherited the APV25

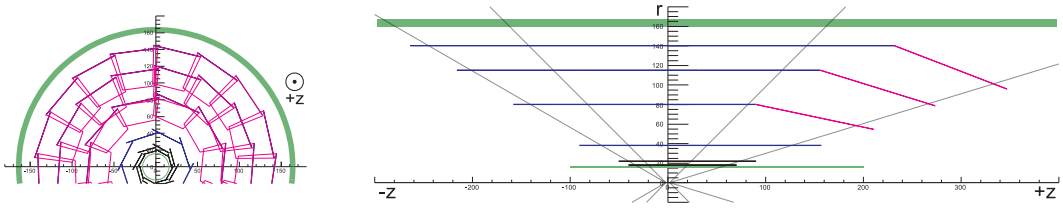

Figure 4.5: Schematic view of the SVD. In the left panel the xy view is shown. In the right panel the longitudinal cross section (r-z plane) is shown. The slanted forward sensors of L4, L5, and L6 are depicted in magenta. In both panels the two PXD layers are shown, as well. Figure taken from Ref. [121].

chips [134] — first used in the tracker of the CMS experiment [135] — equipped with 128 channels each and a shaping time of 50 ns. By design, the APV25 chips are radiation hard up to an integrated dose in excess of 30 Mrad. Their multi-peak operational mode, where six (or three) consecutive samples along the shaping curve are recorded with each trigger, ensures a time resolution of the order of 3 ns. In Fig. 4.5 a schematic view of the detector is shown.

Table 4.3: Specifications of the Belle II SVD [133].

Layer	Radius (mm)	Ladders	Sensors	Strips/Sensor $r\phi, z$	Pitch $r\phi, z$ (μm, μm)
3	39	7	14	768, 768	50, 160
4	80	10	30	768, 512	75 to 50, 240
5	104	12	48	768, 512	75 to 50, 240
6	135	16	80	768, 512	75 to 50, 240
Sum		35	172	132 096, 91 648	

CDC: the central tracking device is a wire drift chamber surrounding the VXD. Conceptually, it follows the design if its successful predecessor in Belle, employing the same structure, material, and gas mixture (50% helium He, 50% ethane C_2H_6). In total, the CDC counts over 14 000 sense wires arranged in 56 layers (which, in turn, are organized in 9 superlayers), with two different orientations: *axial*, namely aligned with the solenoidal magnetic field, and *stereo*, namely skewed with respect to the axial wires. The combination of the information coming from both axial and stereo wires makes it possible to reconstruct a full 3D helix track. Apart from its obvious main role in charged tracks reconstruction and momentum measurement, two other key tasks are being performed by the

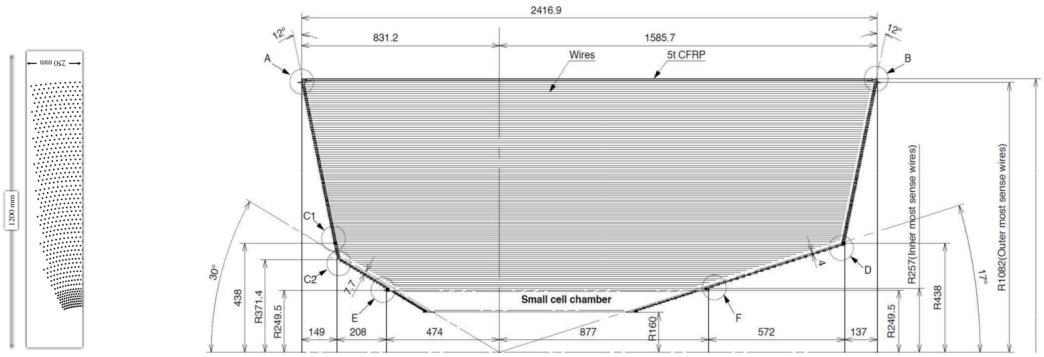

Figure 4.6: Schematic view of the CDC. The small left panel shows the layers configuration in the xy plane. In the main panel the r-z plane is depicted. All measurements are in mm. Figure taken from Ref. [121].

CDC: firstly, it provides Particle IDentification (PID) information exploiting the energy loss $\frac{dE}{dx}$ within its gas volume [11] (in particular, PID of low momentum tracks, which do not reach outermost detectors, relies solely on it). Secondly, it provides reliable trigger signals for events with charged particles.

The main differences with respect to the Belle CDC concern the readout electronics, the cylinder radii, and the addition of three-dimensional trigger information. The readout electronics is required to be much faster than in Belle because of the higher trigger rates. Both the innermost (160 mm) and the outermost (1130 mm) CDC radii are larger than in Belle (77 mm and 880 mm, respectively). These changes are driven by the higher background rates, which would make the chamber unusable at smaller radius, and by the upgraded thinner PID detectors in the central region (*barrel*) of the experiment (see Section 4.2.2). In addition, a 3D charged tracks trigger is expected to be a robust approach against high beam background, and has the advantage of not requiring additional material. In Fig. 4.6 a schematic view of the detector is shown. Its main specifications are summarized in Table 4.4.

Table 4.4: Specifications of the Belle II CDC [133].

Layer	sense wires r (mm)	# of wires	Drift Cell Size (cm)	Average Resolution (μm)
1 to 56	168 to 1111.4	160 to 384	∼1 to ∼2	120

4.2.2 Particle identification subsystems

PID is a crucial aspect of the experiment since it allows to distinguish between final state hadrons and leptons. Two subdetectors are specifically [3] devoted to PID: the TOP counter in the barrel region of the detector, and the ARICH situated in the FW endcap. Both subsystems exploit the Cherenkov effect [11] to distinguish between different charged particles.

TOP: as central PID device for Belle II, the TOP counter [136] measures the time of propagation of Cherenkov photons internally reflected inside quartz radiators. The Cherenkov image is fully reconstructed thanks to the three-dimensional information provided by two-dimensional space information (x, y) and precise timing information. The latter is determined using Micro-Channel Plate (MCP) PhotoMultiplier Tubes (PMTs) situated at the BW surface of each quartz radiator. A mirror placed at the FW end surface reflects back the photons emitted in such a direction, which are then also eventually collected by the PMTs. A focusing system is included in the design in order to minimize chromatic effects responsible for broadening the time resolution. The TOP counter is composed of 16 detector modules — each of which consists of two quartz radiators glued together and is in total 2500 mm long, 450 mm wide, and 20 mm thick. The detector angular acceptance is $\theta \in [31°, 128°]$, covering, as mentioned, only the barrel region.

ARICH: the ARICH is a proximity focusing ring-imaging detector, which uses aerogel tiles as radiator and provides PID information in the FW endcap region of the experiment. The emitted Cherenkov photons propagate through 20 cm of expansion volume before hitting the Hybrid Avalanche Photo-Detectors (HAPDs), and thus creating the well known ring-like images. To improve the performance, and in particular to increase the number of emitted photons without paying the price of degrading the Cherenkov angle resolution, two aerogel layers with slightly different refraction indices ($n_1 = 1.045$ upstream, $n_2 = 1.055$ downstream) are used. Each of the two aerogel layers has a thickness of 2 cm. Such a combination of layers with appropriately tuned refractive indices gives rise to overlapping rings and reduces the spread due to the emission point uncertainty.

[3] As already mentioned, also the CDC provides PID information, but this is not its solely purpose.

4.2.3 Outermost structures

Together with the above-mentioned tracking and PID devices, two other subsystems complete the Belle II design: a calorimeter that plays a fundamental role for neutral particle detection, the ECL, and a neutral long-lived kaon K_L and muon (μ) detector, the KLM. Also extremely important, a superconducting solenoid located between these two subdetectors provides a homogeneous magnetic field of 1.5 T, parallel to the beam direction. The return yoke for the magnetic field is provided by the iron structure of the KLM.

ECL: the ECL is a homogeneous highly-segmented array of thallium-doped caesium iodide CsI(Tl) crystals, covering all three regions of the detector (barrel, FW and BW endcaps). Its main purpose is the detection of photons from B meson decays with high efficiency and good energy and position resolutions. The detector consists of over 8700 crystals that cover about 90% of the solid angle in the center-of-mass system. The average surface and length of the crystals are $\sim 6 \times 6$ cm^2 and 30 cm (16.1 radiation lengths X_0), respectively. The polar angle acceptance is $\theta \in [12.4°, 155.1°]$, with the exception of two gaps $\sim 1°$ wide between the barrel and each endcap [137]. Each crystal has a tower-like shape and is arranged so that it points almost to the IP. While the crystals, the supporting structure, and the preamplifiers remained the same as for Belle, the readout electronics has been replaced: the photo-sensors are now equipped with wave-form-sampling readout electronics. Such a choice was dictated by the need to cope with an increased background rate and larger pile-up noise. The intrinsic energy resolution of the ECL, as measured using a prototype [121, 138], can be approximated as:

$$\frac{\sigma_E}{E} = \sqrt{\left(\frac{0.066\%}{E}\right)^2 + \left(\frac{0.81\%}{\sqrt[4]{E}}\right)^2 + (1.34\%)^2}, \tag{4.2}$$

where E is the energy in GeV.

KLM: the KLM consists of alternating layers of iron plates and active detector elements, and it is located outside the superconducting coil. As the name suggests, the task of such a detector is to reconstruct K_L mesons and identify muons (μ). The iron plates are each 4.7 cm thick and serve as magnetic flux return for the solenoid. In addition, they provide the material budget for 3.9 nuclear interaction lengths (λ_0) — while the ECL provides 0.8 λ_0 — allowing K_L to hadronically shower in its volume. The KLM covers all three regions of the

detector, with a total polar angle acceptance of $\theta \in [20°, 155]°$. Differently from Belle, in some of the detector areas — both endcap regions and the two innermost barrel layers — the former Resistive Plate Chambers (RPCs) have been replaced by layers of scintillator strips with wavelength shifting fibers read out by Silicon PhotoMultipliers (SiPMs) as light sensors. This is because the dead time of RPCs is too long to sustain the background rate expected in these regions.

There are several aspects where the Belle II detector, thanks to its new design and technology, is expected to offer considerably better performance with respect to Belle. In particular, being of more interest for the topic discussed in this dissertation, three things can be stated about improvement in tracking-related matters: the vertex resolution benefits from the position of the innermost VXD layers (closer to the IP), the K_s reconstruction efficiency takes advantage of the considerably larger radius of the VXD outermost layers, and the tracking volume is extended thanks to the larger CDC radius.

5

Tracking at Belle II

A fundamental feature of all high energy experiments is to supplement high performance detectors with dedicated software in order to fully exploit their capabilities. The functions of the software are numerous, ranging from the selection of interesting events (trigger) to the conversion of the different subdetector signals into particles with physical properties, providing the analyst with a description of the physical events (event reconstruction). Of particular interest to this dissertation is the tracking reconstruction chain, the part that takes care of finding and fitting charged tracks starting from the hit-level information provided by the three main tracking detectors (PXD, SVD, and CDC).

In this chapter, the tracking algorithms of Belle II will be described. After a description of the tracking challenges and the role played by the beam background here (Section 5.1), the track parametrization will be introduced (Section 5.2), followed by a description of the tracking algorithms relative to pattern recognition (Section 5.3) and track fitting (Section 5.4). The last part of the chapter will be devoted to show the tracking performance in Monte Carlo (MC) (Section 5.5). For an in-depth description of the tracking algorithms used in the Belle II experiment one should refer to [133].

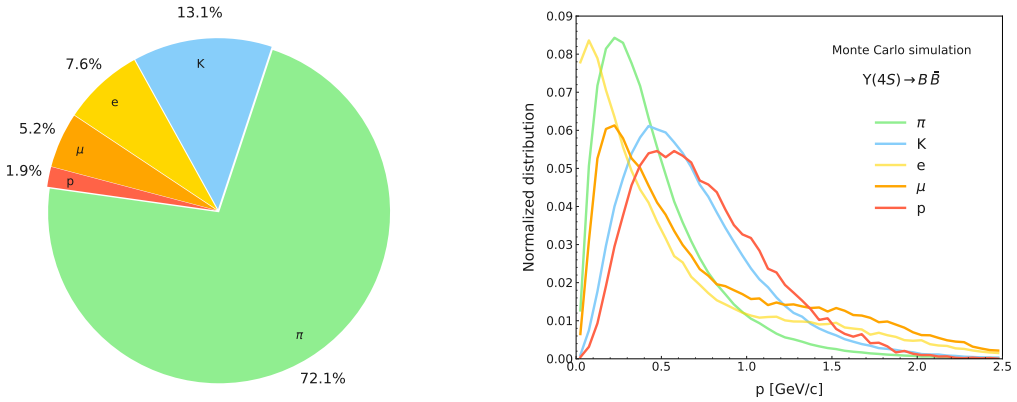

Figure 5.1: Characteristics of $\Upsilon(4S) \to B\bar{B}$ events. In the left panel the relative abundance of the long-lived charged particles is shown, while in the right panel their momentum spectra are shown. Each curve in the right panel is normalized to the total number of tracks from the respective type. Both figures were obtained from a MC simulation, generating 10^5 events with the EvtGen package [139].

5.1 Tracking challenges

As already mentioned, most of the Belle II physics program relies on events in which the annihilation of an electron-positron pair produces a $\Upsilon(4S)$ resonance. In more than 96% of the cases, the $\Upsilon(4S)$ resonance decays promptly into a pair of B mesons [11]. On average, such $B\bar{B}$ events are characterized in the final state by approximately 11 charged tracks with quite soft momentum spectra. Figure 5.1 shows the relative abundance of the long-lived charged particles produced in these events (left panel) and their momentum spectra (right panel). The plots were obtained from a MC simulation, generating 10^5 $\Upsilon(4S) \to B\bar{B}$ events with the EvtGen package [139].

As it can be seen in Fig. 5.1, most of the long-lived charged particles have momenta well below 1 GeV/c. Low momentum particles represent a challenge from a track finding point of view: the trajectories of particles with momentum below 200 MeV/c are heavily affected by multiple scattering and energy loss in the material, and in such a low momentum region most of the tracks do not reach the CDC, and the only available hit information for their reconstruction comes from the VXD layers. Soft momentum tracks reaching the CDC represent a challenge as well: particles with momentum below 300 MeV/c can loop several times within the subdetector volume, creating hundreds of hits.

On top of such challenges arising from the event topology, the occupancy due to beam background is expected to be very high [128]: SuperKEKB's high beam currents, small emittances, and large beam-beam tune shifts — key fea-

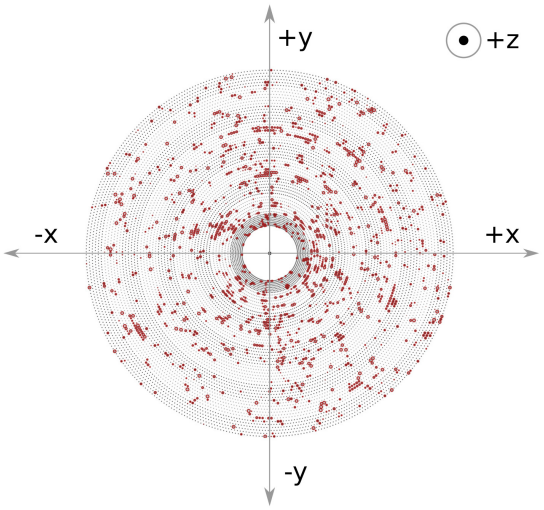

Figure 5.2: Simulated beam background in the CDC, assuming the nominal instantaneous luminosity. Figure adapted from Ref. [133].

tures to reach the design luminosity — contribute to increasing the rate of beam background hits.

5.1.1 Beam background sources

"Beam background" is an umbrella term encompassing background particles generated by the accelerator, both by single-beam and luminosity-dependent processes. There are five main beam background sources at SuperKEKB: Touschek scattering, beam-gas scattering, synchrotron radiation, radiative Bhabha scattering, and two-photon process. The first three are single-beam processes, while the last two are luminosity-dependent processes.

Touschek scattering: it arises from an intrabunch scattering process, where the Coulomb scattering of two particles in the same beam bunch changes the particles' energies. One of the particles ends up with a higher energy, the other with a lower energy, both deviating from the nominal energy and from the stable beam. The scattered particles are usually lost at the beam pipe inner wall during the propagation through the ring, thus if the loss happens close to the IP the detector might be hit by the so-originating shower. Such an effect depends on the third power of the beam energy and it is inversely proportional to the beam size. The expected rate at SuperKEKB, obtained with a simple extrapolation based on beam sizes, is $\sim$ 20 times higher compared to KEKB. Movable collimators

(both horizontal and vertical) and metal shields are used to mitigate it.

Beam-gas scattering: it arises from the scattering of beam particles by residual gas molecules in the beam pipe, that can occur either via Coulomb scattering (process that changes the direction of the beam particle) or Bremsstrahlung scattering (process that decreases the energy of the beam particle through photon emission), with the former being the dominant component. Its rate is expected to be a factor of ~ 100 higher in SuperKEKB with respect to KEKB, as a consequence of the reduced beam pipe radius. The same countermeasures used for Touschek background — movable collimators and heavy-metal shields — are also effective at reducing beam-gas background, though with special considerations for the width of vertical collimators [128].

Synchrotron radiation: the synchrotron radiation emitted by the beam, consisting of accelerated particles, is another source of beam background. The radiation power is proportional to the square of the magnetic field strength and of the beam energy. It follows that the HER beam is the primary source of such a background. The synchrotron radiation spectrum spans from few keV to tens of keV and, as demonstrated by past experience [1], it may severely damage the inner detectors. To mitigate this effect, the beam pipe in the interaction region has a special design including ridge structures — in order to avoid direct synchrotron radiation reaching the inner detectors — and its inner wall is laminated with a gold layer which absorbs photons propagating in the direction of the innermost detectors.

Radiative Bhabha scattering: it arises from photons produced by the radiative Bhabha process that propagate along the beam axis direction and interact with the iron of the accelerator magnets. As a consequence of these interactions, low energy gamma rays and neutrons are produced abundantly. Low energy gammas represent a source of background mainly for the CDC and the TOP, while neutrons represent the main background source for the KLM. The production rate for radiative Bhabha scattering is proportional to the luminosity, so this background is expected to be ~ 40 times higher than at KEKB. To stop these neutrons, a dedicated neutron shielding in the accelerator tunnel is required. Furthermore, in SuperKEKB two separated final focus quadrupole magnets are

[1] During early running of KEKB the inner layer of the Belle SVD was severely damaged by X-rays with E $\sim$ 2 keV from the HER.

used to center the beams and to mitigate the beam losses due to the radiative scattering.

Two-photon process: this background source originates from low momentum electron-positron pairs resulting from two-photon processes $e^+e^- \rightarrow e^+e^-e^+e^-$. With their soft momentum, such pairs can spiral in the solenoid field and leave many hits in the inner detectors.

At the planned instantaneous luminosity the number of background hits is expected to exceed the signal hits by two orders of magnitude, posing a very challenging task for the tracking detectors and for the software reconstruction. Figure 5.2 shows an example of beam background hits in the CDC assuming nominal phase 3 instantaneous luminosity.

5.2 Track parametrization

Generally speaking, the trajectory of a particle in empty space is determined — in Cartesian coordinates — by its position $\vec{x}$ and momentum $\vec{p}$ at some given time. For charged particles moving in a magnetic field generated by a solenoid, these trajectories can be parametrized with five-parameter helices. In Belle II it was chosen to use a perigee-parametrized helix: the helix is defined at its Point Of Closest Approach (POCA) to the origin of the coordinate system, namely the perigee.

The five parameters stored for each track are:

- $d_0 \in [-\infty, +\infty]$: signed distance of the POCA with respect to the z-axis;
- $z_0 \in [-\infty, +\infty]$: z coordinate of the POCA;
- $\phi_0 \in [-\pi, +\pi]$: angle defined by the transverse momentum at the POCA and the x-axis;
- $\omega \in [-\infty, +\infty]$: inverse of the radius of curvature signed with the particle's charge;
- $tan\lambda \in [-\infty, +\infty]$: tangent of the angle defined by the momentum at the POCA and the xy-plane.

A depiction of the helix and of the parameters listed above can be seen in Fig. 5.3. The relation between Cartesian and perigee coordinates can be found in Appendix A.

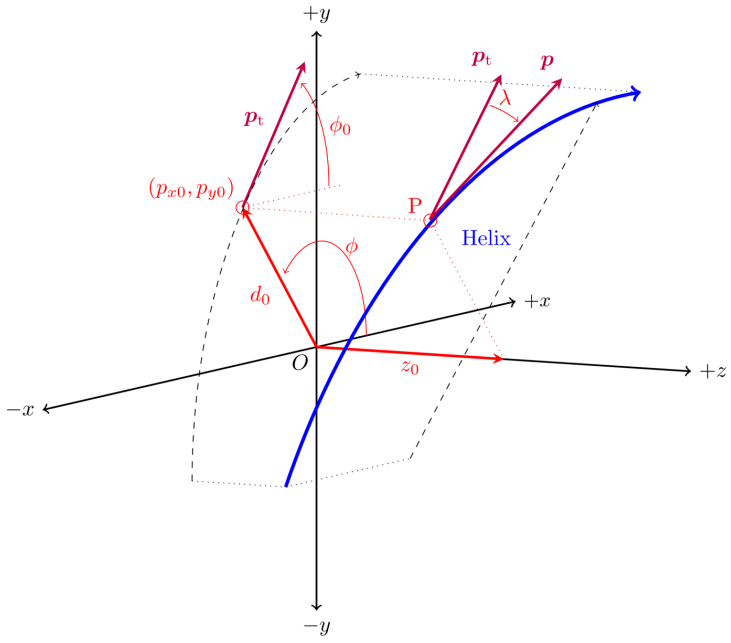

Figure 5.3: Perigee parametrization of the track helix. A description of the parameters can be found in the text. Figure taken from Ref. [140].

5.3 Track finding

The track finding, or pattern recognition, is the part of the software responsible for transforming the hit information coming from the tracking detectors into *track candidates*, sorting the hits belonging to a single charged particle and discarding those originating from background. Thanks to the modularity of the Belle II analysis software framework [141], the tracking chain can be adapted to different background levels and detector performance simply by switching the order in which the individual modules are executed. The first steps of the pattern recognition rely on SVD and CDC hits only. In order to optimize the final performance, the tracking chain alternates stages of pattern recognition and fitting, and different finding algorithms are exploited for each subdetector: standalone CDC track finding, standalone SVD track finding, and inter-detector hit finding based on a Combinatorial Kalman Filter (CKF) [142]. For the various fitting steps a Deterministic Annealing Filter (DAF) is employed [143]. In its current design, the tracking chain workflow starts from a standalone CDC track finding. The obtained CDC track candidates are then fitted and extrapolated inwards to attach SVD hits. The unused SVD hits are employed for a standalone SVD track finding, and the resulting tracks, after a fitting step, are extrapolated outwards to attach CDC hits. Finally, after merging CDC and SVD tracks, they are ex-

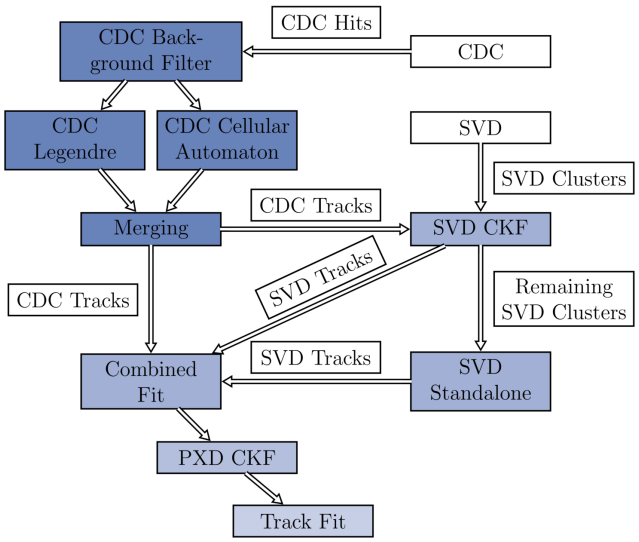

Figure 5.4: Schematic representation of the Belle II tracking chain. Figure taken from Ref. [133].

trapolated inwards to attach PXD hits before the final step of track fitting. PXD hits are added as a last step of the pattern recognition to improve the quality of the tracks. Figure 5.4 shows a schematic representation of the Belle II tracking chain in its current design.

CDC track finding: it represents the first building block of the tracking chain. Two distinct algorithms are used for the pattern recognition in the CDC: a global one, based on the Legendre transformation [144], and a local one, based on the cellular automaton concept [145]. Being executed first, the primary algorithm is — currently — the global one. Such an algorithm, however, comes with the downside of assuming that each track originates from the IP, therefore the local algorithm helps with reconstructing displaced tracks which originate far away from it. In order to exploit their specific benefits, both algorithms get as input the full set of CDC hits. The final collection of standalone CDC track candidates is then obtained thanks to a multivariate approach, based on a Fast Boosted Decision Tree (FastBDT) [146], that adds the local track candidates to the global ones. Such FastBDT is trained using simulated events.

SVD track finding: the SVD standalone pattern recognition is called *VXDTF2*. In the 4 SVD layers the number of possible 3D hit (*SpacePoint*) combinations is huge. In order to reduce it, the concept of *SectorMaps* is introduced: each SVD sensor is divided into M×N sectors. Possible combinations of SpacePoints are

searched only on friend sectors, where such "friendship relations" are established using MC simulation during a dedicated training of the SectorMaps. Finally, the resulting compatible SpacePoint combinations are used to build the final collection of SVD track candidates exploiting a cellular automaton algorithm.

Combinatorial Kalman Filter: the CKF is an iterative local algorithm capable of producing high-purity tracks also in environments characterized by high hit densities. Starting with a seed estimation of the track parameters with uncertainties, the track candidate is extrapolated into the detector volume, iteratively adding to it the compatible hit candidates. The algorithm offers the possibility of including non-uniform magnetic field, energy loss and multiple scattering effects. The CKF is widely used in the Belle II tracking package: CDC track candidates are extrapolated inwards to the SVD, SVD track candidates are extrapolated outwards to the CDC, and CDC+SVD track candidates are extrapolated inwards to the PXD. The possibility to extrapolate CDC tracks outwards to the ECL is contemplated, even though at the moment it is not part of the standard reconstruction chain. In particular, attaching PXD hits to the tracks improves the resolution of the track parameters d_0 and z_0 by a factor of two and more [140], which is a key requirement for precision measurements.

5.4 Track fitting

The final step of the tracking chain, after the track finding block, consists of a final track fitting using the DAF algorithm provided by the GENFIT2 package [143]. In order to correctly calculate the energy loss and the material effects, a specific particle hypothesis has to be assumed. The strategy of Belle II is to fit all reconstructed tracks with three different particle hypotheses — pion (π), kaon (K), and proton (p) — and to store all three track fit results. This allows the analysts to use the best hypothesis, once the PID information is available.

5.5 Evaluating Tracking Performance

The most immediate way to evaluate the tracking performance is to use MC samples: having the exact knowledge of what was generated and analyzing the reconstructed particles can tell us how well the algorithms work. The obvious drawback of using MC is that it considers only the simulated detector response, which is somewhat idealized. Studies to evaluate the tracking performance using

data are currently ongoing in the Belle II tracking group. However, they are not subject of this thesis and will not be discussed here.

In order to evaluate the tracking performance in this context, four different Figure Of Merits (FOMs) has been used: efficiency, purity, clone rate, and fake rate. The efficiency measures the fraction of reconstructed MC particles. A MC particle is defined as reconstructed when it has an associated track candidate, in this context referred to as RecoTrack (RT). Only primary MC particles inside the detector acceptance are considered, so those for which there should be hits left in the detector and the reconstruction should be possible. Formally, the efficiency is defined as the ratio between the number of MC particles with an associated RT and the total number of MC particles:

$$\text{Efficiency} = \frac{\#\text{ MC particles with an associated RT}}{\#\text{ MC particles}}. \tag{5.1}$$

In order to understand the other three FOMs, a classification for RTs should be introduced. A RT can be *matched*, *clone*, or *fake*. A RT is *matched* when it contains a high contribution from only one MC particle and it is the best among all RTs describing that same MC particle. A *clone* is a RT that contains a high contribution from only one MC particle, but it is not the best that exists, i.e. there is another RT containing an even higher contribution from that same MC particle. A *fake* is a RT which is not *matched* nor *clone*. On this basis, the purity evaluates the fraction of matched RTs:

$$\text{Purity} = \frac{\#\text{ matched RT}}{\#\text{ RT}}. \tag{5.2}$$

The clone rate evaluates the fraction of clone RT:

$$\text{Clone Rate} = \frac{\#\text{ clone RT}}{\#\text{ RT}}. \tag{5.3}$$

Finally, the fake rate evaluates the fraction of fake RT:

$$\text{Fake Rate} = \frac{\#\text{ fake RT}}{\#\text{ RT}}. \tag{5.4}$$

The tracking performance shown in this section was obtained using a total of 2×10^5 simulated $\Upsilon(4S) \to B\bar{B}$ events, of which 10^5 $\Upsilon(4S) \to B^+B^-$ events and 10^5 $\Upsilon(4S) \to B^0\bar{B}^0$ events. In order to reproduce realistic conditions simulated beam background was used as well. As discussed at the beginning of the chapter, the beam background composition strongly depends on the assumed

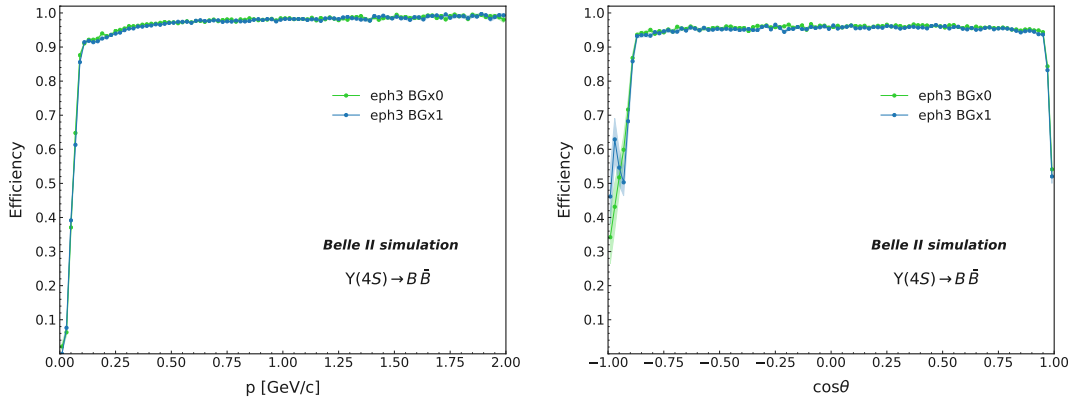

Figure 5.5: Tracking efficiency. The panel on the left shows the efficiency as a function of the particle momentum, while the panel on the right shows the efficiency as a function of the cosine of its polar angle. In each panel two different samples are shown: one without (green curves) and one with (blue curves) simulated beam background. The definition of efficiency is given in Eq. (5.1). The overall efficiency is higher than 95% for both samples.

beam conditions and, therefore, on the data taking period. The level of simulated background used for the studies presented in this and in the following chapters is labeled as "eph3 BGx1" (early phase 3, background x1), namely the background level expected in the first period of the data taking. As a comparison, in this chapter a sample without beam background, labeled as "eph3 BGx0", is used as well. Later in this dissertation, the effect of different background levels on the performance will be presented and discussed (Chapter 8).

Figure 5.5 shows the tracking efficiency (defined in Eq. (5.1)), both as a function of the particle momentum (left panel) and of the cosine of its polar angle (right panel). In both panels the efficiency profile is shown for the two different samples, without (eph3 BGx0) and with simulated background (eph3 BGx1). The overall efficiency is higher than 95% for both samples, and the difference between the two is less than 0.4%, which demonstrates the excellent tracking performance in the early data taking background scenario. Looking at the figure it is evident how the most difficult tracks to reconstruct are those with low momentum and in the most FW and BW regions of the detector.

Figure 5.6 shows the tracking purity (Eq. (5.2)), clone rate (Eq. (5.3)), and fake rate (Eq. (5.4)), both as a function of the particle momentum (left panel) and the cosine of its polar angle (right panel). In this case, only the MC sample with simulated background, the most realistic configuration, is shown. As can be seen from the distributions, the clone and fake rates are higher at low momentum, as

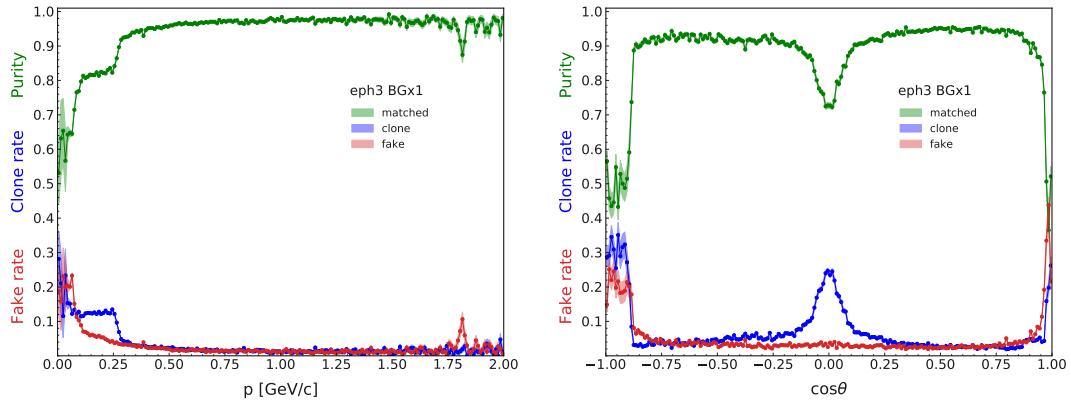

Figure 5.6: Tracking purity (matched), clone rate, and fake rate. The panel on the left shows these quantities as a function of the particle momentum, while the panel on the right shows them as a function of the cosine of the particle polar angle. Their definitions are given in Eqs. (5.2) to (5.4), respectively. In this figure only the sample with beam background (eph3 BGx1) is shown.

Table 5.1: Overall tracking performance evaluated both using a MC sample without (eph3 BGx0) and with (eph3 BGx1) simulated background.

	efficiency (%)	purity (%)	clone rate (%)	fake rate (%)
eph3 BGx0	95.48 ± 0.03	91.38 ± 0.04	5.88 ± 0.03	2.74 ± 0.02
eph3 BGx1	95.09 ± 0.03	90.87 ± 0.04	5.52 ± 0.03	3.61 ± 0.03

opposed to the purity. An enhancement (drop) in the clone rate (purity) is visible for $\cos\theta \sim 0$, which is the direction perpendicular to the beam. A summary of the overall tracking performance, both for the sample without and with beam background, can be found in Table 5.1.

Finally, the effect of using three different particle hypotheses in the track fitting — described in Section 5.4 — is shown in Fig. 5.7. Also in this case the plots were obtained using the sample with simulated background. The left panel shows the momentum resolution of a MC pion sample fitted with pion (green), kaon (blue), and proton (red) hypothesis. The central panel shows the momentum resolution of a MC kaon sample fitted with pion (green), kaon (blue), and proton (red) hypothesis. The right panel shows the momentum resolution of a MC proton sample fitted with pion (green), kaon (blue), and proton (red) hypothesis. In all cases, the best resolution is obtained when using the hypothesis corresponding to the generated particle for the fit. This resolution improvement is more evident for low momentum particles (see Fig. B.1).

This chapter presented the various aspects of tracking at Belle II, which rep-

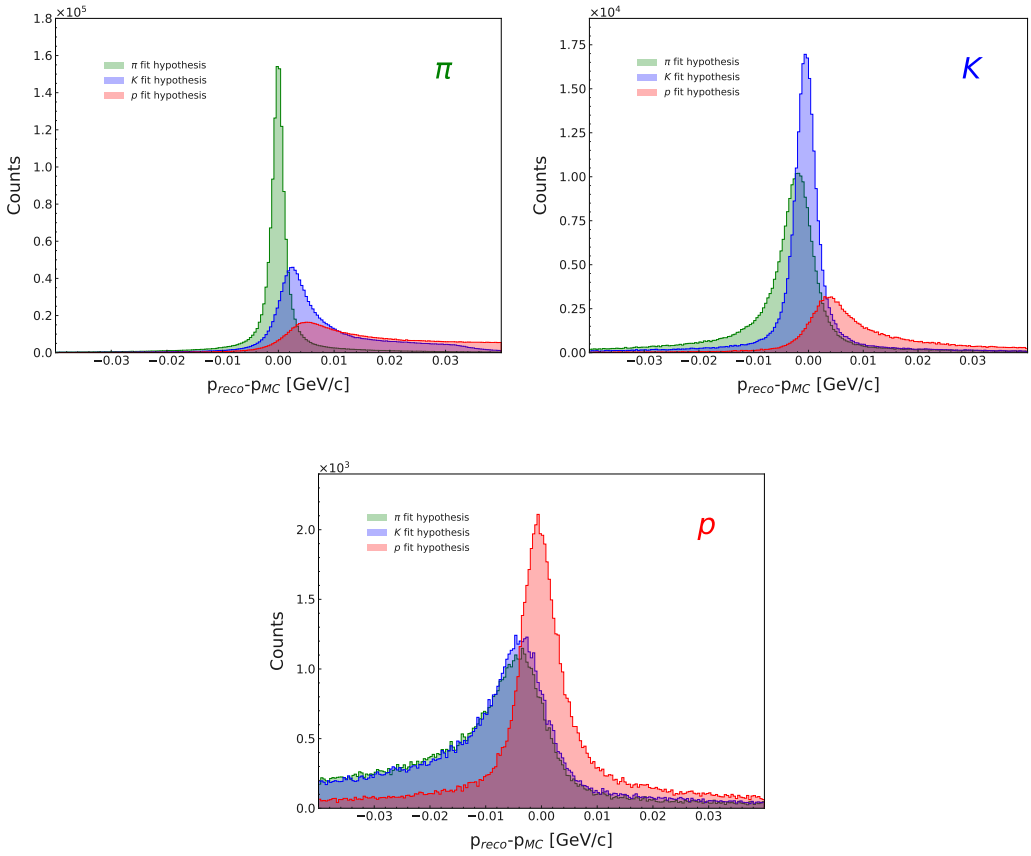

Figure 5.7: Momentum resolution of tracks fitted with different hypotheses. In the top left (top right/bottom) panel, generated pions (kaons/protons) were fitted with pion (green), kaon (blue), and proton (red) hypothesis. In all cases the best resolution is given by fit hypothesis corresponding to the generated particle.

resents the building block for the reconstruction of all decays involving charged tracks. In particular, in the second part of the chapter its excellent performance in the early data taking background scenario were shown. The kinematics regions where the performance is worst turn out to be the low momentum region and the regions at the limits of the angular acceptance. As we shall see in the next chapter, the low momentum region will play an important role in the reconstruction of Λ baryons decaying into $p\pi$, whose pion has a fairly soft momentum spectrum.

6

Displaced vertices and Λ reconstruction

The reconstruction of charged tracks — extensively described in the previous chapter — plays a fundamental role in the identification of a special category of objects, so called V0s. These are neutral particles with mean proper decay length $c\tau$ in the order of a few centimeters decaying into pairs of charged tracks. The term "V0" primarily refers to K_s and Λ and has historical origins [147]: in a bubble chamber, two charged particles originating from a neutral one leave a "V" shape as a trace.

Of particular interest for this dissertation are Λ baryons, since they are involved in most of the possible decay channels of the double strange hexaquark. For ease of understanding, "Λ" will refer to both Λ^0 and its antiparticle $\bar{\Lambda}^0$, unless explicitly stated otherwise. After an introduction on the reconstruction of generic decays at Belle II (Section 6.1), the reconstruction of V0 particles will be described and its performance using MC will be shown (Section 6.2). The last part of the chapter will be devoted to describing an optimized selection for Λ baryons and its performance (Section 6.3). This selection is then going to be used for the double strange hexaquark search sensitivity studies described in the next chapter (Chapter 7). Part of this work is also described in an internal Belle II

note, written by the author of the thesis herself [148].

6.1 Reconstruction of generic decays

The reconstruction of final state particles represents the building block for the reconstruction of all unstable particles and, more generally, all decay chains. The reconstruction of charged tracks was extensively described in the previous chapter. The reconstruction of neutral particles, the other key element in a general decay reconstruction, is not relevant for this thesis and is therefore not described here. More information about it can be found in Ref. [121]. In Belle II, unstable particles are reconstructed, by specifying their decay mode, via the combination of final state particles collected in *particle lists*. All possible combinations are created, and, among them, those who pass some specified selections are saved to a new particle list. Once created, each particle list can be used in the reconstruction of the next decay. In case of decay chains, one must start with the final state particles and proceed upstream with the reconstruction algorithm. Depending on the decay considered, the simple combination of particles can be followed by a vertex fit or other requirements to be met in order to improve the reconstruction. As a basic example — useful for the arguments discussed in this thesis — one can consider the decay of a Λ baryon in two charged tracks, $\Lambda \to p\pi^-$. In this case, the Λ candidates are reconstructed starting from two lists of charged tracks, a list of protons and a list of pions. Each particle in the two lists carries the information about its track parameters, but no hit-level information. A common selection criterion in such a case is the requirement that the invariant mass of the new particle lies in a range centered around the Λ nominal mass value: all the candidates that fulfill this requirement are saved in a new list of Λ particles.

6.2 V0 reconstruction

In the Belle II analysis framework, V0s represent a particular class of particles for which a special treatment is reserved. From a practical point of view they are nothing else than pairs of charged tracks with a common vertex that is usually displaced from the IP. If for charged particles originating close to the IP the track parameters extrapolated at the POCA (described in Section 5.2) provide a very good approximation, a two-track vertex fit far from the IP can really benefit from the whole hit pattern information of the two tracks. While saving hundreds of hits for each track, instead of just five parameters, is out of question from a resource

usage point of view, for V0 candidates the hits information is fully exploited in a preliminary vertex fit during the event reconstruction phase, before being lost. For this purpose, a dedicated module is executed as part of the standard tracking chain: a vertex fit is performed for each possible V0, i.e. each pair of track candidates with opposite charge sign, and every time it succeeds a *V0 object* is stored to be available to analysts at a later stage. Such an object consists of the two charged tracks with modified track parameters, that for displaced vertices result more accurate than the original ones. No V0 with a vertex inside the beam pipe is saved at this stage, but they are recovered in a following step. As a matter of fact, the standard method used to reconstruct generic decays and the specific reconstruction for V0s are not meant to be mutually exclusive but rather to complement each other. At analysis level, the analyst interested in K_s or Λ uses a particle list resulting from merging together two lists obtained with the two methods. In case the same candidate is found in both lists, only one of the two is kept. No selection other than a successful vertex fit and a loose mass cut ($M_{K_s} \in [0.45, 0.55]$ GeV/c^2, $M_\Lambda \in [1.10, 1.13]$ GeV/c^2) is applied to such merged lists, keeping the samples very inclusive. Figure 6.1 shows the invariant mass peaks of K_s candidates (left panel) and Λ candidates (right panel), obtained with the procedure just explained. The background contamination is rather high, especially in the case of Λ. A candidate selection is needed but this is left to analysts and depends on the specific requirements of the analyses.

6.2.1 Performance

The figure of merit used to evaluate the V0 performance is the V0 reconstruction efficiency (ϵ_{V0}), namely the fraction of correctly reconstructed V0s. This efficiency definition is naturally different from that of tracking efficiency illustrated in Eq. (5.1). In this case ϵ_{V0} is defined as the ratio between the number of MC V0s whose two MC daughters both have a track associated and the total number of MC V0s. For the MC V0s entering the definition, only those decaying into two charged tracks are considered, and both of the daughters are required to leave a signal in at least one of the main tracking detectors (SVD and CDC). In the definition, they are referred to as "visual MC V0s":

$$\epsilon_{V0} = \frac{\#\text{ visual MC V0s w/ two associated tracks}}{\#\text{ visual MC V0s}}\,. \tag{6.1}$$

The V0 performance shown in the following was evaluated using simulated $\Upsilon(4S) \to B\bar{B}$ events, as for the tracking performance in the previous chapter.

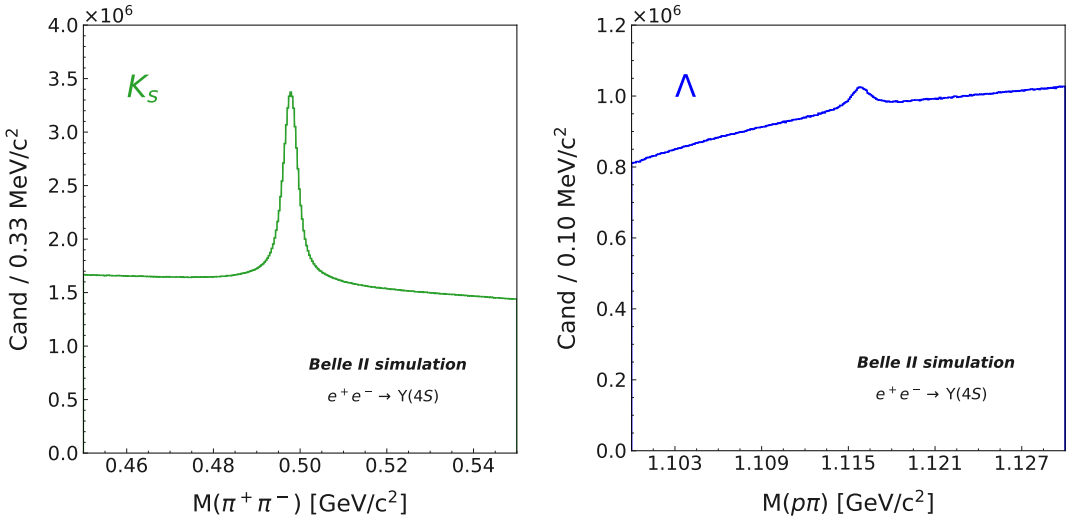

Figure 6.1: V0 candidates invariant mass distribution. The panel on the left shows the $(\pi^+\pi^-)$ invariant mass distribution of K_s candidates, while the panel on the right shows the $(p\pi)$ mass distribution of the Λ candidates. The very inclusive V0 list construction has the consequence of retaining a high background component, and a candidate selection is needed in the analysis step.

In this case a Belle II centrally produced $\Upsilon(4S)$ MC sample was used[1]. The overall V0 reconstruction efficiency is higher for K_s than for Λ: $\epsilon_{K_s} = (82.412 \pm 0.004)\%$ and $\epsilon_\Lambda = (65.73 \pm 0.02)\%$. This difference is mostly due to the different kinematics, and in particular to the difference in momentum distribution of their respective daughters. The momentum distribution both for K_s and Λ daughters in the $\Upsilon(4S) \to B\bar{B}$ events is shown in Fig. 6.2. As it can be seen from the figure, the momentum spectrum of the two K_s daughters is very similar. On the contrary, in the Λ decay the proton tends to carry the largest momentum fraction, while the pion is on average very slow and consequently difficult to reconstruct (as discussed in Section 5.5). Figure 6.3 shows the V0 reconstruction efficiency, both for K_s and Λ, as a function of the V0 flight distance in the transverse plane (left panel) and of the V0 momentum[2] (right panel). In the left panel, one can notice how the efficiency is highest near the IP, it decreases until the second SVD layer (L4), and then stabilizes at an approximately constant value. Looking at the Λ efficiency profile (blue curve) one can notice, as well, small drops corresponding to the last SVD layers (L5 and L6) and the CDC walls. The position of the six VXD layers is shown as vertical dashed lines. In the right panel, the most striking

[1]The MC sample used is from Belle II internal MC13 campaign.

[2]Both variables here refer to the actual V0 particle (K_s or Λ) reconstructed from the original two charged tracks.

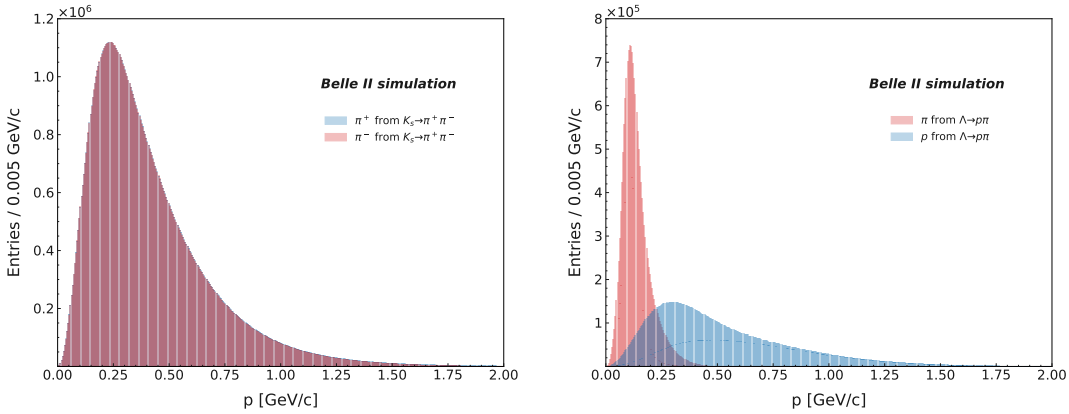

Figure 6.2: Momentum distribution of K_s (left panel) and Λ (right panel) daughters. In the left panel, the blue distribution represents the momentum of the π^+, while the red one represents that of the π^-. The momentum spectrum of the two K_s daughters is very similar, and the two distributions overlap. In the right panel, the blue distribution represents the momentum of the p, while the red one represents that of the π. In this case the two distributions are different. The p from the Λ decay carries in average the largest momentum fraction, while the π is on average very slow.

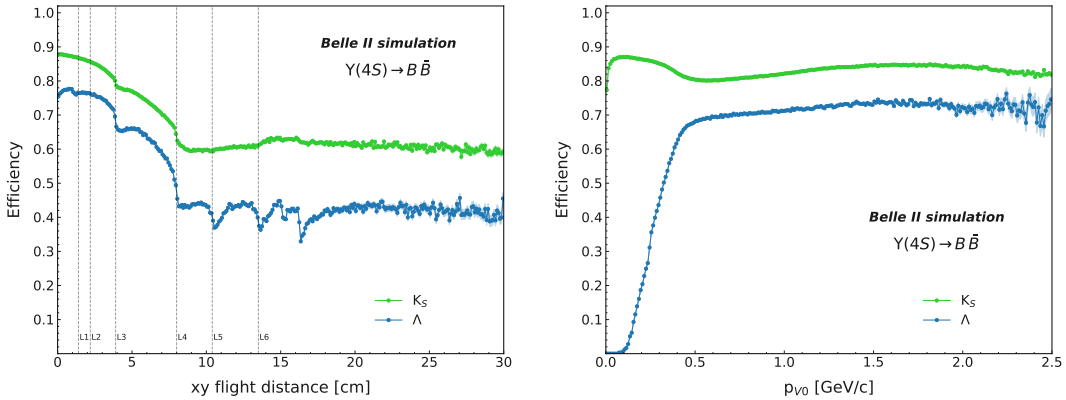

Figure 6.3: V0 efficiency for K_s (green curves) and Λ (blue curves). The panel on the left shows the V0 efficiency as a function of the flight distance in the transverse plane, while the panel on the right shows the V0 efficiency as a function of the V0 momentum. The dashed lines in the left panel show the position of the six VXD layers. The definition of V0 efficiency is given in Eq. (6.1).

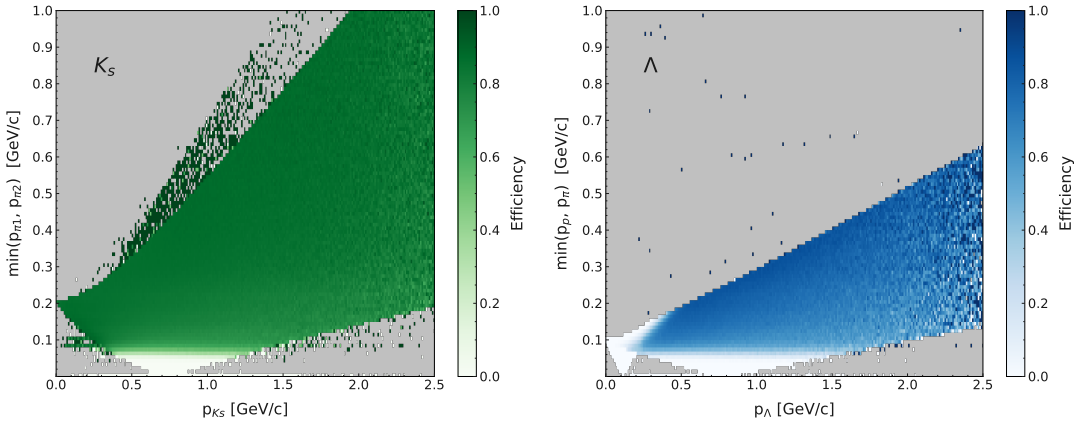

Figure 6.4: 2D V0 efficiency as a function of the V0 momentum (x-axis) and of the lowest momentum among those of the two daughters (y-axis). The left panel shows the 2D V0 efficiency for K_s, while the panel on the right shows it for Λ.

difference between K_s and Λ efficiencies is in the low momentum region: while the K_s reconstruction efficiency is highest at low momentum, the Λ efficiency in the same region is very low. Such a difference is a consequence of kinematics, as well. This can be seen in Fig. 6.4, representing the 2D V0 efficiency as a function of the V0 momentum (x-axis) and the lowest momentum among those of the two daughters (y-axis), for K_s in the left panel and Λ in the right panel. From these plots it can be noticed that for low momentum Λ the lowest of the two daughters' momenta is almost always below 100 MeV/c, making its reconstruction next to impossible. For low momentum K_s instead, this value is higher and thus their reconstruction is easier. In these plots the background color of the panels has been set to gray in order to distinguish it from very low efficiency regions, shown in white.

6.3 Optimization of Λ selection

As already mentioned, the V0 lists provided to analysts are very inclusive and, thus, they contain a large amount of combinatorial background candidates. In the context of the sensitivity study for the double strange hexaquark search, described in detail in the next chapter, the Λ selection needs to be optimized. Since the analysis is targeting a data sample to be collected at the beam energy of the $\Upsilon(3S)$ resonance, the Λ selection has been optimized using a generic $\Upsilon(3S)$ MC sample corresponding to a luminosity of 1 fb^{-1}. For the purposes of the study, the MC truth matching was performed. When used, this returns a variable, *isSignal*, that assumes the value 1 in case the candidate was correctly reconstructed, otherwise 0.

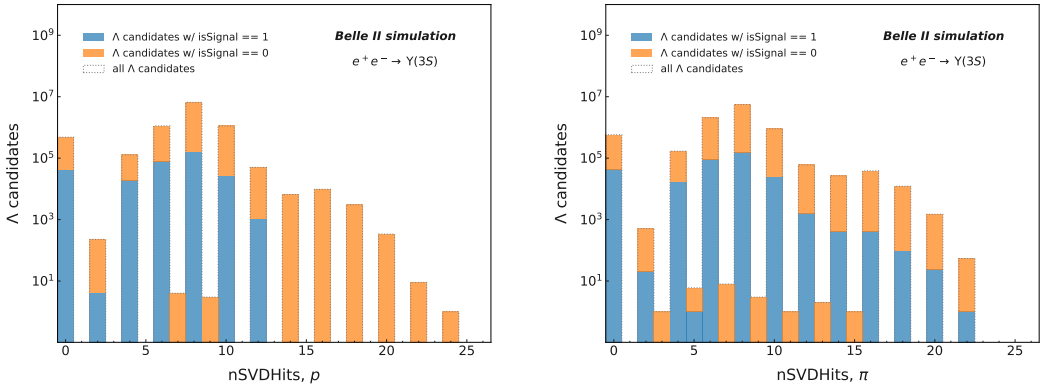

Figure 6.5: Number of SVD hits of the Λ daughters. The panel on the left shows such a variable for the proton, while the panel on the right shows it for the pion daughter. The samples are divided in matched (blue) and non-matched (orange) candidates. Note that in both panels the y-axis is represented in logarithmic scale. For the proton, no signal candidates are found to have more than 12 SVD hits, justifying the cut applied in the selection $nSVDHits, p < 13$.

In the following, matched candidates (namely candidates for which $isSignal = 1$) are also referred to as *signal*, and non-matched candidates ($isSignal = 0$) as *background*.

A quite common procedure in Belle II analyses is to clean up the list of available tracks with cuts on the track parameters d_0 and z_0, restricting them to small regions around the IP. This is indeed a good way to get clean tracks coming from the IP, but it is not ideal in the case of displaced vertices. Instead, for the Λ selection a cut is applied on the number of hits of each daughter track: the pion is required to have at least 1 hit in the CDC ($nCDCHits, \pi > 0$), while the proton is required to have more than 20 hits in the CDC and less than 13 hits in the SVD ($nCDCHits, p > 20$ and $nSVDHits, p < 13$). Generally speaking, requiring the presence of CDC hits implies the rejection of tracks with VXD only information, and a cut on the maximum number of SVD hits removes curlers. Being the SVD a double-sided detector (Section 4.2.1), a track crossing one of its layers leaves a signal on both sides of the layer itself, and, as a consequence, the number of SVD hits of a track is almost always an even number. A track crossing the four SVD layers without curling leave eight hits, while a higher number of hits is an indication of a curler track. In case of protons originating from Λ, the requirement on a maximum number of SVD hits helps in rejecting background. This is shown in Fig. 6.5, representing the number of SVD hits of the Λ daughters, both for matched (blue histogram) and non-matched (orange histogram) Λ candidates.

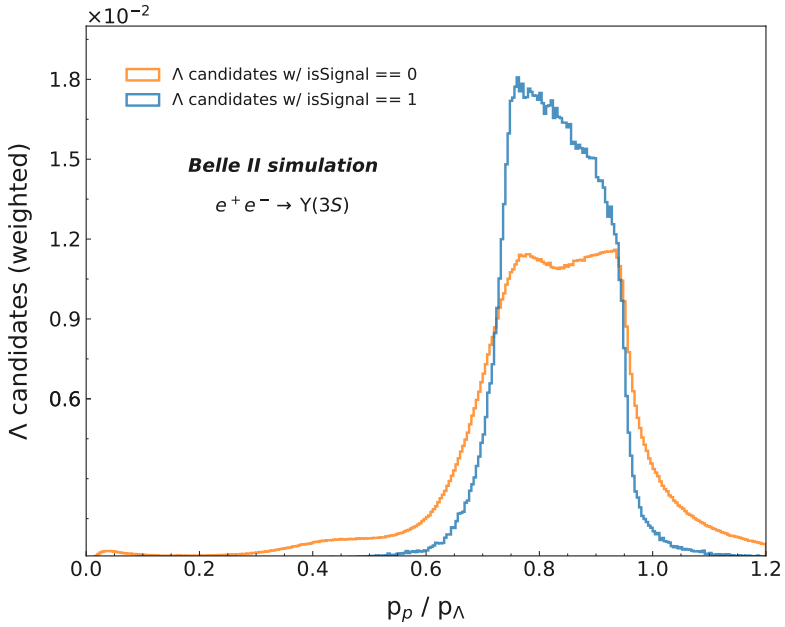

Figure 6.6: Distribution of the ratio between proton and Λ momenta, both for signal (blue histogram) and background candidates (orange histogram). The histograms are normalized to the total number of signal and background candidates, respectively. More than 97% of the signal candidates are located in the range [0.6, 1.0].

None of the protons coming from matched candidates turns out to have more than 12 SVD hits (left panel of Fig. 6.5). On the other hand, this is not the case for the pions (right panel of Fig. 6.5). As further conditions, the proton track is required to match the proton hypothesis (see Section 5.4), and the fraction of proton momentum with respect to that of the Λ is required to range from 0.6 to 1.0 ($0.6 < \frac{p_p}{p_\Lambda} < 1.0$). The latter requirement is a consequence of the different kinematics of the two Λ daughters, with the proton carrying in average the largest momentum fraction (see Fig. 6.2). The cut value can be understood looking at Fig. 6.6, representing the distribution of such a quantity both for signal (blue histogram) and background (orange histogram) candidates. The histograms are normalized to the total number of signal and background candidates, respectively. More than 97% of the signal candidates are located in the selected range.

The effect of this first selection step can be seen in Fig. 6.7, showing the fraction of signal (blue curve) and background (orange curve) candidates surviving after applying it, as a function of the Λ flight distance in the transverse plane (left panel) and of the Λ momentum (right panel). In order to obtain these curves, the number of signal (background) candidates surviving the cuts is normalized

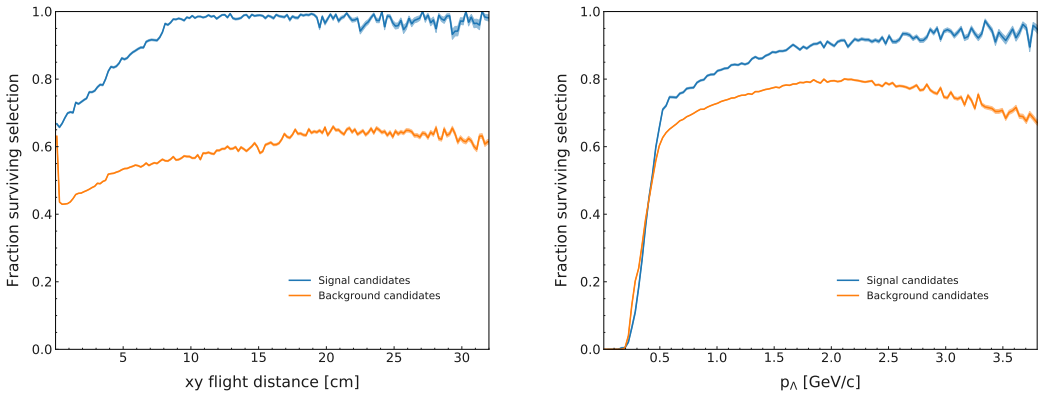

Figure 6.7: Fraction of signal (blue curve) and background (orange curve) candidates surviving the first step of the Λ selection. In the left panel these fractions are represented as a function of the flight distance in the transverse plane, while in the right panel as a function of the Λ candidate momentum. To obtain these fractions, the number of signal (background) candidates surviving the selection was normalized to the number of signal (background) candidates contained in the initial Λ list.

to the number of signal (background) candidates contained in the initial list.

After this first selection step, a momentum-dependent optimization was introduced in order to gain as much as possible in terms of signal retention and background reduction. Seven bins of Λ momentum were defined:

$$p_\Lambda = [(0.0, 0.4), (0.4, 1.0), (1.0, 1.5), (1.5, 2.0), (2.0, 3.0), (3.0, 4.0), (4.0, 6.0)] \text{ GeV/c}. \tag{6.2}$$

Two variables were considered at this stage: *flight significance*, namely the Λ flight distance in units of its uncertainty, and *protonID*, namely the probability of the proton candidate to actually be a proton. It should be noted that the latter variable is defined using PID information as the ratio between the likelihood of the track to be a proton and the sum of likelihoods of it being an electron, muon, pion, kaon, proton, and a deuteron, and it is not related to the particle hypothesis used for the fit. These two variables were chosen because of their high separation power between signal and background. The distribution of the Λ flight significance, both for signal and background candidates, is shown in Fig. 6.8. The two histograms are very different, making it an ideal variable on which to cut. As for the protonID, it has been shown that the relative abundance of protons in $\Upsilon(4S)$ events is low (Fig. 5.1), so in this case using PID information could really be a game changer. This variable can take a value from 0 to 1, representing

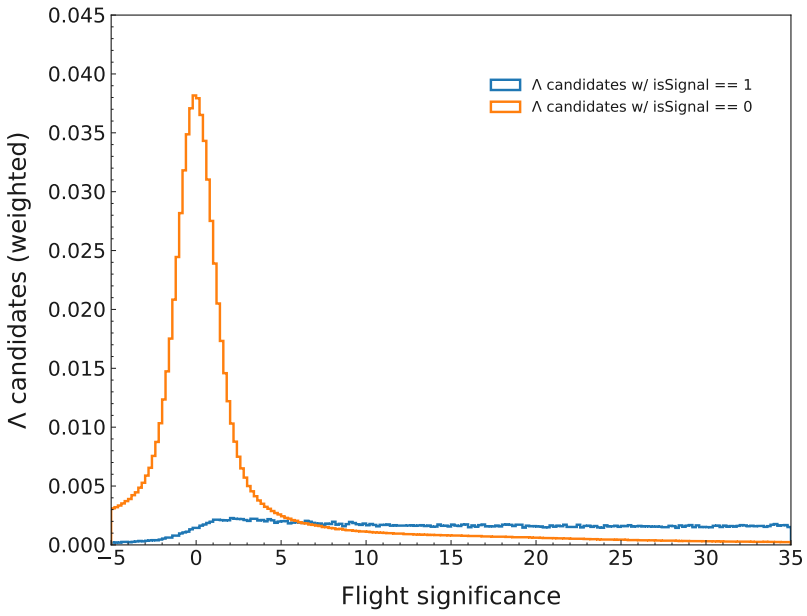

Figure 6.8: Distribution of the Λ flight significance, both for signal (blue histogram) and background candidates (orange histogram). The histograms are normalized to the total number of signal and background candidates, respectively.

the probability that the particle identified as a proton is actually a proton. For each momentum bin $p_{\Lambda,i}$, a 2D FOM was computed as a function of these two variables. In this context the FOM is defined as:

$$FOM = \frac{S}{\sqrt{S+B}}, \tag{6.3}$$

where S represents the number of matched and B the number of non-matched Λ candidates. Each of the 2D FOMs was computed assigning 15 different values to the lower cut on the flight significance — equidistantly spaced in the range (-5.0, 32.5) — and 10 different values to the lower cut on the protonID — equidistantly spaced in the range (0.0, 1.0). One example of such a FOM computation is shown in Fig. 6.9. In this example Λ candidates with momentum p_Λ ranging from 1.0 to 1.5 GeV/c are considered. The FOM of all seven momentum bins can be found in Appendix C. For each momentum bin the pair of cut values maximizing the 2D FOM were selected. Such values were then plotted — separately for the flight significance and protonID variables — as a function of the Λ momentum itself, and the resulting distributions were fitted using phenomenological functions. The choice fell on a 4^{th} order polynomial function in the case of the Λ

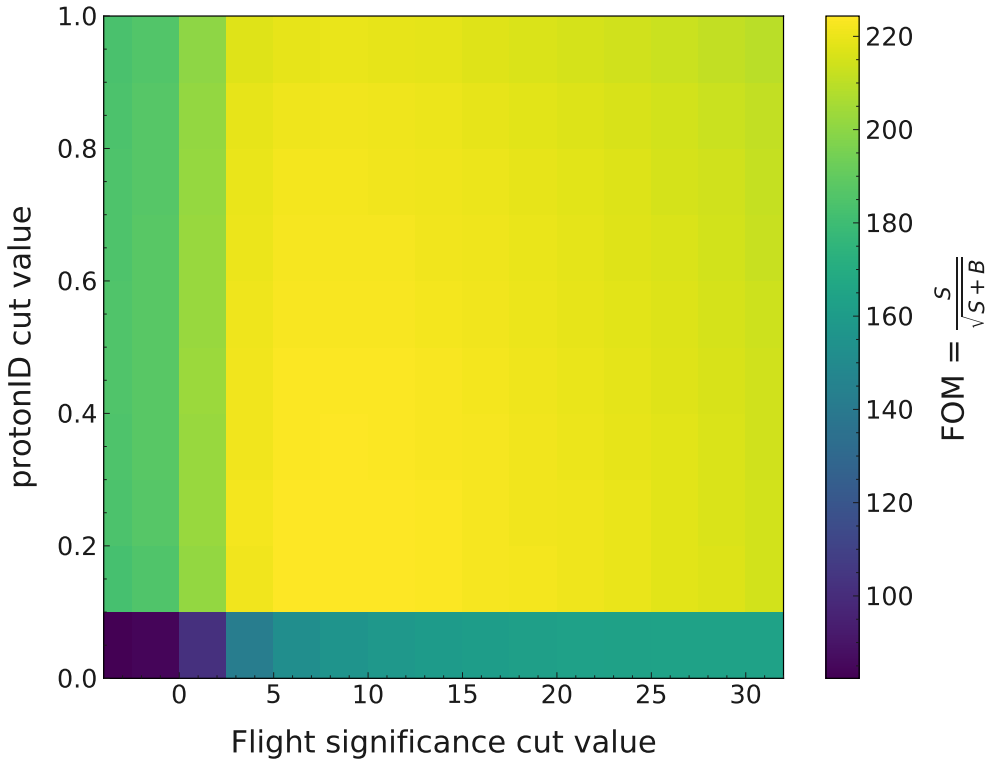

Figure 6.9: Example of 2D FOM computation for Λ candidates with momentum $p_\Lambda \in (1.0, 1.5)$ GeV/c. On the x-axis the lower cut values assigned to the Λ flight significance are shown, while on the y-axis the lower cut values assigned to the protonID are shown. The z-axis represents the computed FOM values. Blue regions have a lower FOM, yellow regions have a higher FOM.

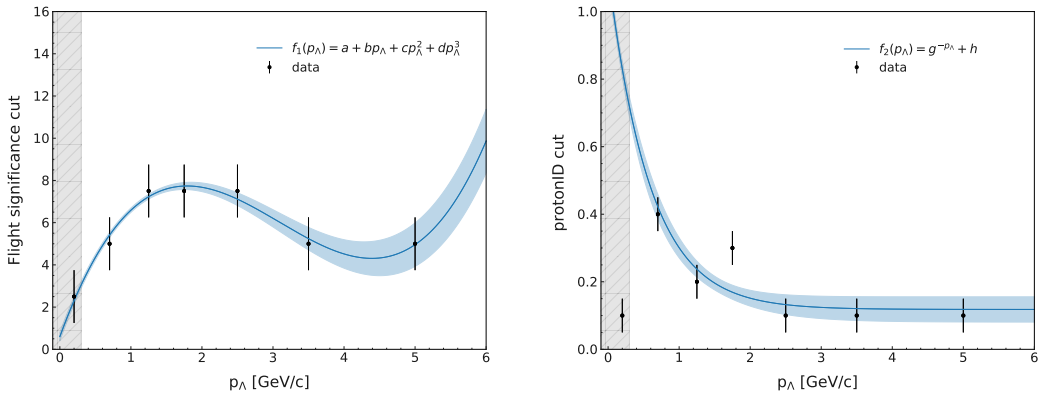

Figure 6.10: Distribution of the the flight significance (left panel) and protonID (right panel) cut values maximizing the FOM as a function of the Λ momentum. The functions used for the fits are purely phenomenological and they are defined in Eqs. (6.4) and (6.5), respectively, and the parameters extracted are summarized in Table 6.1. The errors on the points were taken as the width of the bins in which the flight significance and the protonID were divided, respectively. The gray band in both panels represents the region excluded by the cut on the Λ momentum, $p_\Lambda > 0.4$ GeV/c.

Table 6.1: Parameters extracted from the fits to the cut values of Λ flight significance and protonID as a function of the Λ momentum. The functions used for the fit are defined in Eqs. (6.4) and (6.5).

	f_1 fit parameters				f_2 fit parameters	
par.	a	b	c	d	g	h
value	0.59	9.23	-3.63	0.39	5.48	0.12
error	0.76	0.22	0.15	0.03	2.94	0.05

flight significance:

$$f_1(p_\Lambda) = a + bp_\Lambda + cp_\Lambda^2 + dp_\Lambda^3\,, \tag{6.4}$$

and on an exponential function in the case of the protonID:

$$f_2(p_\Lambda) = g^{-p_\Lambda} + h\,, \tag{6.5}$$

where in both Eqs. (6.4) and (6.5) p_Λ refers to the momentum of the Λ candidate, and a, b, c, d, g, and h are the free fit parameters. The distributions and the corresponding fitting functions are shown in Fig. 6.10. The values of the parameters extracted from the fits are reported in Table 6.1. As it can be noticed from the right panel of Fig. 6.10, the $f_2(p_\Lambda)$ fit function does not look to be ideal for

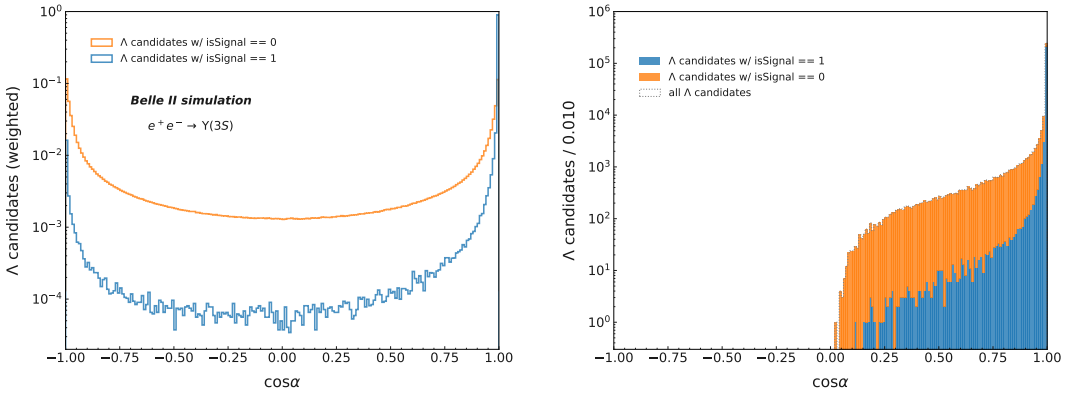

Figure 6.11: Cosine of the angle between the Λ momentum and the vector connecting the IP and the fitted vertex ($cos\alpha$). The panel on the left shows its original distribution, without applying any selection to the sample, both for signal (blue curve) and background (orange curve) candidates. The two distributions are normalized to the total number of signal and background candidates, respectively. The panel on the right shows the $cos\alpha$ distribution after applying the selection described in the text. No candidate with $cos\alpha < 0$ survives after the cut on the flight significance. In both panels the ordinate is represented in logarithmic scale.

low momentum values. A further cut on the Λ momentum was then introduced, $p_\Lambda > 0.4$ GeV/c. Since the fraction of Λ candidates with momentum lower than 0.4 GeV/c is quite small, this additional selection does not have a severe impact on signal reduction. The optimization just described results in the introduction of two momentum-dependent cuts in the Λ selection, that can be written as *flight significance* $> f_1(p_\Lambda)$ and *protonID* $> f_2(p_\Lambda)$.

Finally, in order to further reduce the background contamination, a final requirement is introduced: the cosine of the angle between the Λ momentum and the vector connecting the IP and the fitted vertex ($cos\alpha$) is required to be close to 1 ($cos\alpha > 0.99$). Indeed, for Λ baryons $cos\alpha$ is a rather powerful variables to disentangle between signal and background candidates. The left panel of Fig. 6.11 shows its distribution both for signal (blue curve) and background (orange curve) candidates for the original Λ sample, with no selection applied. These two distributions are normalized to the total number of signal and background candidates, respectively. As one can notice from this plot most of the signal is located in the very backward and forward regions. In the right panel of the same figure, the $cos\alpha$ distribution is shown after applying up to the second set of cuts. At this stage, the negative values of $cos\alpha$ are already excluded by the cut applied on the flight significance (*flight significance* $> f_1(p_\Lambda)$).

The performance of each selection step just described is summarized in Ta-

Table 6.2: Effect of the cuts described in the section both on signal and background candidates. The first row refers to the initial Λ list. The second row refers to the first selection step with track-based cuts. The third row refers to the introduction of the two momentum-based cuts: *flight significance* $> f_1(p_\Lambda)$ and *protonID* $> f_2(p_\Lambda)$. The last row refers to the final set of cuts after introducing a minimum value for the Λ momentum ($p_\Lambda > 0.4$ GeV/c) and the cut on $cos\alpha$ ($cos\alpha > 0.99$).

	# S candidates	fraction S surviving cut	# B candidates	fraction B surviving cut
no cuts	321699	1.0	9124062	1.0
after 1^{st} set of cuts	257990	0.802	5096146	0.559
after 2^{nd} set of cuts	218087	0.678	84016	0.009
after final selection	209489	0.651	33171	0.004

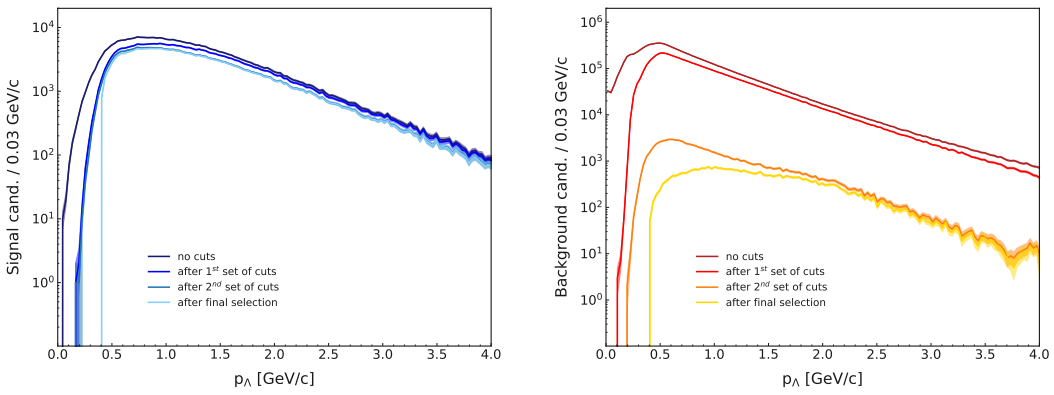

Figure 6.12: Number of Λ candidates as a function of the Λ momentum after each selection step. The panel on the left shows only matched candidates, while the right panel shows only non-matched Λ candidates. In both panels, the ordinate is represented in logarithmic scale.

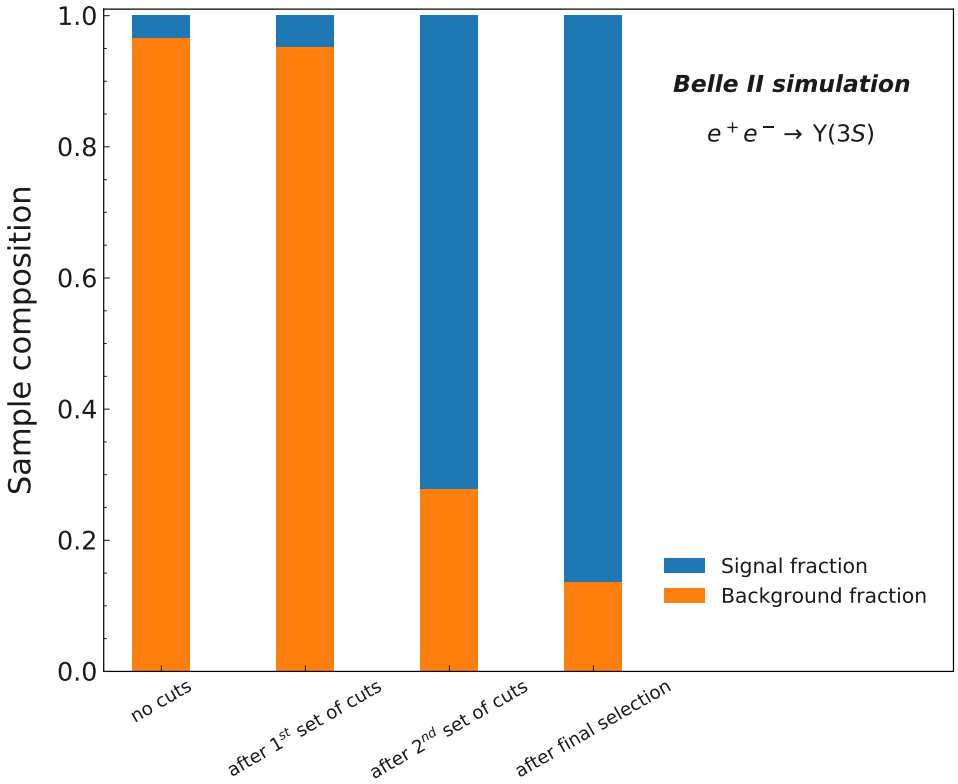

Figure 6.13: Normalized fraction of signal and background candidates of each selection step.

ble 6.2 both for signal and background candidates. The same information is depicted in Fig. 6.12, representing the number of candidates of the original Λ list and after each selection step as a function of the Λ momentum. The performance is shown separately for matched (left panel of Fig. 6.12) and non-matched (right panel of Fig. 6.12) candidates. Figure 6.13 shows, for each of the selection steps, the composition of the Λ sample, in the form of signal and background fractions. A summary of all the selection criteria can be found in Table 6.3.

The net result of the final selection is a very pure Λ sample, containing about the 65% of the matched candidates available in the initial Λ list and only about 0.4% of the non-matched candidates. In this final sample, about 86% of candidates are matched and 14% are non-matched Λ candidates. The fraction of signal and background candidates surviving the final selection is shown in Fig. 6.14, both as a function of the flight distance in the transverse plane (left panel) and as a function of the Λ momentum (right panel). As in the case of Fig. 6.7, the number of surviving candidates is normalized to the number of candidates contained in the initial Λ list. Matched candidates and non-matched candidates are treated

Table 6.3: Final Λ selection criteria. $PDG(tFH, p)$ is the PDG code used for the proton track fit hypothesis and is required to be equal to the proton PDG code [11]. fS indicates the flight Significance of the Λ candidate.

Final selection criteria (I)	
Variable	**Cut**
$nCDCHits, \pi$	> 0
$nCDCHits, p$	> 20
$nSVDHits, p$	< 13
$PDG(tFH, p)$	$== 2212$
p_p/p_Λ	$\in$ [0.6, 1.0]

Final selection criteria (II)	
Variable	**Cut**
fS	$> f_1(p_\Lambda)$
$protonID$	$> f_2(p_\Lambda)$
p_Λ [GeV/c]	> 0.4
$cos\alpha$	> 0.99

separately and shown in blue and orange, respectively.

Figure 6.15 shows the $p\pi$ invariant mass distribution of the Λ candidates once the final selection is applied. Matched (blue histogram) and non-matched (orange histogram) candidates are kept separate, and the two resulting histograms are plotted stacked one on top of the other.

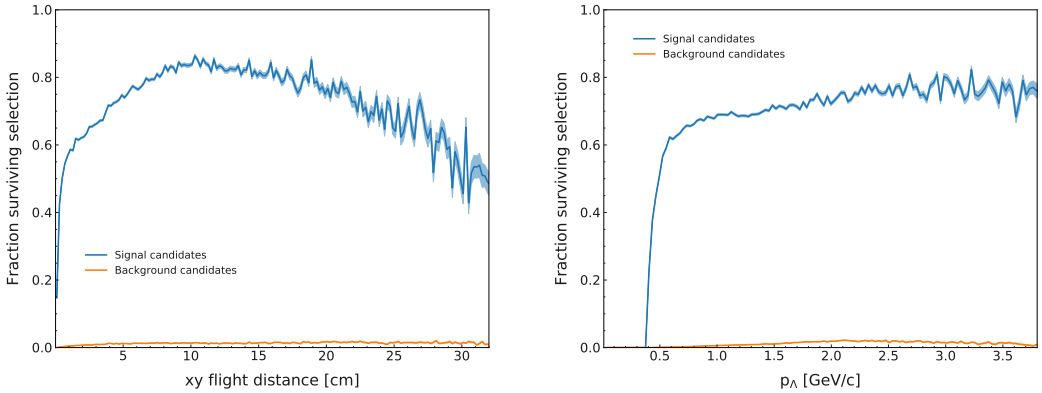

Figure 6.14: Fraction of signal (blue curve) and background (orange curve) candidates surviving the final Λ selection. In the left panel these fractions are represented as a function of the flight distance in the transverse plane, while in the right panel as a function of the Λ candidate momentum. To obtain these fractions, the number of signal (background) candidates surviving the selection was normalized to the number of signal (background) candidates contained in the initial Λ list.

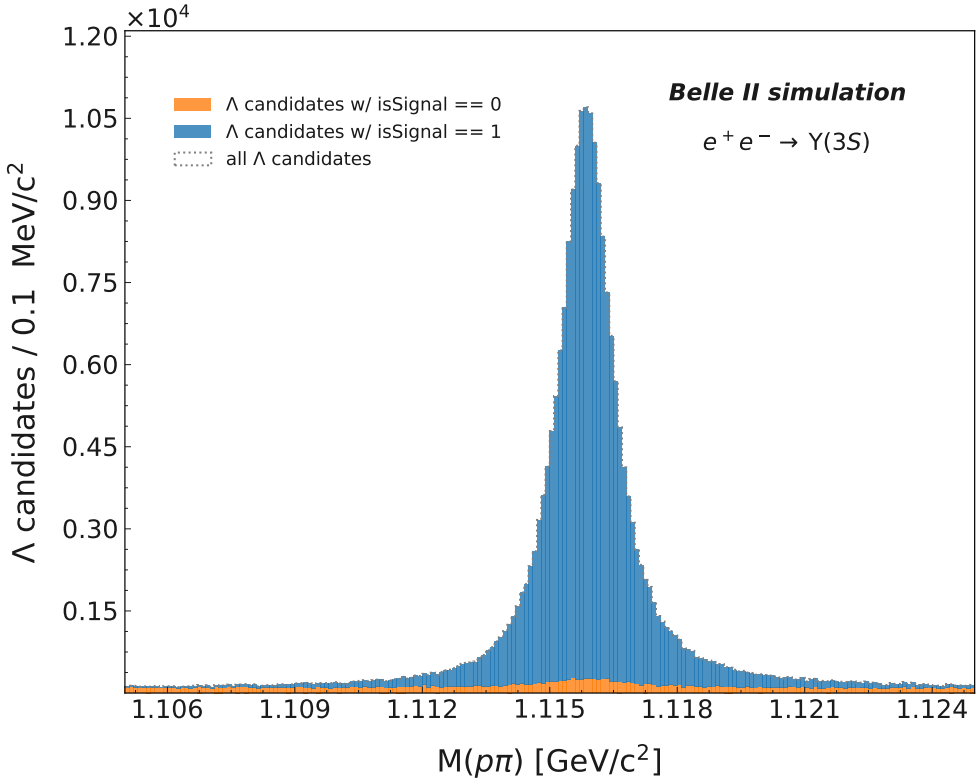

Figure 6.15: Λ invariant mass distribution after the final selection. The selection criteria applied are described in the text. Matched (blue histogram) and non-matched (orange histogram) candidates are kept separate, and the two resulting histograms are plotted stacked one on top of the other. The fraction of background over the total number of candidates in the final sample is in the order of 14%. With regards to the original sample, it has been reduced to the 0.4%.

7

Stable hexaquarks at Belle II

The excellent performance of the Belle II detector and its reconstruction software — described in detail in the previous chapters — underpin the whole physics program of Belle II. This chapter represents the central part of this dissertation, and describes a sensitivity study for the search for a stable, double strange six-quark state produced in $\Upsilon(3S)$ decays at the Belle II experiment. As already discussed in Chapter 3, a previous study in this direction, searching for a double strange stable six-quark state, was published by the BaBar collaboration a few years ago [112]. The main difference between this work and the BaBar analysis is represented by the investigation of various decay channels, accounting for the possible production of pairs of charged pions in the final state (with a maximum of four pairs). In this context, such pion pairs — originating directly from the $\Upsilon(3S)$ — will be referred to as primary pions to distinguish them from the secondary ones originating from Λ decays. Furthermore, even for the channel already investigated by the BaBar collaboration, an increase of the collected luminosity would make it possible to improve the existing upper limits (ULs). In Section 7.3, where the UL extraction is discussed, the BaBar result is compared with the Belle II prediction.

In the sensitivity study presented here, a total of five decay channels is considered:

$$\Upsilon(3S) \rightarrow S\,\Lambda\,\Lambda\,n\pi_s \quad (\text{with } n = 0,\ 2,\ 4,\ 6,\ \text{and } 8)\,, \tag{7.1}$$

where S, following the naming convention introduced by Farrar [36], refers to the stable hexaquark, and $n\pi_s$ indicates the number of primary charged pions present in the final state. The full mass range compatible with a stable state, $0 < M_S < 2.055$ GeV/c^2, was considered. The study presented here is performed using a MC sample equivalent to a luminosity $\mathcal{L} = 300\ fb^{-1}$. The chapter is divided into three main parts: a description of the MC samples used (Section 7.1), a description of the event selection applied and its optimization (Section 7.2), and a description of the UL extraction for the different channels (Section 7.3). This part of the work is also described in an internal Belle II note, written by the author of the thesis herself [149].

7.1 Monte Carlo samples

Generally speaking, when talking about the MC samples used for an analysis, it is important to distinguish between *signal* MC, mimicking the signature of the searched channel(s), and *background* MC, mimicking all other possible event types stemming from the considered reaction at the given energy.

In this analysis, background events are represented by all the generic decays of the $\Upsilon(3S)$ and by continuum events ($e^+e^- \to q\,\bar{q}$) at the same $\sqrt{s}$; as for the employed background MC, Belle II centrally produced generic and continuum MC samples at the $\Upsilon(3S)$ resonance equivalent to a luminosity of 300 fb^{-1} were used with early phase 3 geometry and early data taking background conditions (eph3 BG×1) — the same as introduced in Section 5.5. Details about the used MC campaign are given in Appendix D (Section D.1). The MC signal samples were produced locally instead. In order to simulate the hexaquark S, a new neutral particle with width and spin equal to zero was added to the event generator EvtGen [139]. Due to its zero-width, the hexaquark is assumed to be stable by Geant4 [150], the detector simulation package, and therefore it is ignored in the signal simulation. For each signal channel, the $\Upsilon(3S)$ was forced to decay following a generic m-body phase space model, with m depending on the number of pions in the final state. The resulting signature is a bump in the distribution of the mass squared recoiling against the two Λ baryons and the n pions, peaking around the square of the value of the hexaquark mass M_S^2.

With the hexaquark mass obviously unknown, multiple samples — each with a different value assigned to the hexaquark mass — were generated. An initial study was performed in order to establish exactly how many and which mass values were to be generated. At this stage only the final state without pri-

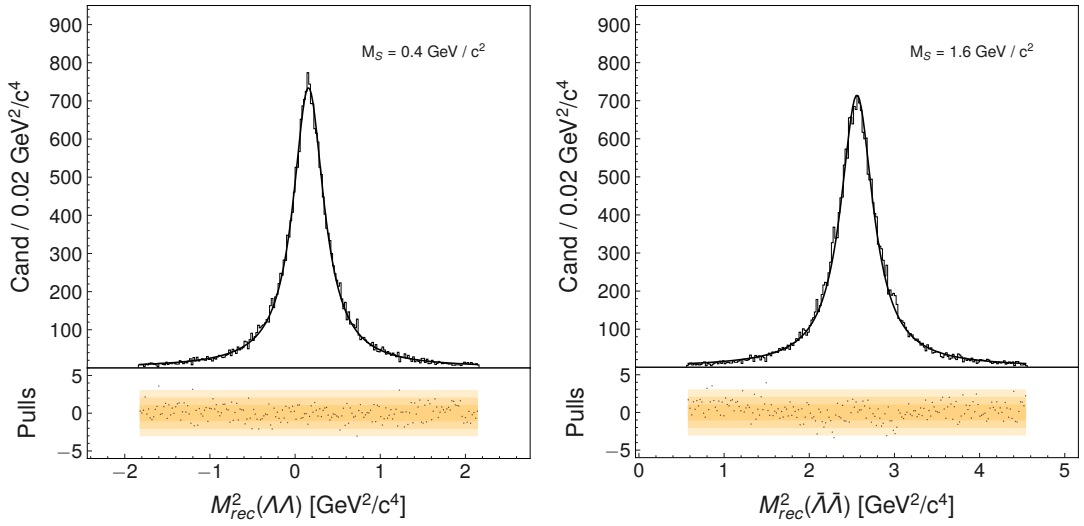

Figure 7.1: Distribution of the invariant mass squared of the system recoiling against the two (anti)baryons for two of the preliminary MC samples. The left panel shows the channel $\Upsilon(3S) \to S\Lambda\Lambda$, with generated hexaquark mass $M_S = 0.4$ GeV/c^2. The right panel shows the channel $\Upsilon(3S) \to S\bar{\Lambda}\bar{\Lambda}$, with generated hexaquark mass $M_S = 1.6$ GeV/c^2. The pulls shown in the bottom part of both panels are defined as the difference between the experimental points and the fit function divided by the error. The orange bands represent the ± 1, 2, and 3σ region from less to more faded, respectively.

mary pions was considered, and the simulation was performed without including beam background. For the generation itself, the final states with two Λ and two $\bar{\Lambda}$ baryons were kept separate, and the hexaquark mass values were arbitrarily chosen. Specifically, 50×10^3 events for 21 different mass values, ranging from $M_S = 0.2$ GeV/c^2 to $M_S = 2.2$ GeV/c^2, in steps of 100 MeV/c^2 were generated for the $\Upsilon(3S) \to S\Lambda\Lambda$ channel, together with 50×10^3 events for three different mass values for the $\Upsilon(3S) \to S\bar{\Lambda}\bar{\Lambda}$ channel ($M_S = 0.4$, 1.6, and 2.055 GeV/c^2). For each of these samples, the recoil mass squared was plotted and the obtained distributions fitted using a Breit-Wigner function, defined as following:

$$BW(x) = N \frac{1}{(x-\mu)^2 + \frac{1}{4}\omega^2} \,. \tag{7.2}$$

The three free parameters N, μ, and ω are related to the height, the mean, and the width of the peak, respectively. For a Breit-Wigner distribution, ω is equivalent to the Full Width Half Maximum (FWHM). Figure 7.1 shows the square of the recoil mass distribution for two of the samples. The parameters obtained from all the fits are reported in Appendix D (Section D.2). As a test,

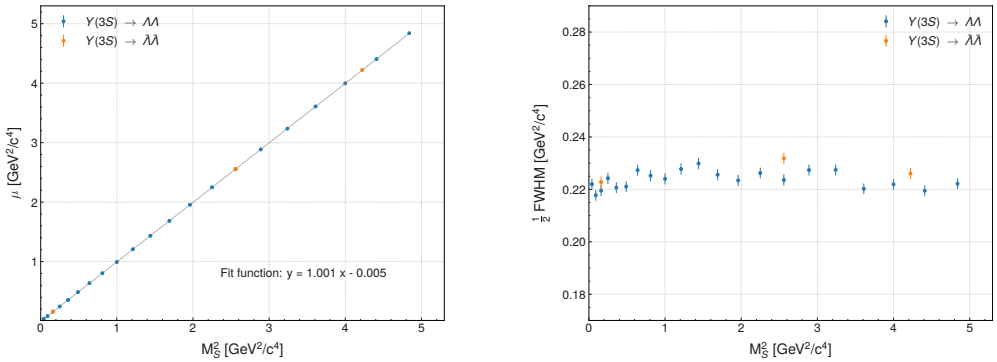

Figure 7.2: Distribution of the fit parameters μ (left panel) and $\frac{1}{2}$ FWHM (right panel) as a function of the generated hexaquark mass squared. In the left panel, the obtained distribution was fitted with a first order polynomial, and the obtained fit function, as well as the parameters, are reported on the plot itself.

the values of μ obtained from the fit were plotted as a function of the square of the generated hexaquark mass M_S^2, and the obtained points were fitted with a first order polynomial, as shown in the left panel of Fig. 7.2. In this plot the fit function and its parameters are reported on the figure itself. The right panel of Fig. 7.2 shows the distribution of the fit parameter $\frac{1}{2}$ FWHM as a function of the square of the generated hexaquark mass M_S^2, instead.

The minimum value among the fit parameters $\frac{1}{2}$ FWHM was chosen to be the *pitch*, in the recoil mass squared space, between each consecutive value of the hexaquark masses $M_{S,i}$ to be generated in the final sample:

$$pitch = \min\left(1/2 \text{ FWHM}\right) = 0.218 \text{ GeV}^2/\text{c}^4 \,. \tag{7.3}$$

In other words, starting from the maximum value considered $M_{S,max} = 2.055$ GeV/c^2, and proceeding until the mass value become negative, each preceding value $M_{S,i-1}$ in the list of considered values was defined using the following equations:

$$M_{S,i-1} = \sqrt{M_{S,i}^2 - pitch} \,. \tag{7.4}$$

Using such a definition, 20 different hexaquark mass values were established to be generated for the subsequent part of the study:

$$\begin{aligned} M_S = \{&0.285, 0.547, 0.719, 0.857, 0.976, 1.082, 1.179, \\ &1.268, 1.351, 1.429, 1.504, 1.574, 1.642, 1.707, \\ &1.770, 1.831, 1.889, 1.946, 2.001, 2.055\} \text{ GeV/c}^2 \,. \end{aligned} \tag{7.5}$$

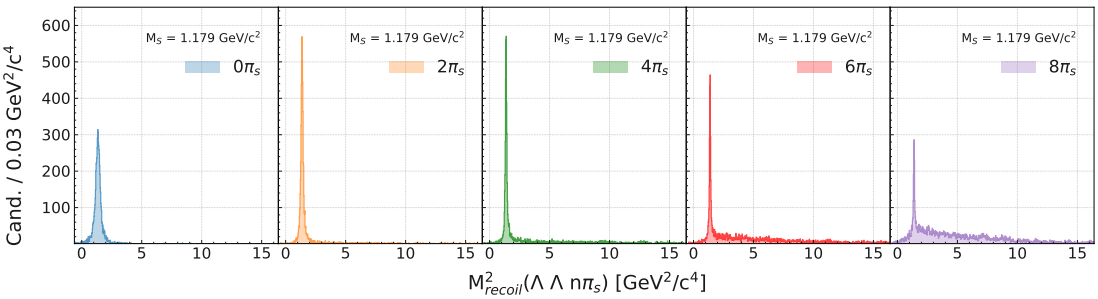

Figure 7.3: Distribution of the invariant mass squared of the system recoiling against the two Λ candidates and the primary pions $n\pi_s$. Moving from the leftmost to the rightmost panel, n = 0, 2 ,4, 6, and 8, respectively. In this example, the generated hexaquark mass is $M_S = 1.179$ GeV/c^2.

For each of the 20 mass values, the five different channels introduced in Eq. (7.1) were considered. The difference between each channel lies — as already mentioned — in the number of primary pion pairs in the final state. Each channel was generated keeping the final states with two Λ and two $\bar{\Lambda}$ baryons separate, thus doubling the number of generated channels. For each of the $20 \times 5 \times 2$ MC signal samples, 75×10^3 events were generated, and early data taking beam background was used during the simulation, reproducing the same conditions of the MC background sample.

As expected, the introduction of beam background in the simulation and of pion pairs in the final state give rise to a more complex scenario. When increasing the number of tracks in the final state, the number of combinatorial possibilities increases as well, often leading to the presence of multiple hexaquark candidates in a single event. Figure 7.3 shows an example of the distribution of the mass squared recoiling against the two Λ baryons and $n\pi_s$ for the five different channels. In this specific example, $M_S = 1.179$ GeV/c^2 and two Λ baryons were considered in the final state. In all the panels it is possible to observe the presence of a tail to larger mass values. The contribution of such a tail becomes more and more important with the increment of primary pion pairs in the final state (i.e. it is minimum in the leftmost panel and maximum in the rightmost panel of the figure). The multiple-candidates problem will be addressed in the next section, after applying a first set of basic selection cuts to the samples.

A fundamental information in any analysis — in order to determine the reconstruction efficiency of each single channel — is the number of correctly reconstructed events. In this analysis, a correctly reconstructed event (*signal*) is required to fulfill all the following requirements:

- for each Λ, the PDG code of its mother must be equal to that of the $\Upsilon(3S)$;

- both Λ baryons should be correctly reconstructed (*isSignal == 1*);
- for each Λ, the PDG code of its first sister must be the same as that of the hexaquark;
- the PDG code of the first $\Upsilon(3S)$'s daughter must be the same as that of the hexaquark;
- for each π in the final state, its mother's PDG code must be equal to that of the $\Upsilon(3S)$.

The PDG code of the hexaquark is a unique value, different from the existing entries in the MC particle numbering scheme [11], that was arbitrarily chosen at the generation time and kept constant throughout the whole analysis. Wrongly reconstructed signal events will be also referred to as *!signal* throughout the chapter.

7.2 Event selection

The event selection is a key step in any analysis: a series of cuts is introduced in order to discard unwanted events while keeping the investigated channel only.

7.2.1 Track-based cuts

The selection of good Λ candidates — one of the most important steps for the analysis — was largely described in the previous chapter (Section 6.3). Additionally, some track-based requirements were introduced for each primary pion, for those channels involving them:

- pionID,π > kaonID,π ;
- nSVDHits,π > 0 ;
- nCDCHits,π > 0 .

The first condition is a loose requirement on the PID of each candidate, asking that its probability of being a pion is larger than that of being a kaon. As for the second condition, since the primary pions originate directly from the $\Upsilon(3S)$, and thus close to the IP, the presence of at least one hit in the SVD is a reasonable assumption. Finally, SVD-only tracks (*i.e.* tracks with no associated CDC hits)

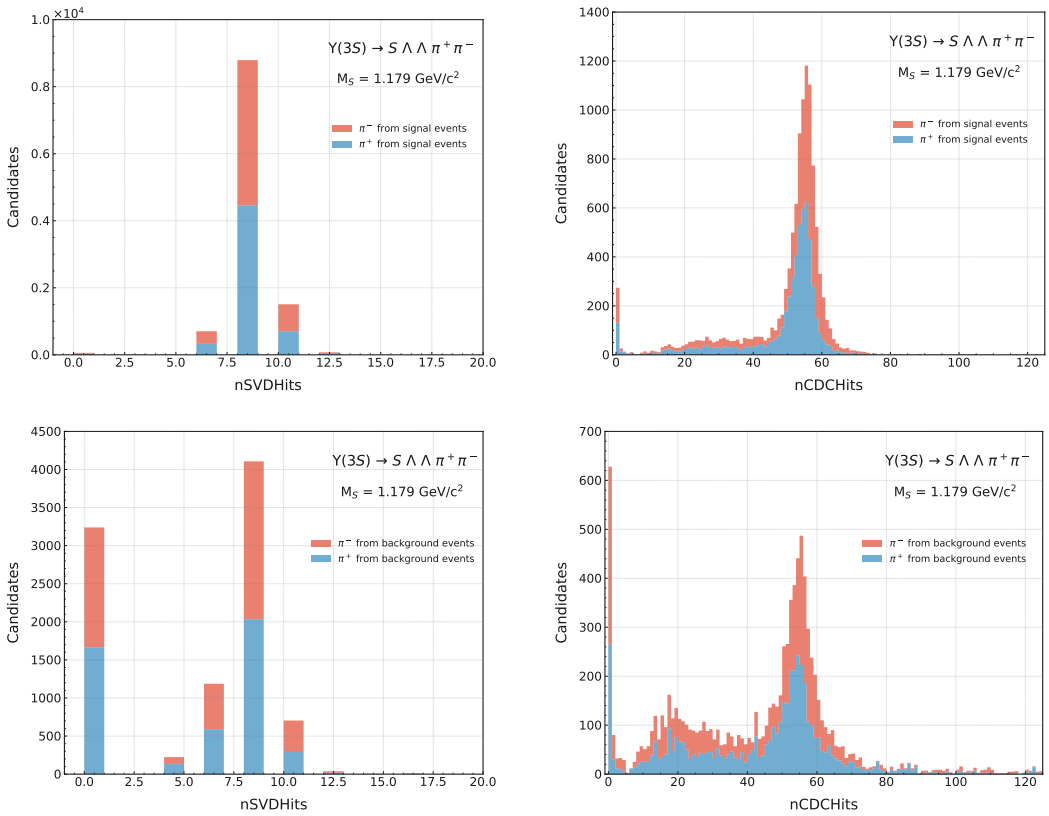

Figure 7.4: Distribution of the number of SVD (left column) and CDC (right column) hits for correctly (top row) and wrongly reconstructed events (bottom row). In each panel, the color blue and red have been used for positive (π^+) and negative (π^-) charged pions, respectively.

are excluded because of a higher fake-rate fraction with respect to SVD+CDC tracks [1].

Figure 7.4 illustrates the effect of the described track-based requirements for one specific signal channel: two primary pions in the final state for a generated hexaquark mass $M_S = 1.179$ GeV/c^2. The distribution of the number of SVD (left column) and CDC (right column) hits for the two primary pions is shown, both in the case of correctly (top row) and wrongly (bottom row) reconstructed signal events. The contributions of positive (blue) and negative (red) charged pions are plotted as stacked histograms. From these panels it is apparent that the fraction of wrongly reconstructed signal events with no SVD nor CDC hits is larger than that of correctly reconstructed ones. The relative results on the very same signal sample are summarized in Table 7.1, reporting both the number of correctly and wrongly reconstructed events, before and after applying the selection. Additional

[1] This statement is based on the result of MC-based performance studies that compare the full tracking chain with a SVD-only tracking chain, done with *release-04*.

Table 7.1: Number of events before and after the track-based selection applied to the final state pions, both for correctly (*signal*) and wrongly (*!signal*) reconstructed events. The results were obtained for the sample as in Fig. 7.4, $M_S = 1.179$ GeV/c^2. More detailed tables can be found in Section D.3.

	n events	nSVDHits >0	nCDCHits >0	both	% left
signal	5572	5516	5301	5251	94.24
!signal	4759	1982	4163	1551	32.59

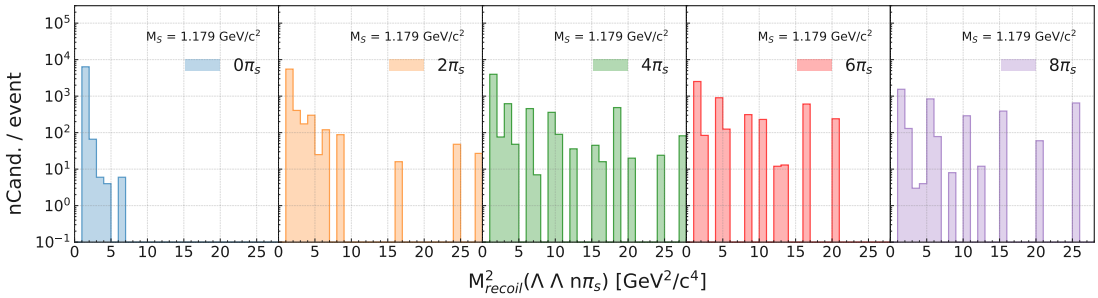

Figure 7.5: Distribution of the number of hexaquark candidates per event for a given hexaquark mass value. Moving from left to right, the number of pions in the final state increases. In this example, the generated hexaquark mass is $M_S = 1.179$ GeV/c^2. Note the logarithmic scale of the y-axis.

tables, summarizing the results for all generated hexaquark masses, can be found in Section D.3 (Tables D.4 and D.5).

7.2.2 Best Candidate selection

It is important to stress that, in Belle II, analyses performed within the standard configuration are candidate-based. This results for many analyses, in particular in searches for rare events, in the necessity of implementing some sort of Best Candidate (BC) selection in case multiple signal candidates per event are found. Figure 7.5 shows the number of candidates per event, after applying the selections on Λ and primary pions described in Section 6.3 and Section 7.2.1, respectively. As it might be expected, the number of candidates per event is higher for the channels with primary pion pairs in the final state, but nevertheless events with multiple candidates are present also in the channel with only Λ baryons in the final state. In order to guarantee the presence of one single hexaquark candidate S per event, a BC selection was implemented. Different variables were considered and tested as possible BC variable. Based on the overall efficiency of the selection,

the final choice fell on *best* Λ_s, namely the *best Lambda pair*, defined as:

$$\begin{aligned} best\Lambda_s &= min\{ \sum_{i=1,2} \Delta\Lambda_i \}, \\ \Delta\Lambda_i &= |M_{i,\Lambda} - M_{PDG,\Lambda}|. \end{aligned} \tag{7.6}$$

In this equation, $i = 1, 2$ indicates the two Λ candidates of the event; $M_{i,\Lambda}$ refers to the reconstructed mass value, while $M_{PDG,\Lambda}$ refers to the Λ mass value reported by the PDG [11], $M_{PDG,\Lambda} = 1115.683$ MeV/c^2. The BC efficiency is defined as the ratio between the number of signal events surviving the BC selection and the number of events with (at least) one correctly reconstructed hexaquark before the BC selection:

$$\epsilon_{BC} = \frac{\#\text{ correctly reconstructed signal events after BC}}{\#\text{ events w/} \geq 1 \text{ correctly reconstructed hexaquark before BC}}. \tag{7.7}$$

As shown in Fig. 7.6, the efficiency of this selection is very high. It depends on the number of primary pion pairs in the final state, but it is nevertheless always higher than 93%.

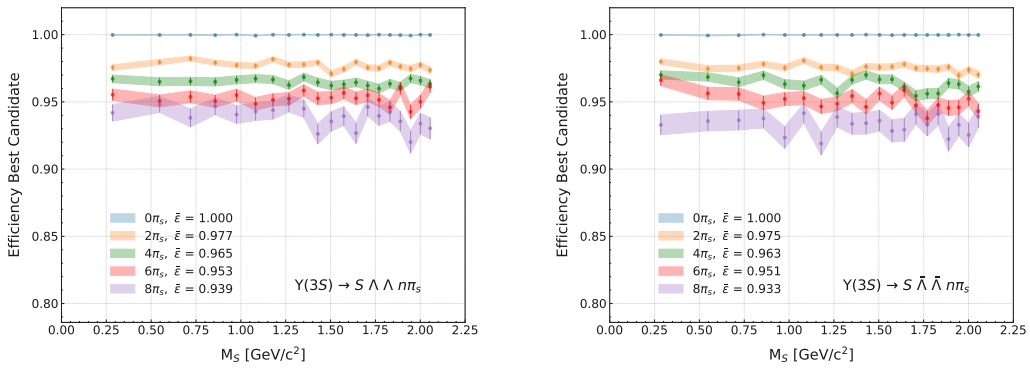

Figure 7.6: Efficiency of the BC selection as a function of the generated hexaquark mass. The definition of BC efficiency is given in Eq. (7.7). In the left panel, the channels with two Λ baryons in the final state are shown, while in the right panel those with two $\bar{\Lambda}$ baryons are shown. On the bottom left of the canvas, the average BC efficiency value $\bar{\epsilon}$ for each channel is reported as well. The average BC efficiency is higher than 93% for all channels.

7.2.3 Rest Of Event

After optimizing and applying the selection on particles directly involved in the decay channels, one possibility to further reduce the background is to introduce a selection on the Rest Of Event (ROE), namely everything not directly involved

in the signal decay chain. In an ideal world, a signal event should contain no additional charged nor neutral particles other than those coming from the signal channel itself. Evidently, in reality things are more complicated than that, and it is likely for a signal event to be contaminated by additional tracks and/or neutral clusters, whose origin is due to beam background. In this analysis, this problem was addressed by studying the distribution of two ROE variables, *nROE_Charged* (*i.e.* the number of charged tracks in the ROE) and *nROE_Photons* (*i.e.* the number of photons in the ROE), both for signal and background events. Notice that, from this section on, the channels with either two Λ or two $\bar{\Lambda}$ candidates are treated simultaneously as one single channel. A cut on both ROE variables was optimized using the Punzi FOM [151]. The Punzi FOM is defined as:

$$Punzi\,FOM = \frac{\epsilon(S)}{\frac{a}{2} + \sqrt{B}}, \tag{7.8}$$

where $\epsilon(S)$ represents the signal efficiency, B represents the number of background events and a represents the number of σ corresponding to a one-sided Gaussian test at significance level α. In this context it was assigned to be $a = 5$, corresponding to the accepted threshold for a new particle discovery. For each mass value, both $\epsilon(S)$ and B were evaluated in a symmetric window around the recoil mass squared, $[M^2_{recoil} - \frac{1}{2}\text{FWHM},\, M^2_{recoil} + \frac{1}{2}\text{FWHM}]$. Such a window was chosen to be different for each generated hexaquark mass, and in particular the value of $\frac{1}{2}$FWHM was extracted from a fit to the signal channel. After applying the selection described in the previous sections on Λ candidates and primary pions, and similarly to what is described in Section 7.1, the distribution of the recoil mass squared was fitted for each hexaquark mass value using a Breit-Wigner function, previously defined in Eq. (7.2). Figure 7.7 shows the values of μ and $\frac{1}{2}$FWHM extracted from each fit as a function of the generated hexaquark mass squared. In particular, the right panel shows that the values of $\frac{1}{2}$FWHM obtained from the fit are different for each channel, and moreover they get smaller when increasing the number of primary pion pairs in the final state. This suggests that, when performing the scan for the UL extractions, a larger number of hexaquark masses should be considered than the original 20 values listed in Eq. (7.5). This concern will be addressed in the next section. Furthermore, these distributions can be fitted using a second order polynomial, thus converting the discrete values of $\frac{1}{2}$FWHM into a continuous function of M^2_S. The parameters obtained from the fits to the five considered signal channels are reported on the plot itself.

Once the definition of the FOM to be used for the optimization is established

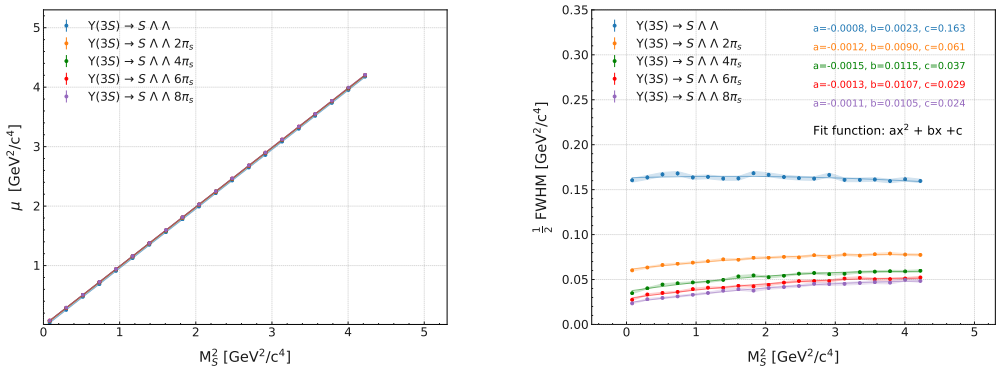

Figure 7.7: Distribution of the fit parameters μ (left panel) and $\frac{1}{2}$FWHM (right panel) obtained by fitting the square of the recoil mass distribution of the hexaquark candidates with a Breith-Wigner as a function of the generated hexaquark mass squared. As a sanity check, the points in the left panel were fitted with a first order polynomial, and the fit functions are represented as solid lines. In the right panel, the points were fitted with a second order polynomial. The obtained functions are represented as solid lines, and the fit parameters are reported in the top right corner of the panel.

(Eq. (7.8)), let us go back to the ROE variables themselves. These variables were treated with a common general strategy (any small differences will be introduced at a later stage): the cut value was left free to vary from channel to channel — allowing different cut values for channels with different number of primary pion pairs — but it was required to be constant for all the generated hexaquark mass values of a specific signal channel. In particular, for each channel it was decided to chose the cut value maximizing the largest number of masses.

Concerning the number of tracks in the ROE, *nROE_Charged*, not all the remaining tracks in the event were included in such a list but only those surviving some basic selections on the transverse (dr) and z distance (dz) of the POCA with respect to the IP. A selection on these variables around zero is a way to exclude tracks originating from beam background, that do not come from the IP but from further away. Specifically it was required $|dr| < 2$ cm and $|dz| < 5$ cm, where the chosen cut values are quite standard for Belle II analyses. The five panels of Fig. 7.8 show the Punzi FOM trend as a function of the exclusive cut imposed on the number of tracks in the ROE, one for each signal channels. In each of them, the Punzi FOM trend is shown for all the generated hexaquark masses. Four different cut values were tried: $nROE\_Charged < x$, with $x = 0$, 1, 2, 3. In the plots the x-axis reports the values to which the exclusive cut was applied, namely $nROE\_Charged < x$ for every x value. The first cut value,

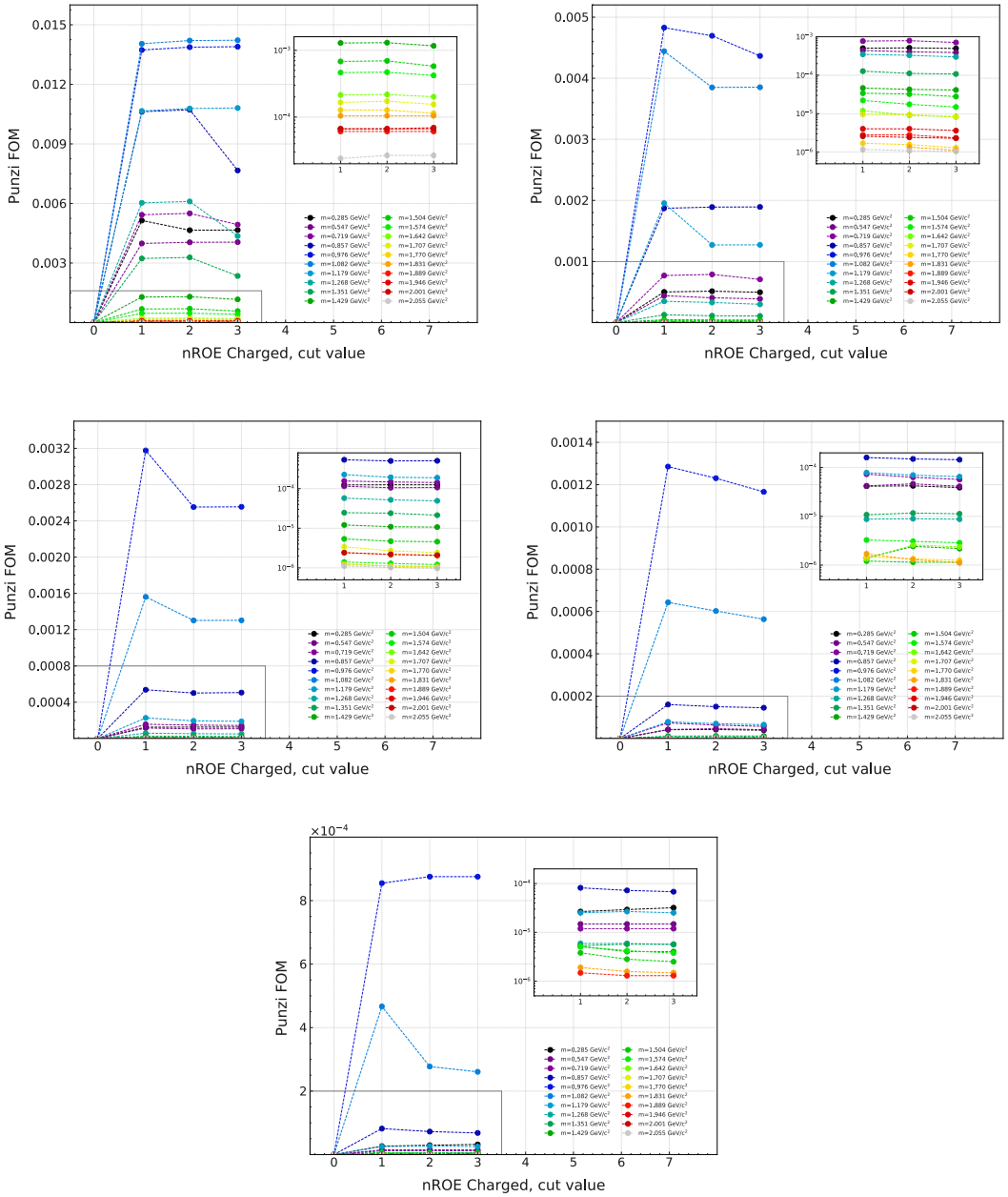

Figure 7.8: Punzi FOM trend as a function of the cut imposed on the number of tracks in the ROE for the five different channels $\Upsilon \to S\Lambda\Lambda n\pi_s$. From left to right and from top to bottom $n = 0$, 2, 4, 6, and 8 can be observed, respectively. In each plot, the trend for each mass value is shown. The x-axis reports the values to which an exclusive cut was applied, namely $nROE\_Charged < x$ for every x value. The boxes in the upper right corner of each canvas represent a zoom in the region within the grey square (lower left corner).

$x = 0$, represents just a cross check: as expected, requiring $nROE\_Charged < 0$ returns 0 events both for signal and background, and the Punzi FOM in that case is always 0. Based on the results obtained, the following selections were applied:

- $nROE\_Charged < 2$ for $\Upsilon(3S) \to S\,\Lambda\,\Lambda$;
- $nROE\_Charged < 1$ for $\Upsilon(3S) \to S\,\Lambda\,\Lambda\,2\pi_s$;
- $nROE\_Charged < 1$ for $\Upsilon(3S) \to S\,\Lambda\,\Lambda\,4\pi_s$;
- $nROE\_Charged < 1$ for $\Upsilon(3S) \to S\,\Lambda\,\Lambda\,6\pi_s$;
- $nROE\_Charged < 1$ for $\Upsilon(3S) \to S\,\Lambda\,\Lambda\,8\pi_s$.

In other words, in the channel with no primary pion pairs up to one track is allowed to be found in the ROE. For all the other channels, instead, the requirement is to find no tracks in the ROE.

Concerning the number of photons in the ROE, *nROE_Photons*, a slightly more advanced approach was needed. The definition of a "standard" selection for photons, always in the context of Belle II analyses, is a bit more tricky and less general than for tracks. Therefore, in order to decide which photons to be included in the ROE variable construction, different configurations were tested. Each of the considered configurations was built starting from two photon-related variables: E, the energy of the particle, and *clusterZernikeMVA* (in this context referred to as Z), a multivariate shower-shape classifier that uses multiple Zernike moments [152]. Specifically, the *clusterZernikeMVA* variable returns a value between 0 and 1, the output of a MVA built using eleven Zernike moments of an ECL cluster. In total, 24 different configurations were built, obtained by combining 6×4 different selections on the two mentioned photon-related variables:

- $E \geq E_{cut}$, with $E_{cut} = [0.05, 0.1, 0.15, 0.2, 0.25, 0.3]$ GeV ;
- $Z \geq Z_{cut}$, with $Z_{cut} = [0.0, 0.2, 0.5, 0.8]$.

As a convention, each configuration is labeled with the suffix "*_EXZY*" in the text, where X and Y are replaced by an integer index corresponding to a specific E and Z cut, respectively. The list of cuts with their corresponding X or Y indices can be found in Table 7.2.

For this variable, the final configuration to be used and its cut value were left free to vary from channel to channel, but they were required to remain the same for all the generated hexaquark masses of a specific channel. For each configuration, four possible cuts on the number of ROE photons were tested:

Table 7.2: Explanation of the convention used for the different *nROE_Photons* configurations. Each configuration is labeled with the suffix *_EXZY*, and the cut corresponding to each X and Y value is reported here.

EX	E_{cut} [GeV]	0.05	0.10	0.15	0.20	0.25	0.30
	X	0	1	2	3	4	5

ZY	Z_{cut}	0.0	0.2	0.5	0.8
	Y	0	1	2	3

nROE_Photons_EXZY $< x$, with $x = 0, 1, 2, 3$. As before, the first cut value ($x = 0$) represents only a cross check. Because of the high number of combinations (20 masses $\times$ 24 configurations $\times$ 4 cut values), for this variable it was decided to keep the cut value equal to 1 (i.e. not allowing the presence of any photon in the ROE), and, under such a condition, to pick the best configuration.

Figures 7.9 to 7.13 show the Punzi curve trend as a function of the exclusive cut imposed on the number of photons in the ROE, for each of the 24 considered configurations. In each panel, the Punzi FOM trend is shown for all the generated hexaquark masses. Also in this case in the plots the x-axis reports the values to which the exclusive cut was applied, namely *nROE_Photons_EXZY* $< x$ for every x value. For each channel it was decided to chose configuration that, when considering the cut value equal to 1 (*nROE_Photons_EXZY* < 1), maximized the Punzi FOM for the largest number of masses. Based on the results obtained, the following selections were applied:

- $nROE\_Photons\_E5Z3 < 1$ for $\Upsilon(3S) \to S\,\Lambda\,\Lambda$;
- $nROE\_Photons\_E2Z3 < 1$ for $\Upsilon(3S) \to S\,\Lambda\,\Lambda\,2\pi_s$;
- $nROE\_Photons\_E3Z1 < 1$ for $\Upsilon(3S) \to S\,\Lambda\,\Lambda\,4\pi_s$;
- $nROE\_Photons\_E3Z1 < 1$ for $\Upsilon(3S) \to S\,\Lambda\,\Lambda\,6\pi_s$;
- $nROE\_Photons\_E4Z2 < 1$ for $\Upsilon(3S) \to S\,\Lambda\,\Lambda\,8\pi_s$.

7.3 Upper limit extraction

After applying the event selection described in the previous sections both on signal and background samples, it is possible to estimate the expected UL on the different channels.

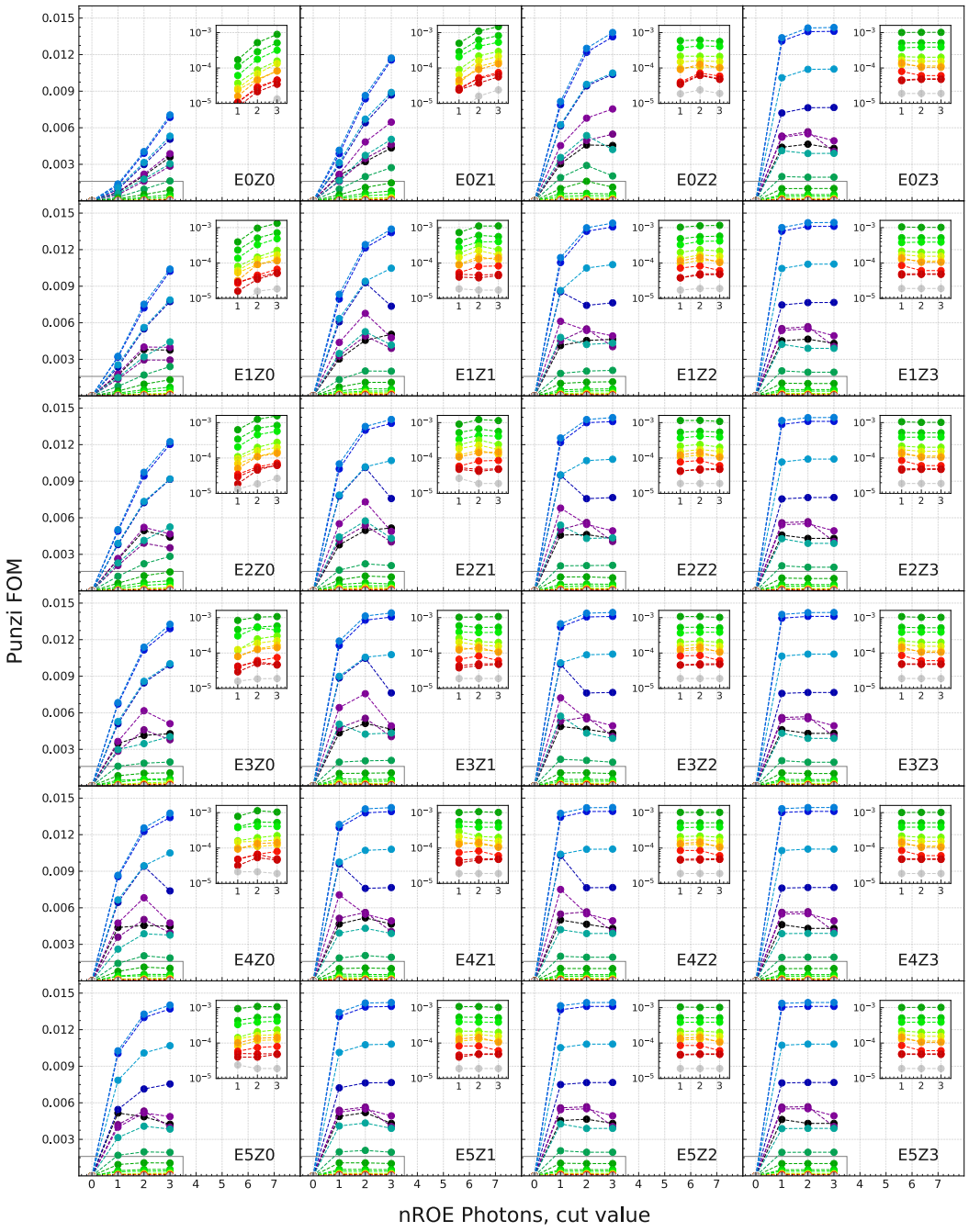

Figure 7.9: Punzi FOM trend as a function of the cut imposed on the number of ROE photons for the channel $\Upsilon(3S) \to S\Lambda\Lambda$. Each of the 24 canvases represents a specific configuration, and shows all generated mass values. The x-axes report the values to which the exclusive cut was applied, namely $nROE\_Photons\_EXZY < x$ for every x value. The boxes in the upper right corner of each plot represent a zoom in the region within the grey square (lower left corner).

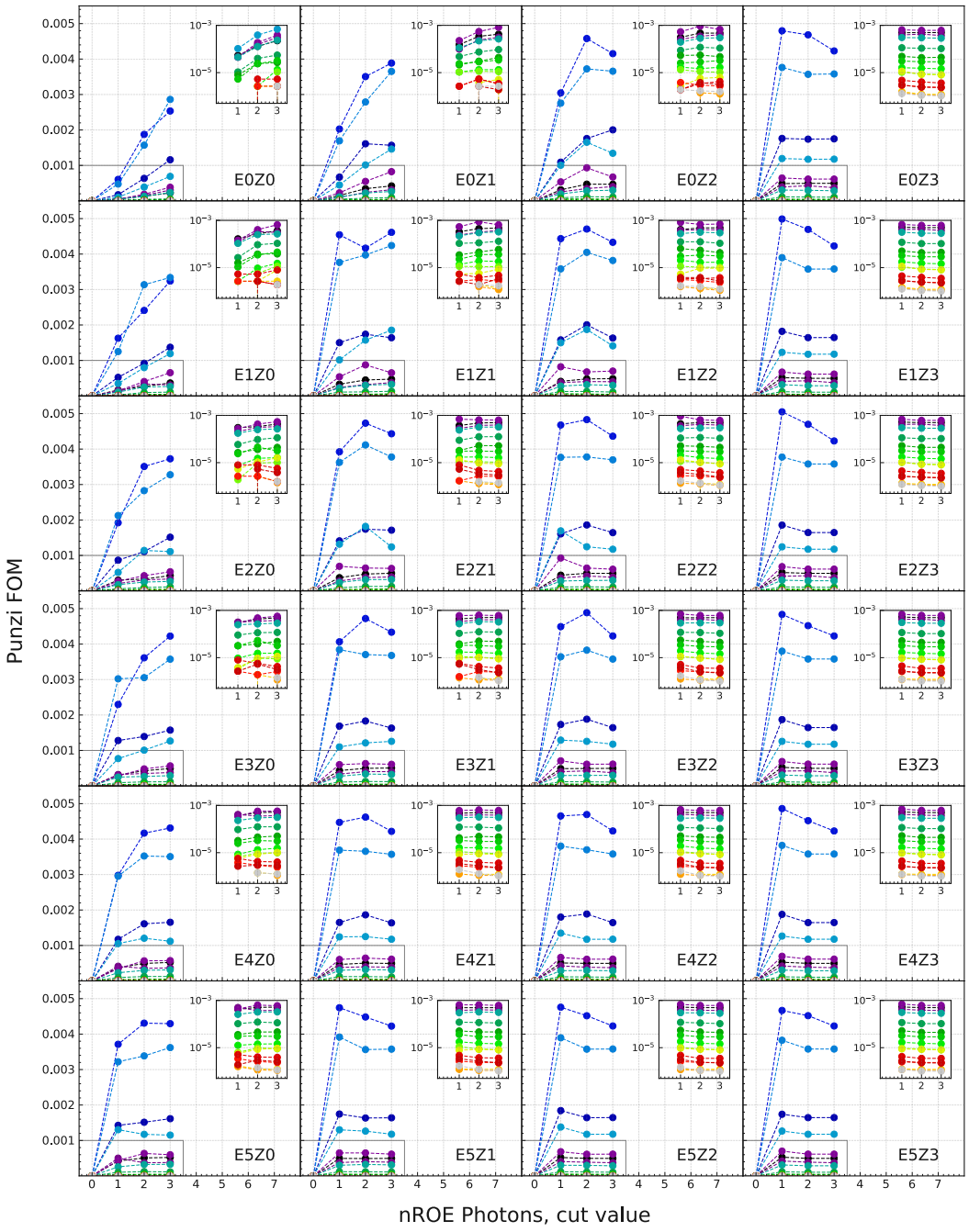

Figure 7.10: Punzi FOM trend as a function of the cut imposed on the number of ROE photons for the channel $\Upsilon(3S) \to S\Lambda\Lambda\, 2\pi_s$. Each of the 24 canvases represents a specific configuration, and shows all generated mass values. The x-axes report the values to which the exclusive cut was applied, namely $nROE\_Photons\_EXZY < x$ for every x value. The boxes in the upper right corner of each plot represent a zoom in the region within the grey square (lower left corner).

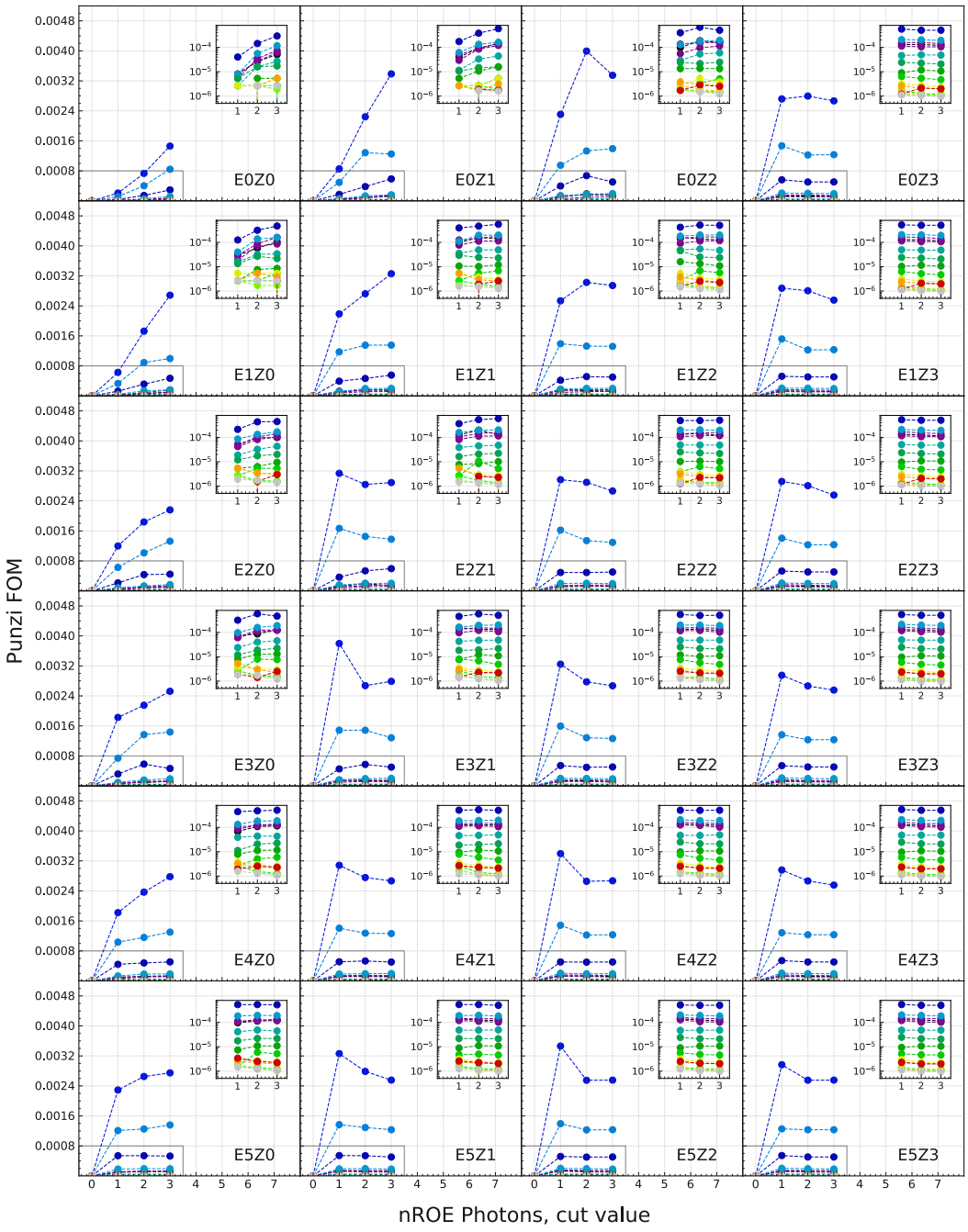

Figure 7.11: Punzi FOM trend as a function of the cut imposed on the number of ROE photons for the channel $\Upsilon(3S) \to S\Lambda\Lambda\, 4\pi_s$. Each of the 24 canvases represents a specific configuration, and shows all generated mass values. The x-axes report the values to which the exclusive cut was applied, namely $nROE\_Photons\_EXZY < x$ for every x value. The boxes in the upper right corner of each plot represent a zoom in the region within the grey square (lower left corner).

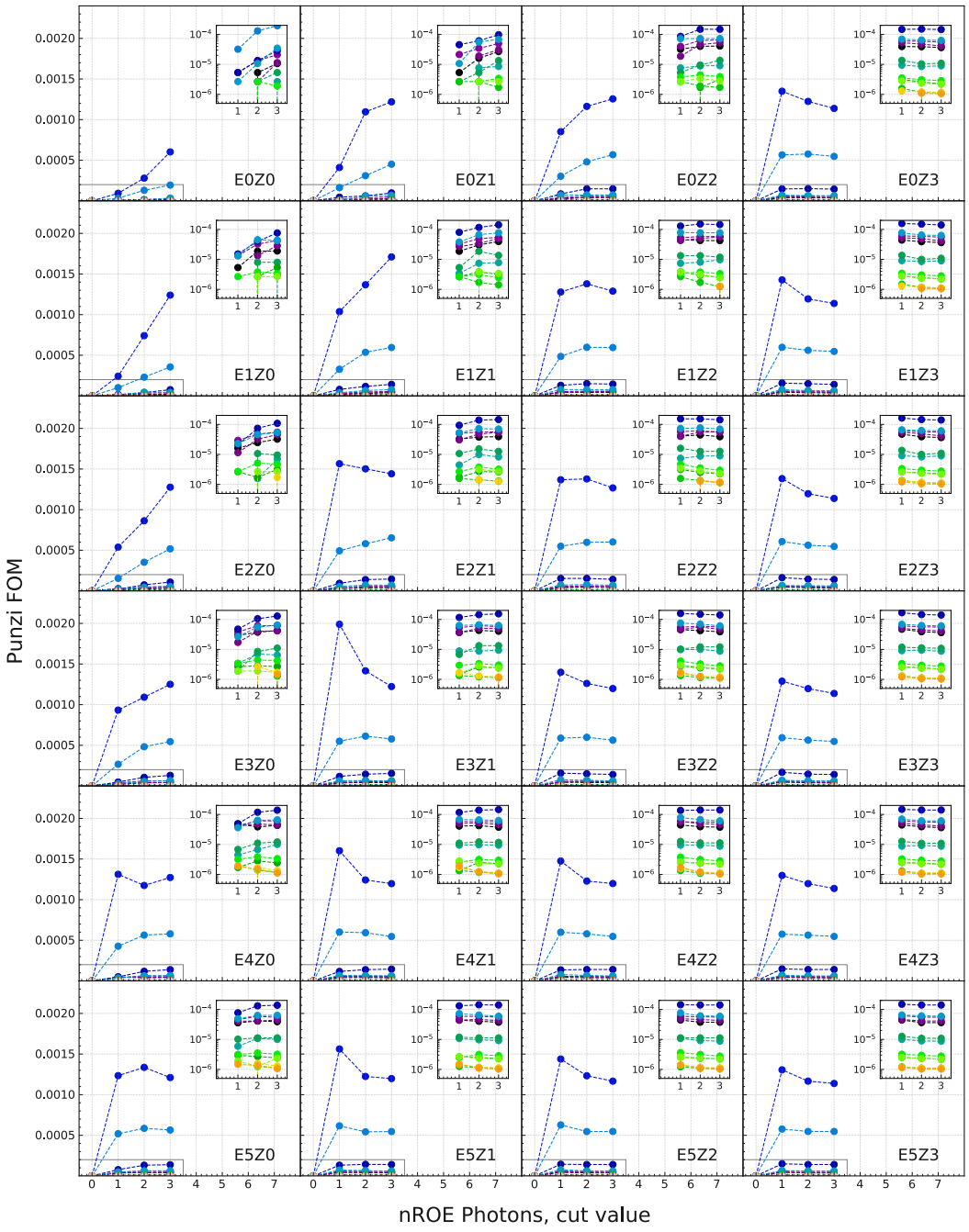

Figure 7.12: Punzi FOM trend as a function of the cut imposed on the number of ROE photons for the channel $\Upsilon(3S) \to S\Lambda\Lambda\, 6\pi_s$. Each of the 24 canvases represents a specific configuration, and shows all generated mass values. The x-axes report the values to which the exclusive cut was applied, namely $nROE\_Photons\_EXZY < x$ for every x value. The boxes in the upper right corner of each plot represent a zoom in the region within the grey square (lower left corner).

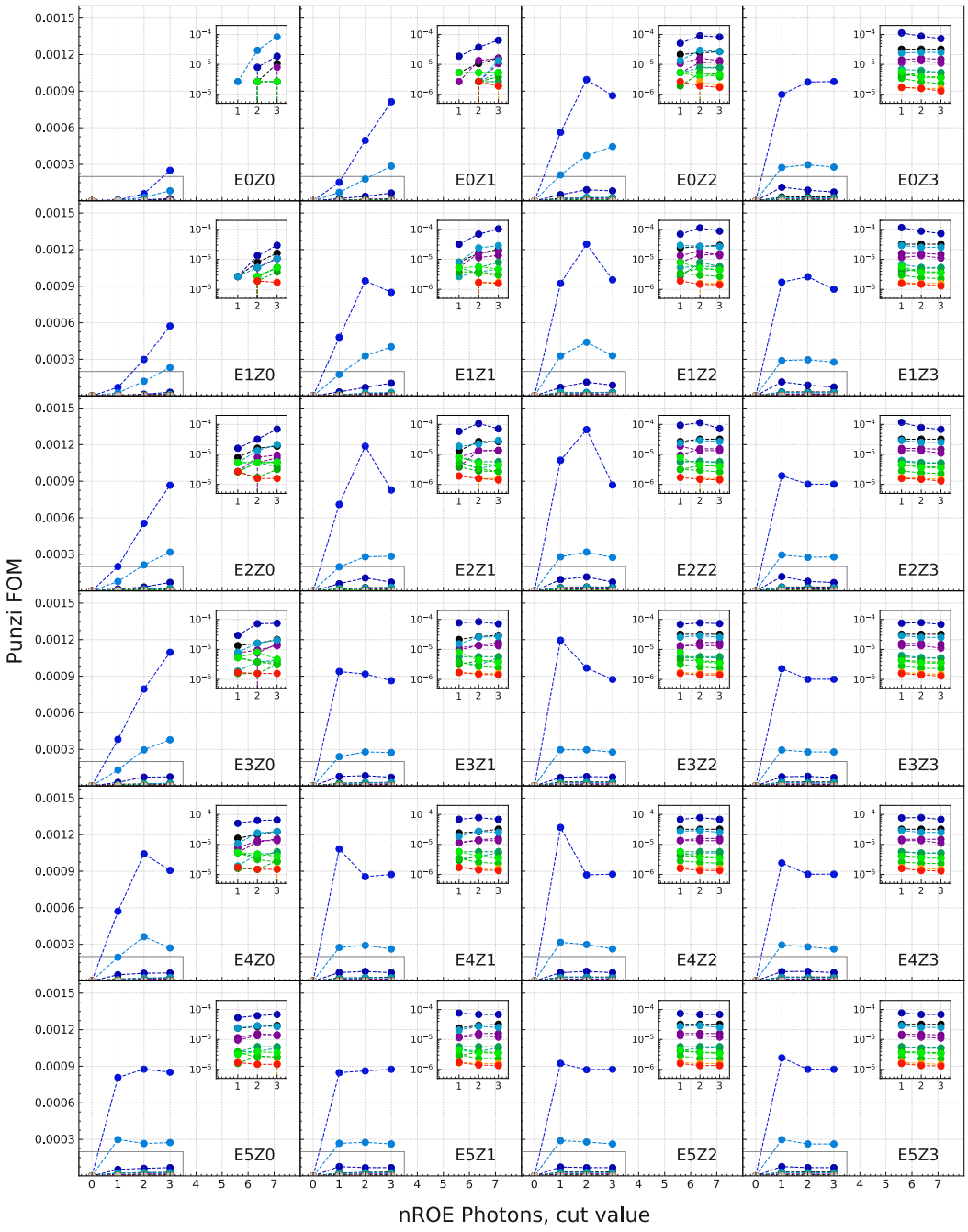

Figure 7.13: Punzi FOM trend as a function of the cut imposed on the number of ROE photons for the channel $\Upsilon(3S) \to S\Lambda\Lambda\, 8\pi_s$. Each of the 24 canvases represents a specific configuration, and shows all generated mass values. The x-axes report the values to which the exclusive cut was applied, namely $nROE\_Photons\_EXZY < x$ for every x value. The boxes in the upper right corner of each plot represent a zoom in the region within the grey square (lower left corner).

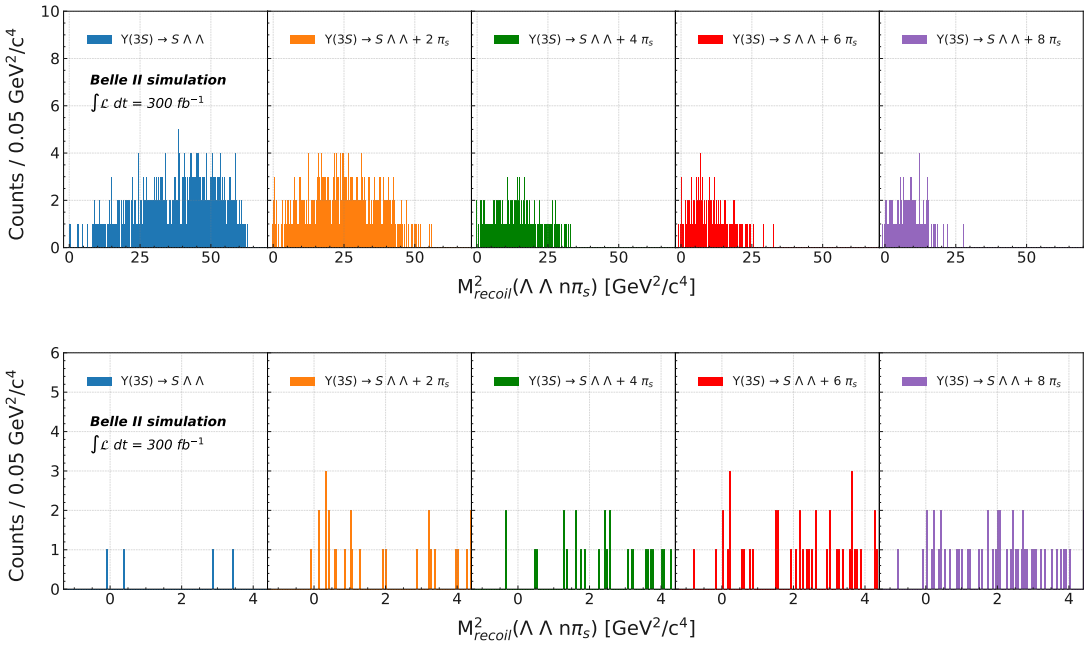

Figure 7.14: Events left in the background sample after applying all the selections. The upper panel shows a very large range in M^2_{recoil}, while the lower panel is a zoom in the interesting region for the analysis.

Figure 7.14 shows — for all the different channels — the distribution of the events from the background sample surviving the selection as a function of the square of the mass recoiling against the two Λ baryons and the primary pions, both in a very large range (upper panel) and in the interesting region for the analysis (lower panel). In particular, from the lower panel one can see that, regardless of the considered channel, only very few background events survive the selection procedure in the interesting mass region. Figure 7.15 shows an example of the distribution of the recoil mass squared of one signal MC sample (M_S =

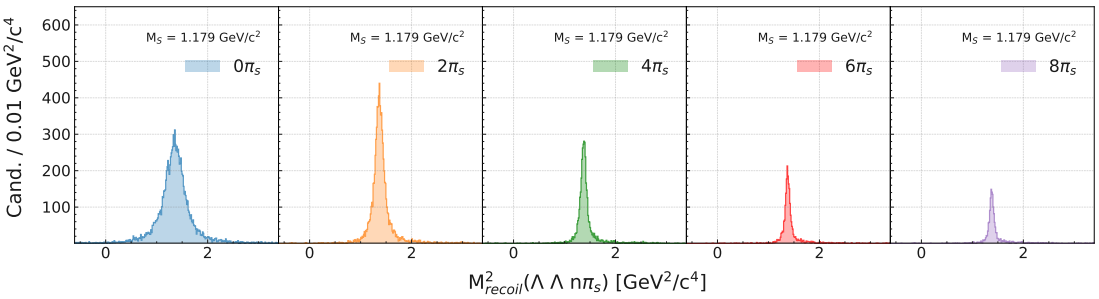

Figure 7.15: Distributions of the invariant mass squared of the system recoiling against the two Λ candidates and $n\pi_s$ after applying all the selections. Moving from left to right, n = 0, 2, 4, 6, and 8, respectively. The generated hexaquark mass used in this example is $M_S = 1.179$ GeV/c^2.

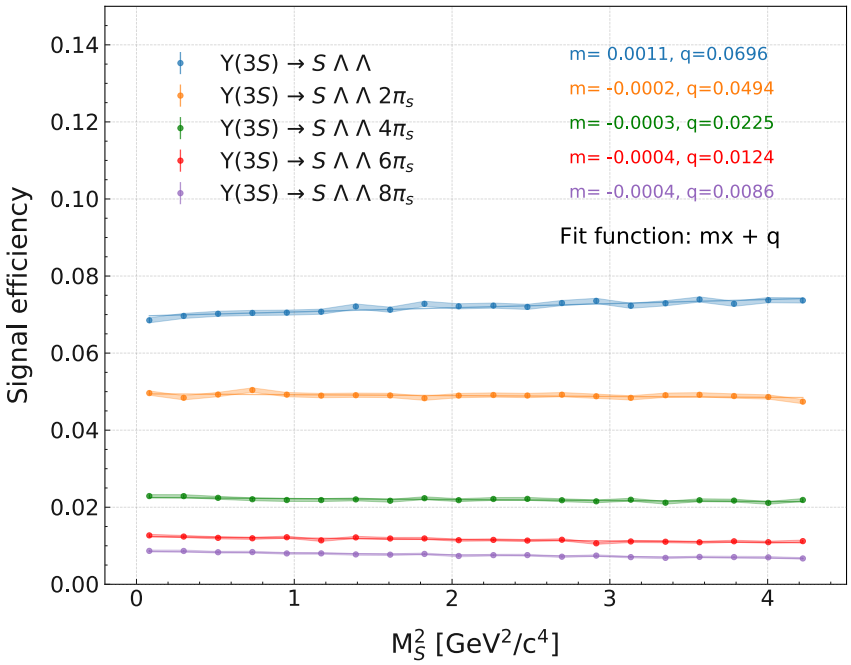

Figure 7.16: Signal efficiency as a function of the hexaquark mass squared, after applying the selections. The definition of signal efficiency is given in Eq. (7.9). For each channel, the points were fitted with a first order polynomial. The obtained functions are represented as solid lines, and the fit parameters are reported in the top right corner of the canvas. The colored bands show the statistical error on the efficiency extrapolations.

1.179 GeV/c^2) for the different channels, after applying all the selections. Figure 7.16 shows the signal efficiency as a function of the hexaquark mass squared. For each mass value, the efficiency is defined as:

$$\epsilon_S(M_S) = \frac{\#\text{ correctly reconstructed events after selection}}{N_{gen}}, \tag{7.9}$$

where the definition of "correctly reconstructed events" is the same as discussed in Section 7.1, and $N_{gen} = 150{\times}10^3$ is the number of generated hexaquarks for each mass value ($75{\times}10^3$ events with two Λ baryons and $75{\times}10^3$ events with two $\bar{\Lambda}$ baryons). For each channel, the efficiency distribution as a function of M_S^2 was fitted with a first order polynomial. In such a way, the discrete values of $\epsilon(S)$ were converted into a continuous function of M_S^2. The fit parameters are reported in Fig. 7.16, as well. For the UL extraction, the null hypothesis assumption is that no signal events are present in the data sample. In this way, one can estimate an UL on the signal strength within a certain CL. Under the assumption of a Poisson counting experiment with average number of background events F, an upper limit

S_{up} on the number of signal events within a certain Credibility Interval (CI) can be constructed as [153]:

$$CI = \frac{\int_0^{S_{up}} \left[(S+F)\, e^{-(S+F)}/n!\right] P(S) dS}{\int_0^{\infty} \left[(S+F)\, e^{-(S+F)}/n!\right] P(S) dS} \,. \tag{7.10}$$

In this equation, $P(S)$ represents the prior probability for S, and n represents the number of events actually observed in the experiment. Under the assumption that $P(S)$ is constant for each S, Eq. (7.10) becomes:

$$1 - CI = e^{-S_{up}} \, \frac{\sum_{m=0}^{n} (S_{up}+F)^m/m!}{\sum_{m=0}^{n} F^m/m!} \,. \tag{7.11}$$

Equations (7.10) and (7.11) are derived using a Bayesian assumption, resulting in the impossibility for the number of background events to be larger than the total number of events observed in the experiment. In this light, S_{up} can be interpreted as the upper limit on the average number of signal events that makes the integrated probability of observing n events not larger than CI, when on average F background events are present. In this specific case the null hypothesis implies $n = F$, meaning that all the events found originate from background.

Assuming the null hypothesis, the UL for the channel branching ratio at a given mass M_S can be written as:

$$UL(M_S) = \frac{S_{up}(F(M_S), CI)}{N_{\Upsilon(3S)}\, \epsilon_S(M_S)} \,. \tag{7.12}$$

To solve the equation, S_{up} is derived from Eq. (7.11) with a numerical evaluation. In this case, F represents the number of background events found in a window around the considered mass squared, [M_S^2 - $\frac{1}{2}$ FWHM, M_S^2 + $\frac{1}{2}$ FWHM], $\epsilon_S(M_S)$ represents the signal efficiency, and $\mathrm{N}_{\Upsilon(3S)}$ is the number of $\Upsilon(3S)$ present in the sample. $\mathrm{N}_{\Upsilon(3S)}$ depends on the cross section $e^+e^- \to \Upsilon(3S)$ and on the collected luminosity:

$$N_{\Upsilon(3S)} = \mathcal{L}_{\Upsilon(3S)}\, \sigma(e^+e^- \to \Upsilon(3S)). \tag{7.13}$$

For the results shown here, we set $\sigma(e^+e^- \to \Upsilon(3S)) = 4.2$ nb [11, 154].

As already mentioned in Section 7.2.3, the values of $\frac{1}{2}$FWHM obtained from the fit to the signal sample after applying the selections (see in particular the right panel of Fig. 7.7) suggest that the 20 mass values are not the best choice for the scan in the recoil mass squared. The same concept is shown in Fig. 7.17. Here the range covered using the 20 mass values, when using as a scan window

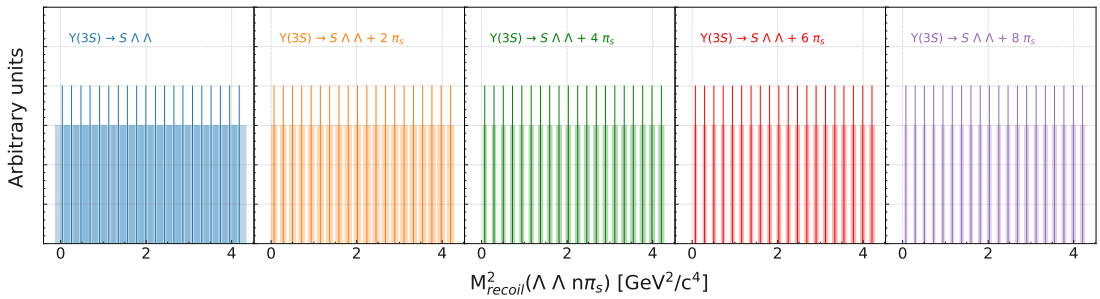

Figure 7.17: Ranges covered using the 20 mass values when performing a scan in windows [M_S^2 - $\frac{1}{2}$ FWHM, M_S^2 + $\frac{1}{2}$ FWHM]. In the channels with primary pion pairs in the final state, with this approach various region are left uncovered.

[M_S^2 − $\frac{1}{2}$ FWHM, M_S^2 + $\frac{1}{2}$ FWHM] is shown. Since various regions are left uncovered it is evident that — in case of primary pion pairs in the final state — this is not an optimal approach. To avoid this problem, five new sets of masses were defined, one for each channel, and used to fine-tune the scan. For the definition, an equation similar to Eq. (7.4) was used, but in this case instead of a constant pitch the value of $\frac{1}{2}$FWHM(M_S^2) coming from the fit (showed in the right panel of Fig. 7.7) was used:

$$M_{S,i-1} = \sqrt{M_{S,i}^2 - \frac{1}{2}\text{FWHM}(M_S)} \tag{7.14}$$

As a final result, the new sets of masses contain 26, 59, 83, 99, and 111 values, respectively. Figure 7.18 shows the upper limit estimation for the five channels, when setting the CI to be 90%, for an integrated luminosity $\mathcal{L} = 300$ fb^{-1}. In the plots, the $\pm1\sigma$, $\pm2\sigma$, $\pm3\sigma$ bands represent the quantiles evaluated at (0.32, 0.68), (0.05, 0.95), and (0.01, 0.99), respectively, when performing 10^4 extrapolations of the UL. For these 10^4 tests, the number of background events F for each mass scan was randomly sampled following a Poissonian distribution. As a parameter of the distribution (λ), the average number of events expected in each interval was used:

$$\lambda = \text{Number of events expected per GeV}^2/\text{c}^4 \times \text{width of } {M_S}^2 \text{ window}\,. \tag{7.15}$$

For each channel, the number of events expected per GeV^2/c^4 is evaluated as the number of events found in the whole signal region divided by the width of the region itself. In this context, the signal region was fixed to [0.0, 5.0] GeV^2/c^4.

Finally, the evolution of the UL as a function of the integrated luminosity was evaluated, and it is shown in Fig. 7.19 for the five different final states.

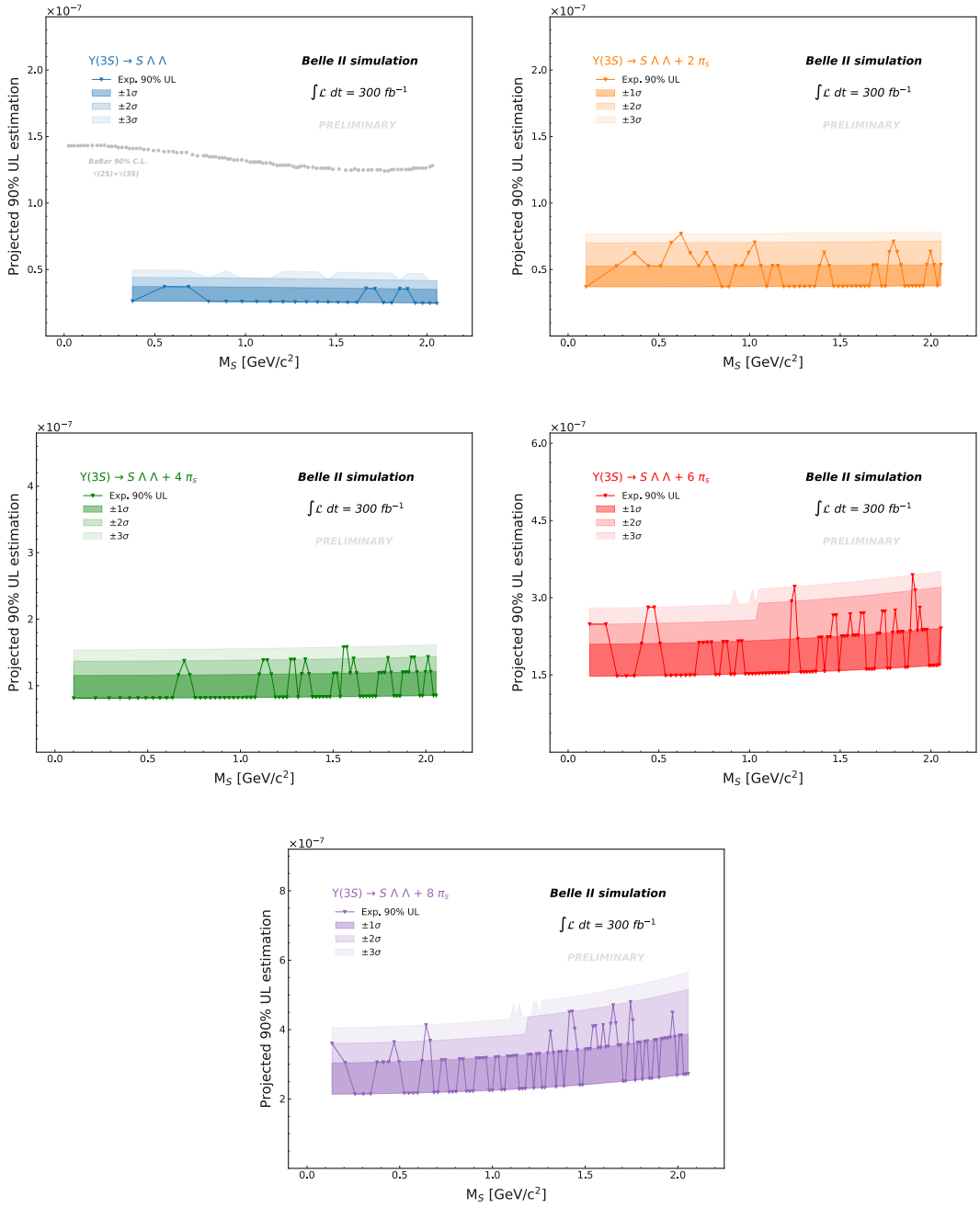

Figure 7.18: Estimation of the UL as a function of the hexaquark mass M_S, with CI=90%. In each plot, the colored bands represent $\pm1\sigma$, $\pm2\sigma$, $\pm3\sigma$ regions from the lower to the higher transparency, respectively. In the top left panel, corresponding to the channel with no primary pion pairs in the final state, the existing UL set by BaBar [112] is represented as well.

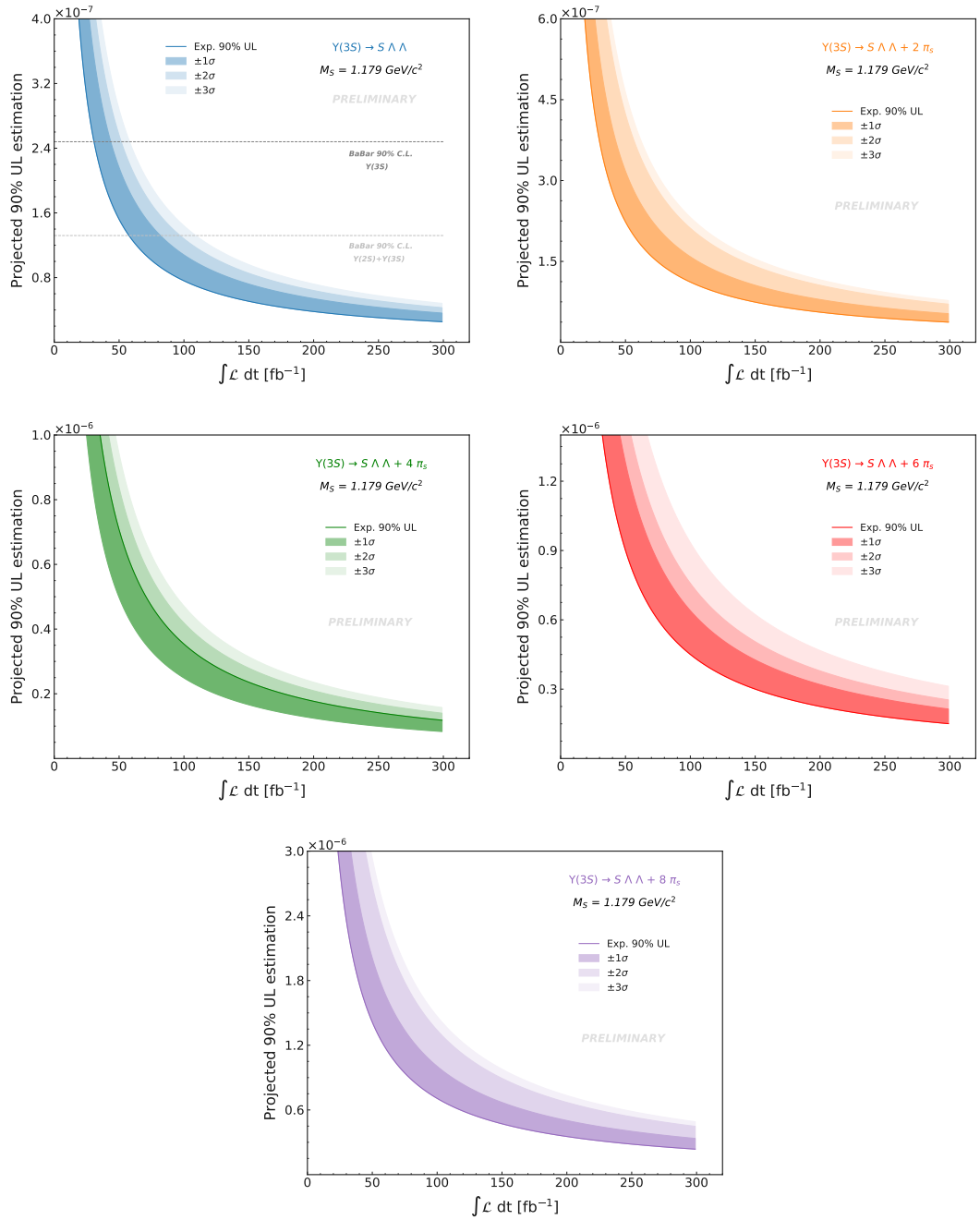

Figure 7.19: Estimation of the UL as a function of the integrated luminosity, with CI=90%. In each plot, the colored bands represent $\pm1\sigma$, $\pm2\sigma$, $\pm3\sigma$ regions from the lower to the higher transparency, respectively. In the upper left panel, corresponding to the channel with no primary pion pairs in the final state, the existing UL set by BaBar [112] is represented as well.

8

Benchmark studies

After an initial commissioning phase and early data taking without the VXD, on March 25th, 2019 the first collisions of the actual Belle II physics program were detected, and the experiment is collecting data since then. So far, almost all data were collected at the energy of the $\Upsilon(4S)$ resonance [1]. However, the search for a stable hexaquark will require to analyze data collected at the $\Upsilon(3S)$ energy, and everything shown so far was based on MC only. Yet, there are some aspects of the planned analysis that can be benchmarked using the available data sample collected up to now. Such a dataset can be used to compare results with those obtained using MC, in order to check whether the simulation is in agreement with the experimental observations, and — when needed — to work towards its improvement.

This chapter will introduce some performance studies focused on Λ baryons carried out using the $\Upsilon(4S)$ dataset collected up to the summer 2021, corresponding to an integrated luminosity of 189.88 fb^{-1}. As for the MC, an official Belle II MC campaign, corresponding to an integrated luminosity of 200 fb^{-1}, has been used. The difference in luminosity between the data and MC samples is addressed

[1] A small amount of data was collected off-resonance. Also, at the end of 2021 a special scan was collected around $\Upsilon(10750)$.

by the introduction of a normalization factor k_L for the MC sample:

$$k_L = \frac{\mathcal{L}_{data}}{\mathcal{L}_{MC}} = \frac{189.88 \text{ fb}^{-1}}{200.00 \text{ fb}^{-1}} = 0.95 \,. \tag{8.1}$$

Two different Λ channels have been explored: an exclusive Λ sample coming from the Λ_c decay $\Lambda_c^+ \to \Lambda^0 \pi^+$ (Section 8.1), and an inclusive Λ sample (Section 8.2). In both cases the selection applied in order to select good Λ candidates is the same as described in Section 6.3. The two samples are to some extent complementary: if the exclusive sample provides information on Λ truly coming from physics events, but with a specific kinematics and limited statistics, the inclusive sample offers huge statistics to be analyzed, but is prone to include many more fake candidates (this concept will be taken up later in the chapter). Part of this work is also described in an internal Belle II note, whose sections about Λ baryons were written by the author of the thesis herself [155].

The comparison between MC and data is done considering some relevant kinematics variables and plotting the data-MC ratio as their function. For samples with the same luminosity, an ideal agreement between data and MC would lead to a constant ratio of 1. In order to count the number of signal candidates a sideband subtraction approach was used. This kind of approach is justified in the presence of linear behavior of the background. The definitions of mass region and sidebands are related to the width σ_{68} of the $p\pi$ invariant mass distribution, defined using quantiles Q. More precisely, σ_{68} is defined as half of the difference between $Q[0.84]$ and $Q[0.16]$:

$$\sigma_{68} = \frac{Q[0.84] - Q[0.16]}{2} \,. \tag{8.2}$$

The mass region (MR) is limited by the two values:

$$MR \in (\mathrm{M}_\Lambda - \sigma_{68},\, \mathrm{M}_\Lambda + \sigma_{68}) \,, \tag{8.3}$$

while the left (S_L) and right (S_R) sidebands:

$$S_L \in (\mathrm{M}_\Lambda - 6\,\sigma_{68},\, \mathrm{M}_\Lambda - 5\,\sigma_{68}), \quad S_R \in (\mathrm{M}_\Lambda + 5\,\sigma_{68},\, \mathrm{M}_\Lambda + 6\,\sigma_{68}) \,. \tag{8.4}$$

In both Eqs. (8.3) and (8.4), M_Λ is set to $\mathrm{M}_\Lambda = 1115.68$ MeV/c^2, and refers to the nominal Λ mass value [11]. The choice of $5\,\sigma_{68}$ and $6\,\sigma_{68}$ in the sidebands definition is arbitrary, but ensures to be enough far away from the mass region. The specific numerical values used for σ_{68}, MR, S_L, and S_R are sample-dependent and they

are reported in Appendix E. Unless otherwise specified, all the plots presented in the next sections are obtained after the sideband subtraction.

8.1 Λ from $\Lambda_c^+ \to \Lambda^0 \pi^+$

The first Λ sample benchmarked is an exclusive sample deriving from the decay of the charmed hyperon $\Lambda_c^+ \to \Lambda^0 \pi^+$. In addition to the selection imposed on Λ, described in Section 8.2, some cuts were applied to the final state π and to the mother particle Λ_c. Concerning the π, since it is expected to originate somewhere close to the IP, the absolute distance of the track's POCA in the r-ϕ plane ($|d_0|$) and in the z plane ($|z_0|$) were required to be $|d_0| < 0.5$ cm and $|z_0| < 3.0$ cm, respectively. Concerning the Λ_c candidate, its momentum in the center-of-mass frame p_{CMS} was required to be $2.7 < p_{CMS} < 5.0$ GeV/c, and the invariant mass of the $\Lambda\pi$ system was required to lie in the interval $2.12 < M(\Lambda\pi) < 2.45$ GeV/c^2, being the Λ_c nominal mass value $M_{\Lambda_c} = 2.286$ GeV/c^2 [11]. Finally, a vertex fit — with CL set to 0.0 — was performed. Unlike the cut values used for the Λ sample, these additional requirements were not optimized, but rather adapted from a Belle II internal note [156].

Figure 8.1 shows the invariant mass distribution of the $\Lambda\pi$ system. The black points represent data, while the blue points represent MC. The MC sample is normalized using the factor k_L defined in Eq. (8.1). As one can see from the figure, the shape of the data and normalized MC is similar, but there seems to be an overall shift between the two distributions. In order to match them, an additional factor (ϵ) should be introduced, obtained as the ratio between the number of signal events inside the Λ_c mass region in data and in the luminosity-scaled MC:

$$\epsilon = \frac{\#\text{ events in mass region, data sample}}{\#\text{ events in mass region, lumi-scaled MC sample}} = 0.816\ . \tag{8.5}$$

The factor ϵ could be interpreted as an overall difference in performance between MC and data, with MC overestimating the performance. For the definition of mass region, both the data and the MC sample were fitted using a double Gaussian (f_a) and a first order polynomial (f_b). The double Gaussian f_a was defined as:

$$f_a = N \left(f\ \frac{e^{\frac{-(x-\mu_1)^2}{2\sigma_1^2}}}{\sigma_1\sqrt{2\pi}} + (1-f)\ \frac{e^{\frac{-(x-\mu_2)^2}{2\sigma_2^2}}}{\sigma_2\sqrt{2\pi}} \right), \tag{8.6}$$

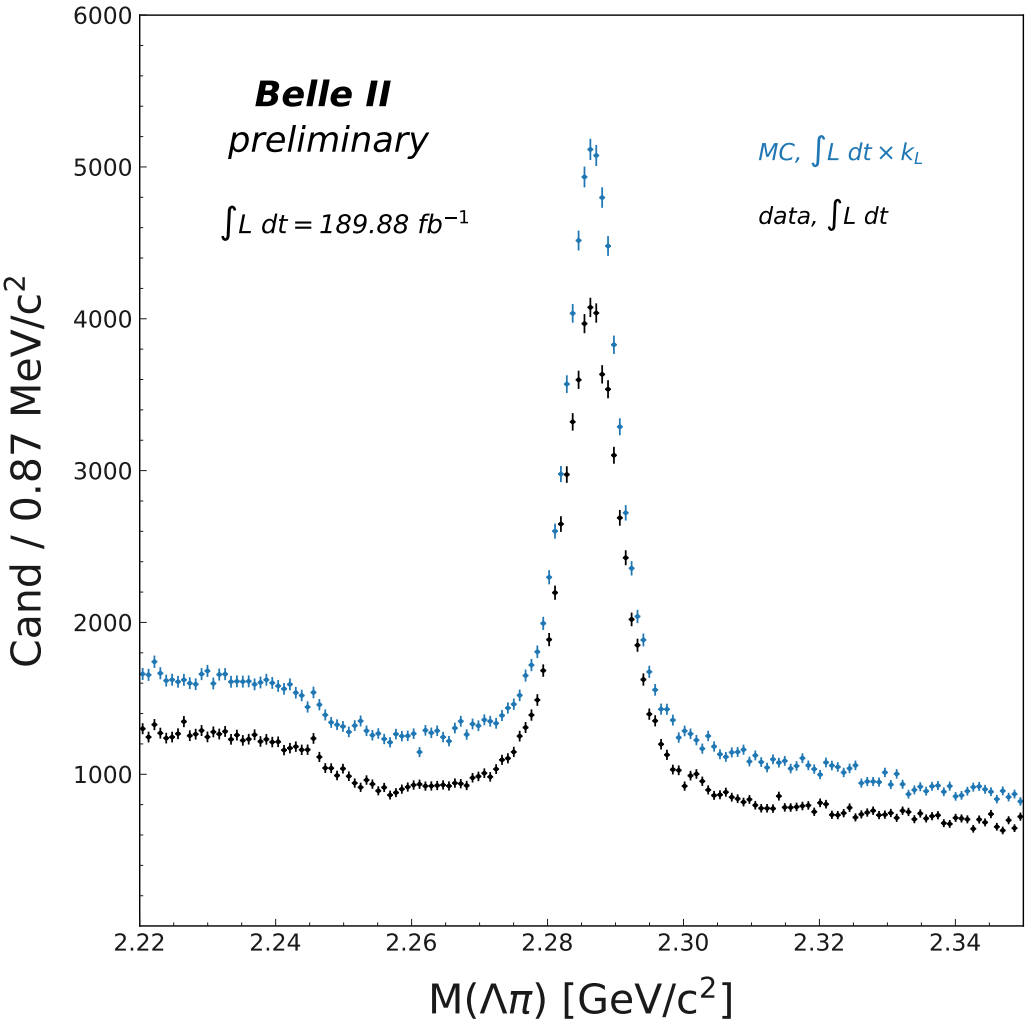

Figure 8.1: $\Lambda\pi$ invariant mass peak, both for the MC sample (blue points) and the data sample (black points). The MC sample is normalized using the factor k_L, introduced in Eq. (8.1), that takes into account the different luminosities of the two samples.

with

$$\mu_2 = \mu_1 + \Delta\mu\,, \tag{8.7}$$

and

$$\sigma_2 = \sqrt{\sigma_1^2 + \sigma_{tail}^2}\,. \tag{8.8}$$

The presence of the second Gaussian allows the fit to take into account and describe possible small shifts and tails in the distribution. The mass region was taken to be $\pm 2\,\sigma_c$ around the nominal Λ_c mass value, where σ_c is the weighted sum of σ_1 and σ_2 from the double Gaussian:

$$\sigma_c = \sqrt{\sigma_1^2 + \sigma_2^2}\,. \tag{8.9}$$

As for the first order polynomial f_b, it was defined simply as:

$$f_b = a \,+\, bx\,. \tag{8.10}$$

The result of the fit on the invariant mass of the $\Lambda\pi$ system, both for the MC (left panel) and the data (right panel) sample, is shown in Fig. 8.2. The values of the parameters extracted from the fits can be found in Appendix E.

The result of weighting the MC sample with the additional factor ϵ is shown in Fig. 8.3, where the newly obtained histogram (green) is drawn on top of the points already shown in Fig. 8.1. In the bottom panel the pulls are shown, namely the difference — bin per bin — between the data and the normalized MC distribution (green histogram) divided by the error:

$$\text{Pulls} = \frac{\#\,\text{data} - \#\,\text{MC}}{\sqrt{\sigma_{data}^2 + \sigma_{MC}^2}}\,, \tag{8.11}$$

where σ_{data} (σ_{MC}) is the square root of the counts in each bin of the data (MC) histogram. The orange band represents the $\pm 3\sigma$ region in the data-MC difference. As one can see, the introduction of a weight ϵ for the MC sample leads to a better overall agreement between data and MC, with almost all the pulls contained in the $\pm 3\sigma$ region.

Similarly, Fig. 8.4 shows the invariant mass distribution of the $p\pi$ system — namely the Λ candidates — both for MC and data. Only candidates inside the Λ_c signal region were considered. As in Fig. 8.3, also here the MC sample is shown with the two different normalizations discussed (blue points and green histogram). Black points represent data. In the bottom panel the pulls distribution is shown, with the relative $\pm 3\sigma$ region highlighted (orange band). Also in this case, the

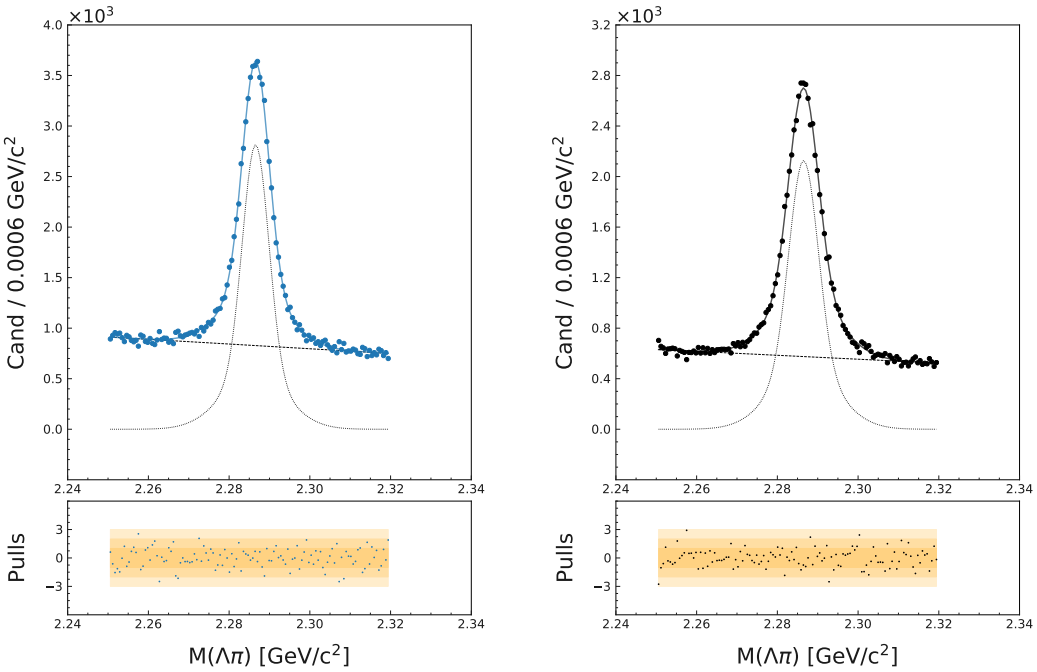

Figure 8.2: Fit to the $\Lambda\pi$ invariant mass peak, both for the MC sample (left panel) and the data sample (right panel). The fit function used is a double Gaussian and a first order polynomial. Its precise definition can be found in the text, and the values of the parameters extracted from the fits are reported in Appendix E. The pulls shown in the bottom panels are defined as the difference between the experimental points and the fit function divided by the error, and the orange bands represent the $\pm 3\sigma$ region.

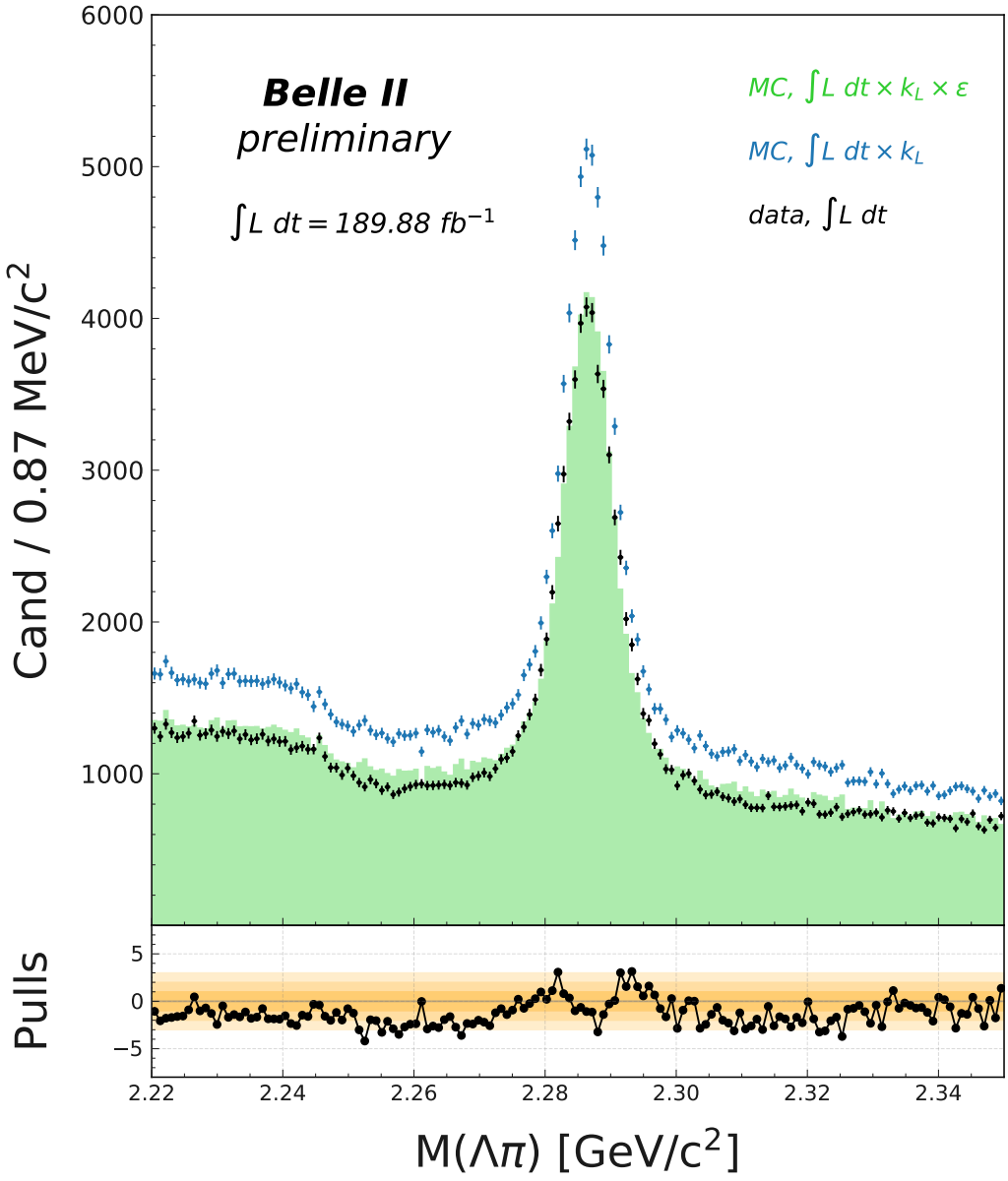

Figure 8.3: $\Lambda\pi$ invariant mass peak, both for the MC and the data sample. With respect to Fig. 8.1, an additional green histogram — resulting after weighting the MC sample with the factor ϵ (see Eq. (8.5)) — has been added. In the bottom panel the pulls distribution, namely the difference between data and normalized MC (green histogram) divided by the error, is shown. The exact definition of pulls is given in Eq. (8.11). The orange band represents the $\pm 3\sigma$ region.

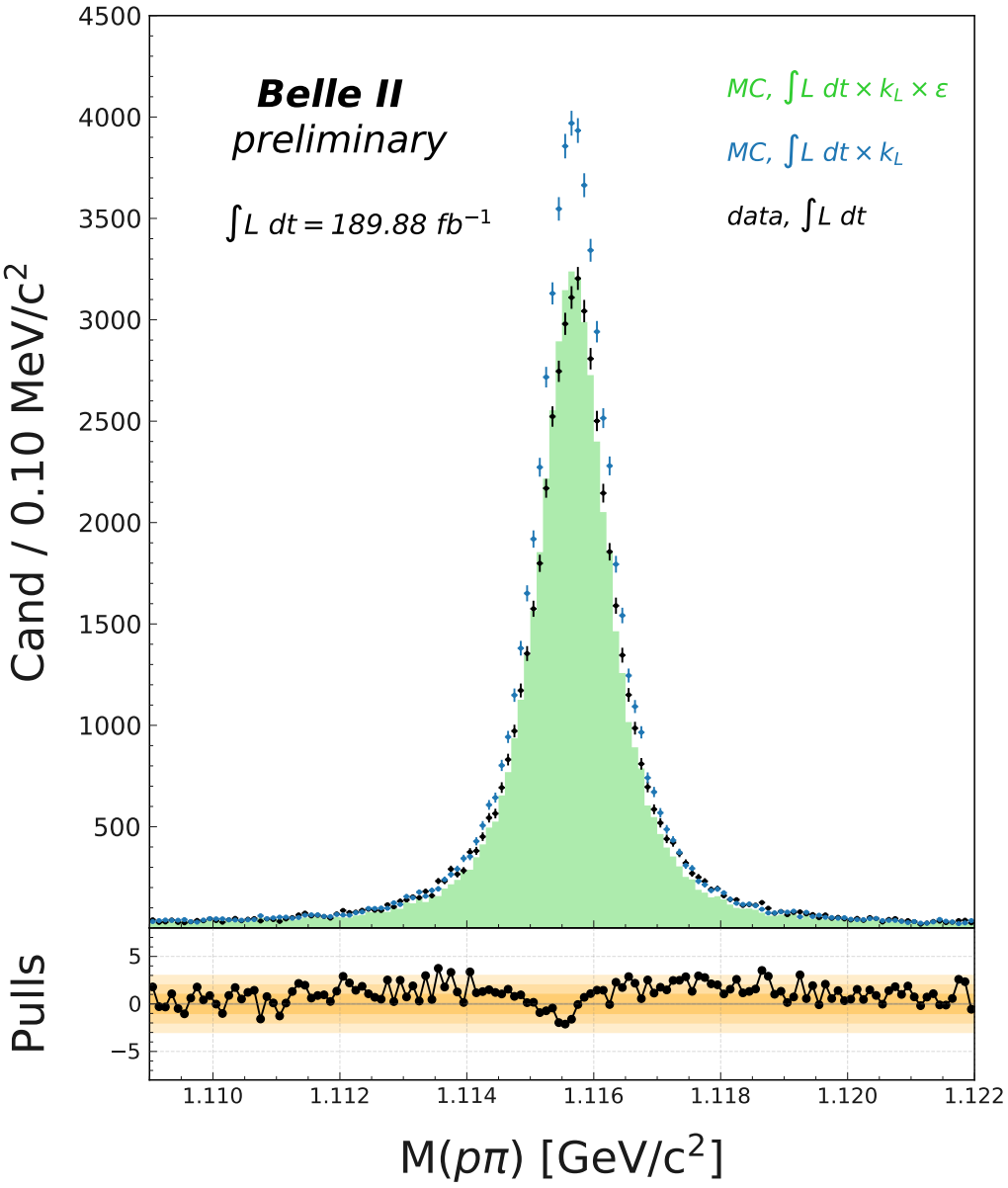

Figure 8.4: $p\pi$ invariant mass peak, both for the MC and the data sample. Two different normalizations for the MC sample are used, resulting in the blue points and the green histogram. Only Λ candidates in the Λ_c mass region are considered. In the bottom panel the pulls distribution, namely the difference between data and normalized MC (green histogram) divided by the error, is shown. The exact definition of pulls is given in Eq. (8.11). The orange band represents the $\pm 3\sigma$ region.

introduction of ϵ is enough to match the invariant mass distributions in data and MC.

Even if an overall factor can, at first glance, account for the difference between data and MC, this very simplistic approach is not fully justified, and such a difference should be further investigated. Generally speaking, interesting quantities to monitor, and to be checked both in MC and data, are the mean value μ_{50} and the width σ_{68} of the $p\pi$ invariant mass peak. A possible difference in resolution between data and MC could point to problems of various kind, both in simulation or reconstruction. More specifically, it may prove useful to monitor such quantities in bins of relevant variables, and in the case of Λ baryons the natural candidate is their flight distance. Figure 8.5 shows μ_{50} and σ_{68} as a function of the Λ flight distance in the transverse plane (xy-distance). The mean μ_{50}, shown in the left panel of Fig. 8.5, is obtained as the quantile $Q[0.50]$ of the mass distribution in each transverse distance bin, in blue for MC and in black for data. The error bands are estimated as the region between the quantiles $Q[0.48]$ and $Q[0.52]$. At the bottom of the canvas the ratio between data and MC is shown, as well. The mean value μ_{50}, both for data and MC, within the VXD volume is close to the nominal mass value [11], represented in the figure as a dashed red line. Moving further away from the IP one starts to notice some differences, but they are limited to less than 2 MeV/c^2. In the right panel, the width σ_{68} — defined in Eq. (8.2) — is shown, both for MC (blue points) and data (black points). Also in this case, at the bottom of the canvas the ratio between data and MC is plotted. At low distances the width is similar when comparing data and MC, while the difference increases when moving away from the IP. The width does not show an overall dependence on the flight distance in the transverse plane. In both panels, some structures are visible near the different layers of the VXD, represented in the plot as vertical dashed lines. In most cases, however, such structures are present both in data and MC, and they are not a feature of only one of the two samples.

The distribution itself of the Λ flight distance in the transverse plane, when comparing data and MC, contains some interesting information. The left panel of Fig. 8.6 shows such a distribution, both for data (black points) and MC (blue points). In the right panel the ratio between data and MC is shown, as a function of the same variable. This specific plot is the one that carries the most interesting information: close to the IP the ratio takes on a value approximately equal to one, and then it decreases when moving away from the origin. Looking closely, one can see some feature of the distribution corresponding to the VXD layers,

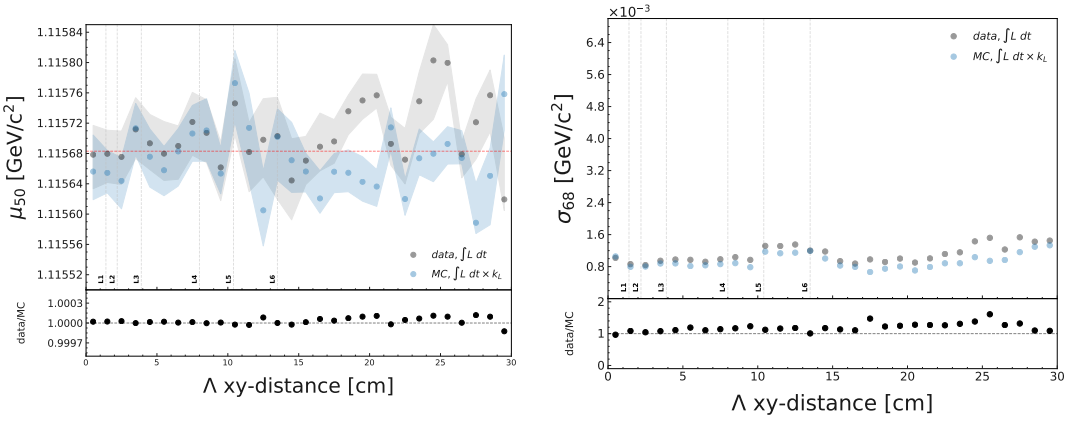

Figure 8.5: Mean value μ_{50} (left panel) and width σ_{68} (right panel) of the M($p\pi$) peak as a function of the flight distance in the transverse plane. The dashed red line in the left panel represents the nominal value of the Λ mass [11]. The exact definition of these two quantities (μ_{50} and σ_{68}) can be found in the text. In both panels, blue points represent the MC sample and black points represent the data sample. Vertical dashed lines are drawn corresponding to the six VXD layers.

represented in the panels as vertical dashed lines, and pointing to some effects of interaction with the material not fully reproduced in the simulation. This observation motivated the choice of considering the 3D flight distance rather than its flight distance in the transverse plane, where the effect is milder.

Figure 8.7 shows the distribution of the Λ flight distance (left panel) and the ratio between data and MC as a function of the same variable. The trend of the ratio, similarly to the right panel of Fig. 8.6, assumes a value close to one near the IP, and then it decreases when moving away from it. The points have been fitted with a straight line, and the fit function is reported on the plot. The linear dependence of the data-MC ratio as a function of the flight distance points to a degradation of the performance in data with respect to MC for Λ decaying far from the IP. This observation is attributed to background contributions that affect tracking in the CDC and that are not yet perfectly modeled in MC. As it will be shown in the next chapter, the background conditions strongly influence the tracking performance, in particular in the case of the CDC.

Another piece of information, with different implications, can be extracted from the Λ momentum. Figure 8.8 shows its distribution (left panel) and the ratio between data and MC as a function of the same variable (right panel). The irregular shape of the ratio, increasing for low momentum baryons (below ∼2 GeV/c) and decreasing for high momentum baryons (above ∼2 GeV/c) points to an incorrect reproduction of the Λ kinematics in MC. The distribution itself results from the superposition of two main components, one with low and one

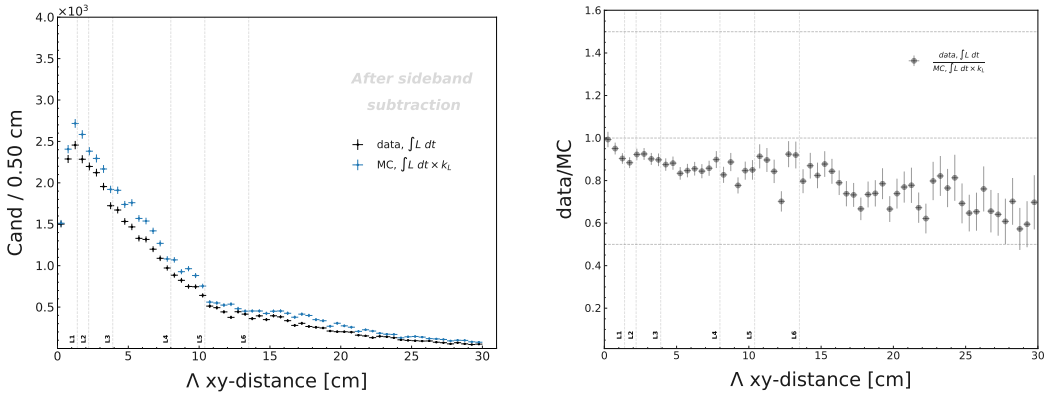

Figure 8.6: Distribution of the Λ flight distance in the transverse plane (left panel) and data-MC ratio as a function of the same variable (right panel). In the left panel, blue points represent MC, while black points represent data. The vertical dashed lines show the position of the VXD layers.

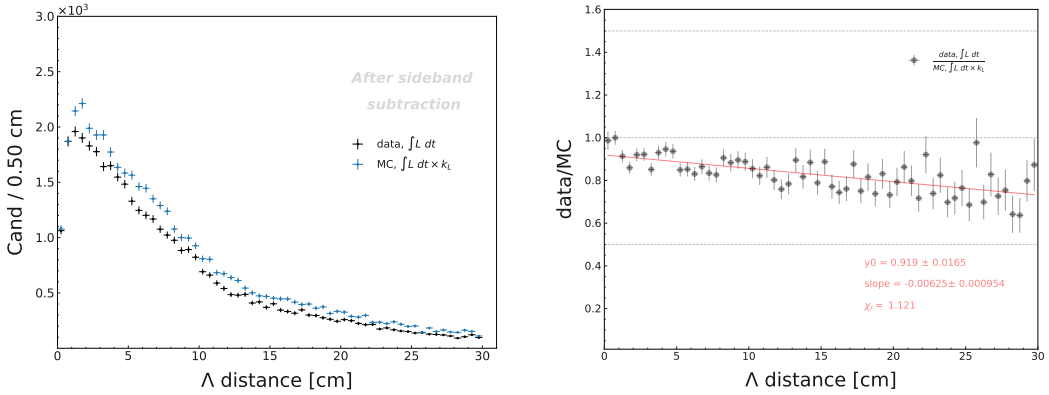

Figure 8.7: Distribution of the 3D Λ flight distance (left panel) and data-MC ratio as a function of the same variable (right panel). In the left panel, blue points represent MC, while black points represent data. In the right panel, he distribution of the ratio is fitted with a straight line, and the fit function is reported on the plot itself.

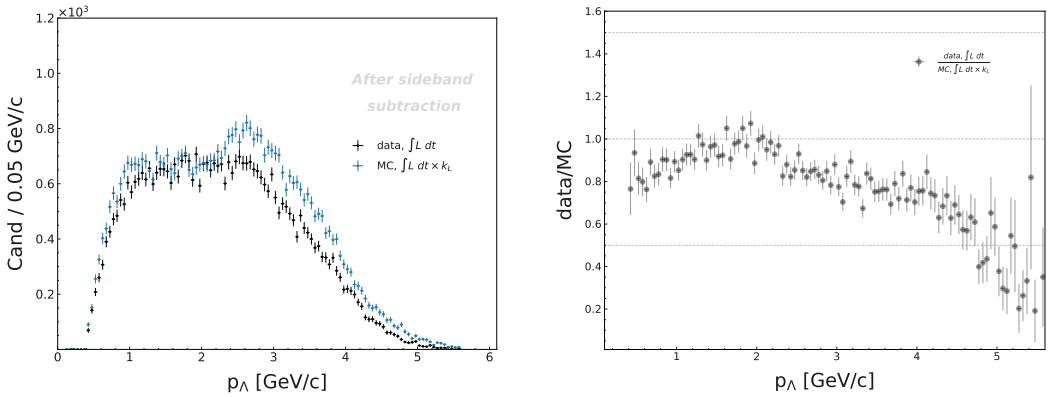

Figure 8.8: Distribution of the Λ momentum (left panel) and data-MC ratio as a function of the same variable (right panel). In the left panel, blue points represent MC, while black points represent data.

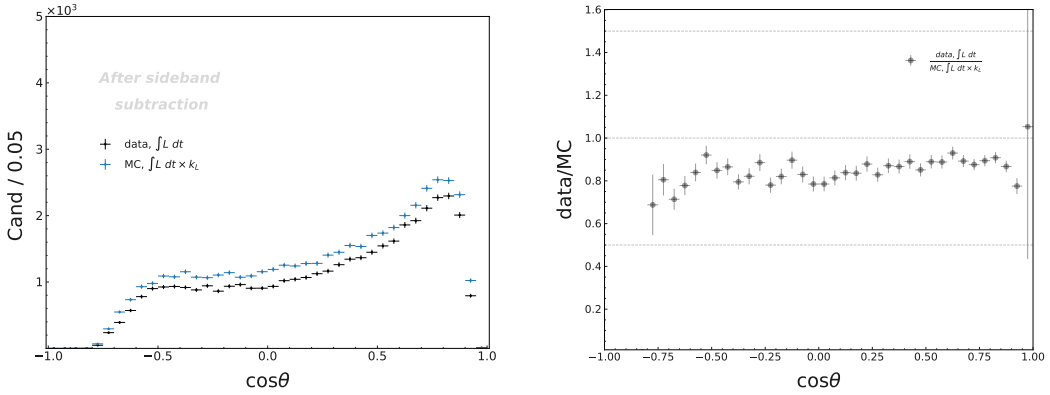

Figure 8.9: Distribution of the Λ polar angle (left panel) and data-MC ratio as a function of the same variable (right panel). In the left panel, blue points represent MC, while black points represent data.

with high average momentum, that — in different ways — are not correctly reproduced in MC. The problem, in this case, is to be sought in the MC event generator used and in the wrong tuning of some of its parameters.

Finally, Fig. 8.9 shows the distribution of the Λ polar angle (left panel) and the ratio between data and MC as a function of the same variable (right panel). In this case, when looking at the data-MC ratio, it does not show an overall dependency on this variable. Possible interplays between these variables were checked by plotting the data-MC ratio as a function of two variables simultaneously in the form of 2D plots. These distribution can be found in Appendix E (Section E.1). No particular structure was revealed, and the same message already inferred from the 1D distributions was confirmed: a mis-modeling of the Λ momentum spectrum and a deterioration in performance of data with respect to MC for Λ

decaying far from the IP.

8.2 Inclusive Λ sample

The second sample benchmarked is an inclusive Λ sample, consisting of all candidates reconstructed from one proton and one pion which pass the selections described in Section 6.3. Figure 8.10 shows the invariant mass distribution of the resulting $p\pi$ system. The black points represent data, while the blue points represent the MC sample, normalized using the factor k_L (see Eq. (8.1)). The green histogram, following the procedure already described in the previous section, represents also the MC sample, with an additional factor ϵ_2 considered for the normalization. As for the exclusive Λ sample, also in this case ϵ_2 was obtained empirically by comparing data and MC. It was defined as the ratio between the number of signal events in data and in the luminosity-scaled MC:

$$\epsilon_2 = \frac{\#\text{ signal events in data sample}}{\#\text{ signal events in lumi-scaled MC sample}} = 0.841. \tag{8.12}$$

In this case, "signal events" refers to the number of events in the signal region after the sideband subtraction. The definition of mass region and sidebands uses quantiles, and the exact numbers can be found in Section E.2. Already from this plot it can be seen that the situation is more complex than with the exclusive sample. The introduction of the overall factor ϵ_2 is not enough to make the data (black points) and MC (green histogram) distributions match: even after applying it there appears to be a lack of data in the mass region and an excess in the sidebands. This is clear when looking at the pulls distribution shown in the bottom panel of Fig. 8.10. Also in this case the orange band represents the $\pm 3\sigma$ region, and almost all the pulls lie outside it.

As in the case of the exclusive sample, the mean μ_{50} and width σ_{68} of the invariant mass peak as a function of the flight distance in the transverse plane has been investigated. The two distributions are shown in Fig. 8.11. The mean μ_{50}, shown in the left panel of the figure, is obtained as the quantile $Q[0.50]$ of the mass distribution in each transverse distance bin, in blue for MC and black for data. The error bands contain values included between the quantiles $Q[0.48]$ and $Q[0.52]$. At the bottom of the canvas the ratio between data and MC is shown as well. The trend, both for data and MC, increases with the transverse distance. It is smaller with respect to the nominal mass value [11] — represented in the figure as a dashed red line — for vertices inside the VXD, and then gradually

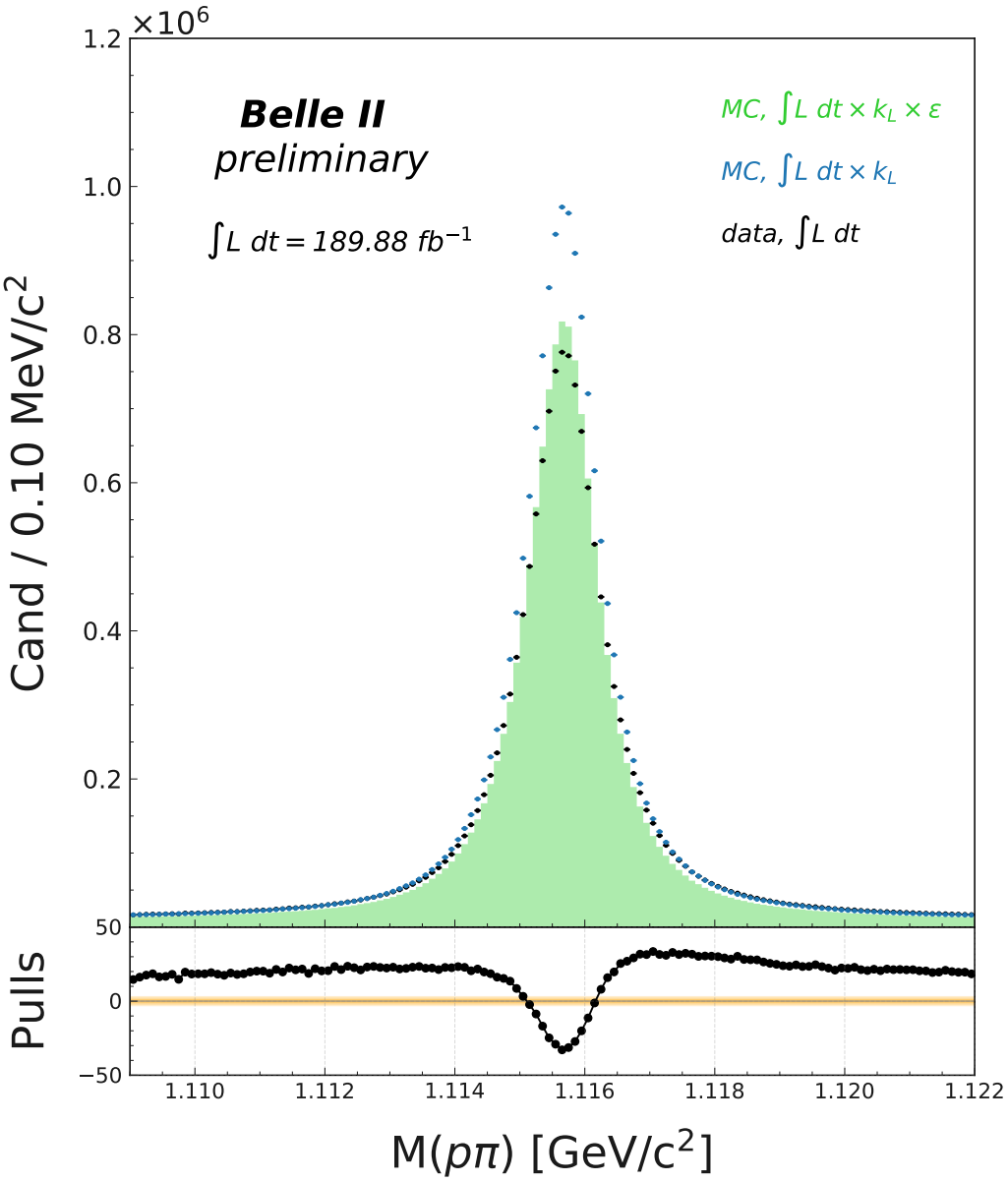

Figure 8.10: $p\pi$ invariant mass peak, both for the MC and the data sample. Two different normalizations for the MC sample — described in details in the text — are used, resulting in the blue points and the green histogram. In the bottom panel the pulls distribution, namely the difference between data and normalized MC (green histogram) divided by the error, is shown. The exact definition of pulls is given in Eq. (8.11). The orange band represents the $\pm 3\sigma$ region. To be noted is that the pulls y-scale is ten times wider than the ones in the previous section.

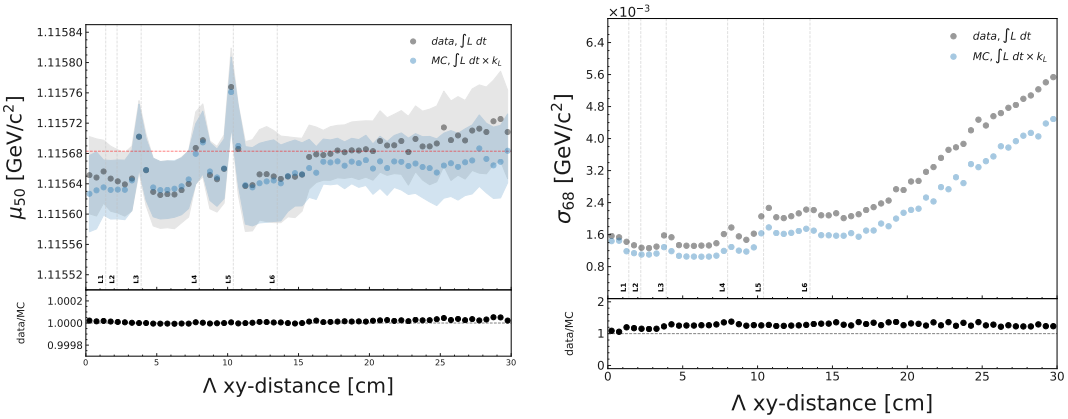

Figure 8.11: Mean value μ_{50} (left panel) and width σ_{68} (right panel) of the $p\pi$ invariant mass peak as a function of the flight distance in the transverse plane for the Λ inclusive sample. The dashed red line in the left panel represents the nominal value of the Λ mass [11]. The exact definition of these two quantities (μ_{50} and σ_{68}) can be found in the text. In both panels, blue points represent the MC sample and black points represent the data sample. Vertical dashed lines are drawn corresponding to the six VXD layers.

approaches the nominal value (and in case of data it crosses it). The difference between data and MC is more pronounced at large distances. Despite a generally smooth trend, three sharp peaks are visible corresponding to three of the SVD layers (L3, L4, and L5), both in data and MC. This effect points to a problem in the reconstruction in the proximity of this detector material, affecting both data and MC. In the right panel, the width σ_{68} — defined in Eq. (8.2) — is shown, both for MC (blue points) and data (black points). Also in this case, the ratio between data and MC is plotted at the bottom of the canvas. For this inclusive Λ sample, the width in data is systematically wider than that in MC. At low distances the width appears to be similar when comparing data and MC, while the difference increases when moving away from the IP. Unlike the case of the exclusive sample (see Fig. 8.5 for comparison), the width does show an overall dependence on the flight distance in the transverse plane, with a deterioration towards high values of such a variable. Also in this case, corresponding to the three SVD layers L3, L4, and L5 there are some structures visible, both in data and MC.

Both Figs. 8.10 and 8.11 hint to the conclusion that the inclusive sample considered here is not entirely suitable for the sideband subtraction approach. Because of its few selection criteria, it is particularly sensitive to the background conditions, and such conditions have proven to be not yet reliable in MC with respect to data (as it will be further explained in the next chapter). In particular,

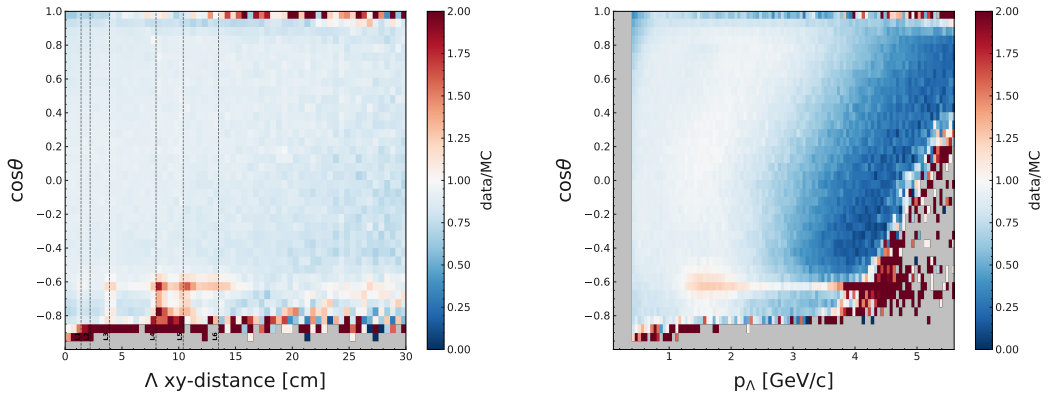

Figure 8.12: 2D data-MC ratio. In the left panel, the ratio is shown as a function of the Λ polar angle (y-axis) and its transverse flight distance (x-axis). In the right panel, the ratio is shown as a function of the Λ polar angle (y-axis) and its momentum (x-axis). Red regions of the panels correspond to areas where there is an excess of data with respect to MC. Blue regions correspond to those where there is a lack of data with respect to MC. White regions correspond to those where the data-MC ratio is close to the unity. The background color of the panels has been set to gray in order to distinguish it from the white regions.

higher background conditions increase the number of tracks, and in the proximity of material the number of vertices. Most of these vertices are badly reconstructed and end up in the sidebands of the Λ mass peak, causing a difference between data and MC which cannot be entirely explained in terms of tracking performance. This can be better understood when looking at 2D data-MC ratio plots. In these plots, red regions of the panels correspond to areas where there is an excess of data with respect to MC. Blue regions correspond to areas where there is a lack of data with respect to MC. White regions correspond to areas where the data-MC ratio is close to the unity. The background color of the panels has been set to gray in order to distinguish it from proper white regions. In the left panel of Fig. 8.12, the ratio between data and MC is shown as a function of the Λ polar angle (y-axis) and its transverse flight distance (x-axis). The position of the six VXD layers is shown as vertical dashed lines. The excess of data with respect to MC is localized at the acceptance limits and at backward angles in proximity of the SVD layers. In the right panel, the ratio between data and MC is shown as a function of the Λ polar angle (y-axis) and its transverse momentum (x-axis). The excess of data with respect to MC at backward angles is not localized along a specific momentum region, even though it seems to be more pronounced at high momentum — where the statistics is poor.

The key information is revealed when looking at the same kind of distri-

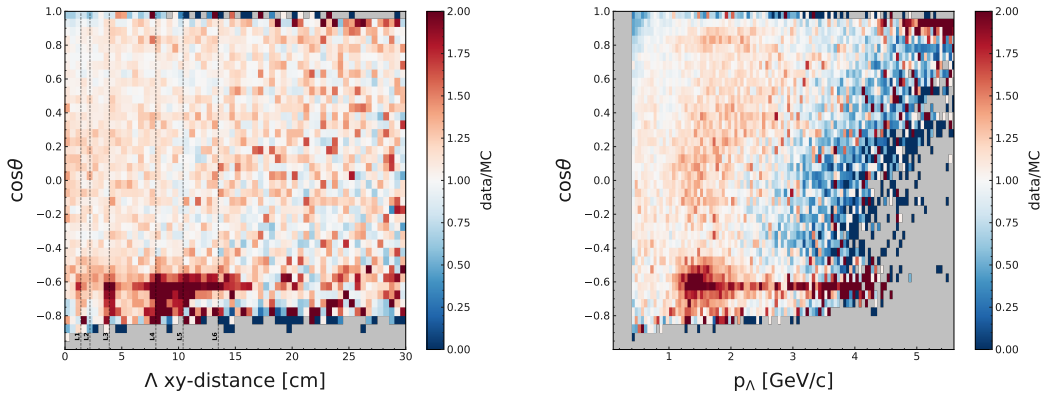

Figure 8.13: 2D data-MC ratio in the sidebands. In the left panel, the ratio is shown as a function of the Λ polar angle (y-axis) and its transverse flight distance (x-axis). In the right panel, the ratio is shown as a function of the Λ polar angle (y-axis) and its momentum (x-axis). Red regions of the panels correspond to areas where there is an excess of data with respect to MC. Blue regions correspond to those where there is a lack of data with respect to MC. White regions correspond to those where the data-MC ratio is close to the unity. The background color of the panels has been set to gray in order to distinguish it from the white regions.

butions, but focusing in the sideband regions only. The resulting picture is shown in Fig. 8.13. Overall, one can notice almost everywhere an excess of data with respect to MC. In particular, the red regions at backward angles observed in Fig. 8.12 are reproduced in Fig. 8.13 as well. On the contrary, when looking at the same distributions but considering the mass region only, there are almost no structures visible, as can be seen in Fig. 8.14. This points to a problem in reproducing the sidebands in MC, and on a deeper level, in reproducing the background conditions in simulation.

In this chapter several limitations of the current simulation have been shown. It has been also shown how the role of background may be a game changer in different ways. The current limitations in the simulation turn out to be especially important when considering inclusive samples, where minimal selection criteria may not be enough to get rid of all contributions not strictly deriving from physics channels. Monitor the background level and improve its simulation is therefore a very important task for the success of the experiment, and many efforts in this direction are ongoing in the collaboration. In particular, recent studies show that including in the simulation more realistic shapes for the collimators greatly improves the agreement of simulated background with data [157]. However, the background simulation and its problems is not the subject of this thesis, so it will not be further discussed here. The next chapter will be dedicated instead

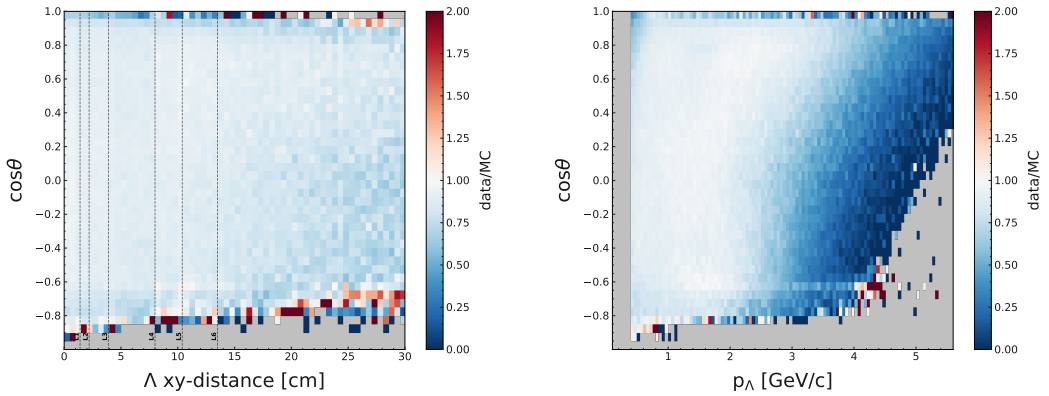

Figure 8.14: 2D data-MC ratio in the mass region. In the left panel, the ratio is shown as a function of the Λ polar angle (y-axis) and its transverse flight distance (x-axis). In the right panel, the ratio is shown as a function of the Λ polar angle (y-axis) and its momentum (x-axis). Red regions of the panels correspond to areas where there is an excess of data with respect to MC. Blue regions correspond to those where there is a lack of data with respect to MC. White regions correspond to those where the data-MC ratio is close to the unity. The background color of the panels has been set to gray in order to distinguish it from the white regions.

to understand how tracking performance is affected by a background level higher than expected with respect to the standard simulation, and how such levels in data could be measured and monitored, in order to provide precise information for its improved simulation in MC.

9 Future challenges

Beam background is a reality that all accelerator-based particle physics experiments have to deal with. It is very important to keep it as low as possible, but it is practically impossible to eliminate it completely. To build a successfully experiment, having a comprehensive knowledge of its beam background is essential, and some of the key factors are having it under control, being able to reliably simulate it, and tune the software algorithms to get the best possible performance.

In the previous chapter it was observed that the background level of the Belle II experiment is currently not well reproduced in the simulation. This chapter will be devoted to elaborate on this statement and give an overview of the current situation. In Section 9.1 it will be shown how this difference can be noticed by monitoring specific variables. In Section 9.2 it will be shown how a worse background affects tracking performance, and Section 9.3 will highlight some of the possible impacts on the hexaquark search.

9.1 Background level in data

In the Belle II experiment, as in every physics experiment, the simulation of the background level is a delicate and very complicated process. The sources of beam background were described in Section 5.1.1. Their correct simulation imply an

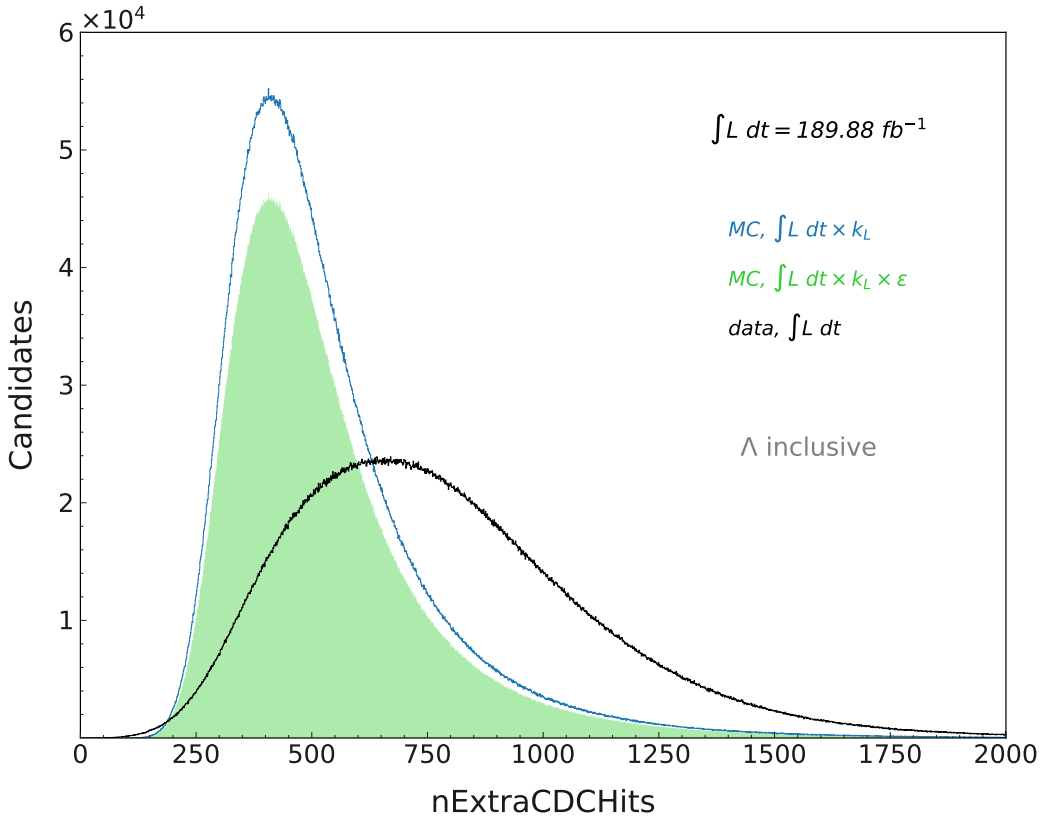

Figure 9.1: Distribution of the event-based variable *nExtraCDCHits*, representing the number of CDC hits not assigned to any track in an event. The blue and green distributions both represent MC, with the two different normalization introduced in Section 8.2. The black histogram represents data. Such a variable is strictly related to the beam background level, and the difference between its distribution in data and MC points to a difference in the beam background conditions for data and MC, in particular to an underestimation of the background level on the simulation side.

in-depth knowledge of the accelerator and beam conditions, and a advanced level of monitoring and control which is very difficult to achieve, particularly in the initial stage of the data taking with a new accelerator. The beam conditions used to simulate the *standard* background level — those used for the studies presented so far in this thesis and labeled as "eph3 BG×1" in Section 5.5 — turned out to be partially inconsistent with the real situation, in particular resulting in an underestimation of the beam background.

An effective way to demonstrate this difference is to compare variables that are dependent on the beam background level in MC and data. In this respect, a notably useful variable is *nExtraCDCHits*, an event-based variable that — event by event — counts the number of CDC hits that are not assigned to any track.

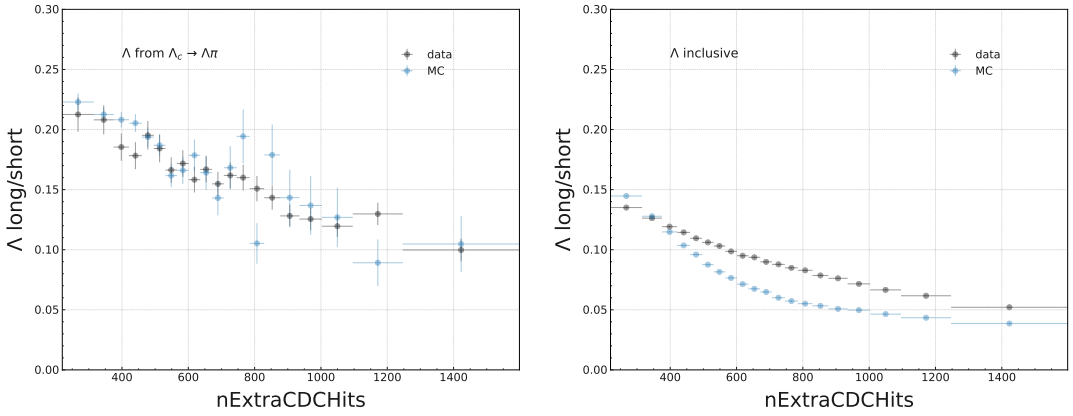

Figure 9.2: Long-short Λ ratio as a function of the number of extra CDC hits in the event. The left panel shows these quantities for Λ coming from the decay $\Lambda_c \to \Lambda\pi$. The right panel shows these quantities for an inclusive Λ sample. The two Λ samples are those introduced in Chapter 8. In both panels, blue points represent the MC sample, while black points represent data.

Intuitively, this variable is strictly related to the background level: in a clean environment there will be no (or few) hits not associated with any track. In contrast, the higher the background level, the higher the value that this variable will assume. Figure 9.1 shows the distribution of the number of extra CDC hits both in data and MC. The samples are the same as introduced and used in the previous chapter when considering the inclusive Λ sample (Section 8.2), and for the MC both normalizations introduced there are shown. The data and MC distributions are extremely different, both in shape and in the peak position, pointing to a difference in the beam background conditions between data and MC. In particular, since the mean value of the distribution is higher in data, the beam background itself is also higher in data than in the simulation.

The same information about background level is carried by Λ baryons (or more generally by displaced vertices), and — to some extent — it can be monitored while performing analyses involving displaced vertices. The way to do so is to divide the V0 signal sample in two categories, *long* V0s and *short* V0s, and then compute the ratio of long to short signal candidates. The definition of these categories is related to the Λ flight distance in the transverse plane, and weather it is before or after the innermost CDC wall. In particular, long candidates are required to have a xy-distance ≥ 15 cm, while short candidates xy-distance < 15 cm. When plotting the long-short ratio as a function of the number of extra CDC hits in the event a dependence between the two variables can be noticed. This is shown in Fig. 9.2 for both Λ samples introduced in the previous chapter.

This dependence can be explained by the assumption that the deterioration in

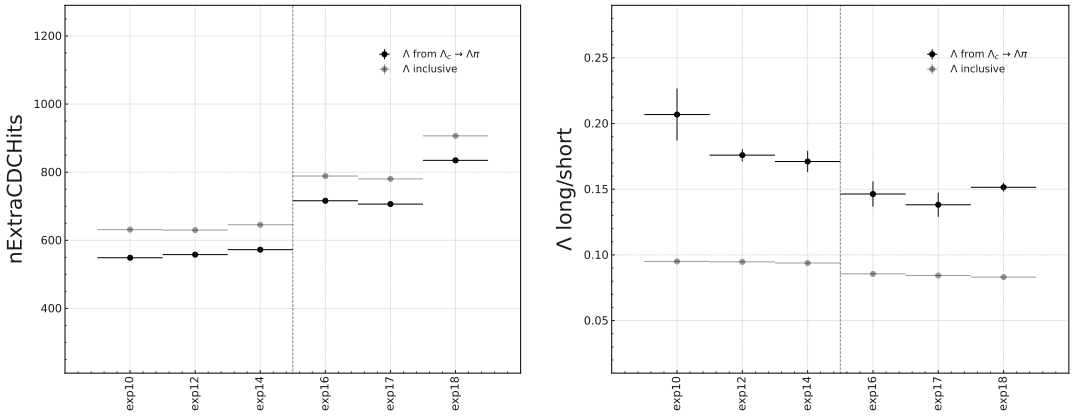

Figure 9.3: Background-dependent variables as a function of the experiment number. The left panel shows the number of extra CDC hits as a function of the experiment number. Each point is obtained as the average number of *nExtraCDCHits* in each experiment. The right panel shows the Λ long-short ratio as a function of the same variable. The ratio is evaluated dividing the total number of long and short Λ obtained after the sidebands subtraction, experiment by experiment. In both panels, black points represent the exclusive Λ sample (Λ from $\Lambda_c \to \Lambda\pi$), while gray points represent the inclusive Λ sample. The vertical dashed line in both panels divides the experiments into two groups, with the left one having generally lower background than the right one.

performance following any background increase is responsible for a degradation of the reconstruction of long V0, i.e. those that decay away from the IP, which are generally more difficult to reconstruct (as shown in the left panel of Fig. 6.3). In the inclusive sample the MC and data points do not have the same distribution, with the ratio decreasing faster in MC. This difference makes it difficult to quantify the background level given the long-short ratio, but it does not preclude the possibility to monitor possible changes over time.

Figure 9.3 shows the two background-dependent variables introduced above as a function of the experiment number, where different experiment numbers represent different data taking periods (higher experiment number corresponds to more recent data). The left panel shows the number of extra CDC hits as a function of the experiment number for both the exclusive and the inclusive Λ samples. The right panel, instead, shows the long-short ratio as a function of the same variable, once again for both the exclusive and the inclusive Λ samples. Given the dependence on the experiment number, no simulation is currently available for these plots[1]. The trend is visible in both panels of Fig. 9.3. In

[1]Run-dependent MC samples, i.e. with luminosity and beam background level extracted from the corresponding data samples, are under preparation and will be available soon. It is known that the background level has fluctuated over time — a lot of tuning took place and is

Table 9.1: MC samples used to evaluate the tracking performance. As for the detector configuration, early (eph3) refers to the missing part of PXD L2, while nominal (nph3) refers to the full PXD installation. The different PXD geometry has a negligible effect on the beam background composition, but the parameters used for the simulation of "BG×1" samples are different between eph3 and nph3. The different beam conditions used to generate the various background sample are summarized in Table B.1.

	Detector configuration	Background rate factor
eph3 BG×0	early	× 0
eph3 BG×1	early	× 1
nph3 BG×1	nominal	× 1
nph3 BG×2	nominal	× 2
nph3 BG×5	nominal	× 5

particular, when comparing the two groups of three experiments each (left and right of the dashed line), it can be seen that exp10, exp12, and exp14 have a generally lower background (i.e. lower number of extra CDC hits) compared to exp16, exp17, and exp18. Consistently, the first group of experiments has a higher long-short ratio compared to the latter one, thus pointing to the same conclusions (being the two variables inversely proportional). This confirms the assumption that, to some extent, the background level can be monitored using displaced vertices, although its precise assessment with this technique is challenging and anyway not possible without run-dependent MC samples.

9.2 Tracking performance in high background scenarios

As already mentioned, the background simulation is a very complicated process. Considerable effort within the collaboration is currently devoted to this task, but this goes beyond the scope of this thesis. What is important for the purposes of this dissertation is the impact that a higher background level (with respect to the one originally considered, eph3 BG×1) can have on tracking performance and consequently on the hexaquark analysis. This can be estimated by simulating different levels of beam background and study the reconstruction performance. In particular, for the studies presented in this section, five different MC sam-

still ongoing from the accelerator side, in order to find the best machine conditions.

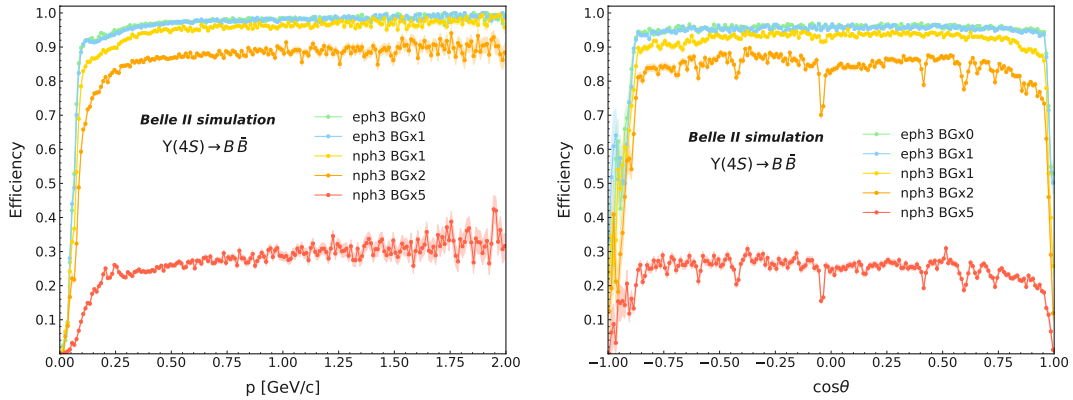

Figure 9.4: Tracking efficiency for different beam background conditions. The panel on the left shows the efficiency as a function of the particle momentum, while the panel on the right shows the efficiency as a function of the particle polar angle. The definition of efficiency is given in Eq. (5.1). The legend is explained in Table 9.1.

ples were used which are summarized in Table 9.1. The two samples labeled as "eph3 BG×1" and "nph3 BG×1" differ in two aspects: the PXD-related geometry and the beam conditions used in the simulation (despite being both labelled as "BG×1"). As for the geometry, "eph3" stands for "early" and refers to the missing part of PXD L2, while "nph3" stands for "nominal" and refers to the full PXD installation (see Section 4.1.2 for more details). The PXD geometry has a negligible impact on tracking, and the different performance is driven by the parameters used in the background simulation. A detailed list of the beam conditions used to generate the different backgrounds can be found in Table B.1. For each of the MC samples a total of 2×10^5 events were generated: 10^5 $\Upsilon(4S) \to B^+B^-$ events and 10^5 $\Upsilon(4S) \to B^0\bar{B}^0$ events. The uncertainties represented in the plots arise from statistics only.

Figure 9.4 shows the tracking efficiency, both as a function of the particle momentum (left panel) and polar angle (right panel), for the different MC samples. These are the same kind of plots introduced in Section 5.5, with the definition of efficiency given in Eq. (5.1). The average efficiency depends clearly on the beam background level. In general it is higher than 80% for all but the sample with extreme beam background conditions (nph3 BG×5), where the efficiency drops to ∼30%.

Figure 9.5 shows the tracking purity, clone, and fake rates for the three samples with higher beam background conditions: nph3 BG×1, nph3 BG×2, and nph3 BG×5 from top to bottom row, respectively. In each row these quantities, whose

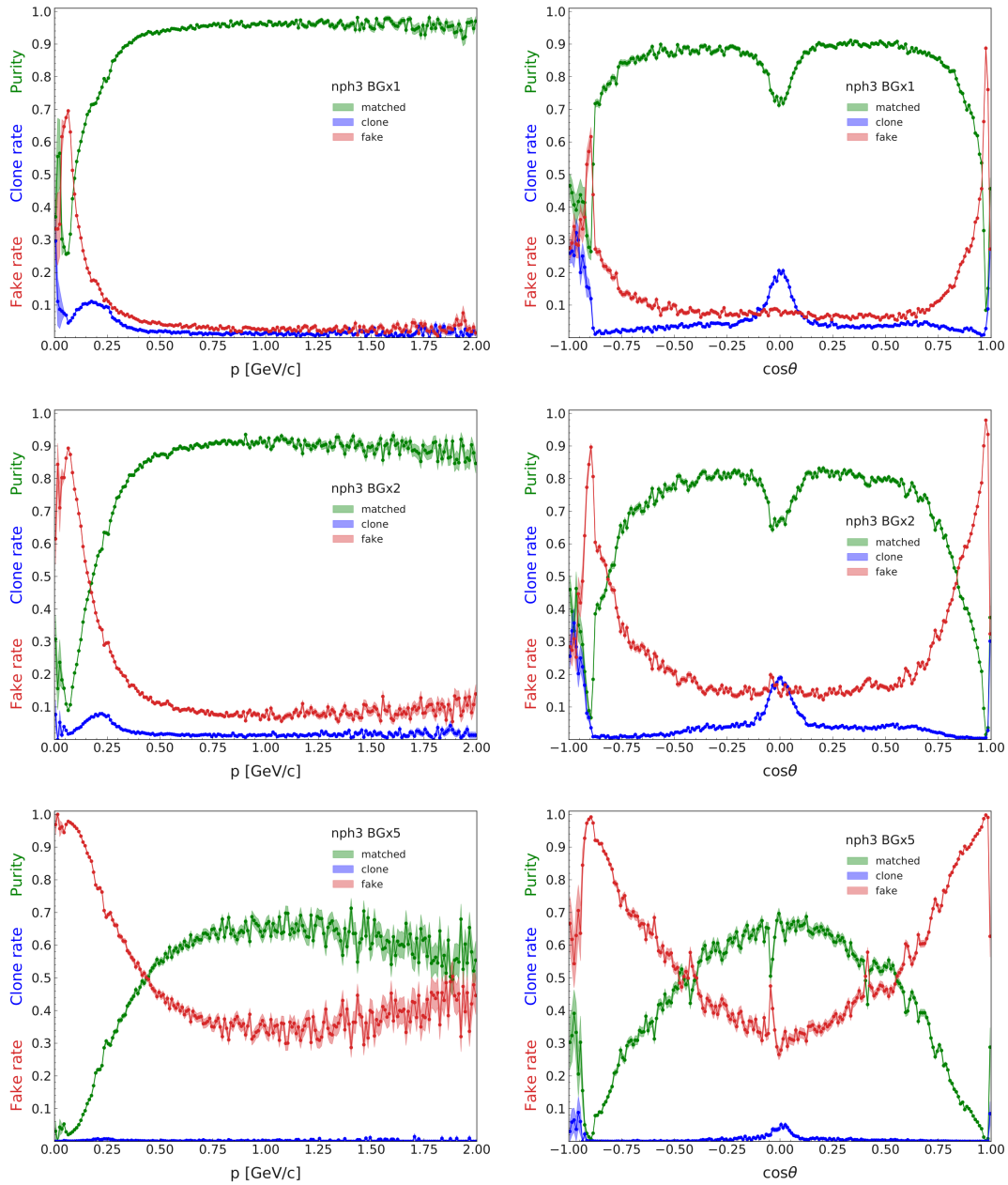

Figure 9.5: Tracking purity (matched), clone rate, and fake rate for different background conditions. In the first row the sample nph3 BG×1 is shown. In the second row the sample nph3 BG×2 is shown. In the third row the sample nph3 BG×5 is shown. The left column shows the quantities as a function of the particle momentum, while the right column shows them as a function of the particle polar angle. Purity, clone rate, and fake rate definitions are given in Eqs. (5.2) to (5.4), respectively.

Table 9.2: Average tracking performance evaluated using the five MC samples with different background conditions introduced in Table 9.1.

	efficiency (%)	purity (%)	clone rate (%)	fake rate (%)
eph3 BG×0	95.48 ± 0.03	91.38 ± 0.04	5.88 ± 0.03	2.74 ± 0.02
eph3 BG×1	95.09 ± 0.03	90.87 ± 0.04	5.52 ± 0.03	3.61 ± 0.03
nph3 BG×1	92.16 ± 0.04	82.40 ± 0.05	4.62 ± 0.03	12.97 ± 0.05
nph3 BG×2	83.50 ± 0.06	62.48 ± 0.06	3.34 ± 0.02	34.17 ± 0.06
nph3 BG×5	24.60 ± 0.07	25.92 ± 0.07	0.25 ± 0.01	73.83 ± 0.07

definitions were given in Eqs. (5.2) to (5.4), are plotted as a function of the particle momentum (left column) and polar angle (right column). The same distributions for the early background condition (eph3 BG×1) were shown in Fig. 5.6. As it can be seen from Fig. 9.5, when focusing on the panels of one of the two columns, the same structures are present, just more pronounced moving from top to bottom. The clone and fake rates are higher at low momentum, as opposed to the purity. The enhancement (drop) in the clone rate (purity) — already noticed in Fig. 5.6 — is visible for $\cos\theta \sim 0$ (right column), which is the direction perpendicular to the beam.

The average values of efficiency, purity, clone, and fake rate, integrated over the whole momentum and angle ranges, are summarized in Table 9.2 for the five MC samples. The highest background scenario considered here, nph3 BG×5, is of course a very extreme condition, but it provides important information. In case it were to become reality the performance would deteriorate too much, and a modification of the tracking algorithms will be needed. Preliminary studies showed that a different order in the tracking chain (i.e. executing the SVD standalone track finding before the CDC standalone track finding) would already improve the performance in case of high background, but this needs to be further studied.

9.3 Background impact on the hexaquark search

In Section 9.1 it was shown how, with the current conditions, the standard beam background level (eph3 BG×1) is underestimated in simulation. As a rough estimate, the current background level is somewhere between the eph3 BG×1 and nph3 BG×1 cases. To date, repeating the entire hexaquark analysis with a different MC is not a priority. Once a decision will be made on data taking at the

energy of the $\Upsilon(3S)$ resonance, the choice of the correct sample will be crucial, and the analysis will be repeated with better tuned MC. The purpose of this section is to highlight some of the possible consequences of a higher background level, and to give initial hints about possible opportunities for improvement. For these studies only the MC sample nph3 BG×1 has been used. As already mentioned, this represents a slight overestimation of the current beam background level as found in the data. Also, the study was performed only on the channel without pions in the final state, $\Upsilon(3S) \to \Lambda\Lambda$.

Figure 9.6 shows the comparison between the pre-selection signal efficiency in standard (eph3 BG×1, left panel) and higher (nph3 BG×1, right panel) background conditions, as a function of the generated hexaquark mass squared M_S^2. In this case the efficiency is computed before applying any selection to the signal sample [2], simply dividing the number of MC-matched reconstructed events by the number of generated hexaquark events. In the higher beam background scenario the overall pre-selection efficiency drops from ∼12% to ∼4%, making the analysis more challenging.

For some parts of the analysis it is practically impossible to make predictions that can be useful without precise information on the background level and a reliable simulation. This is the case, for example, for the ROE selection, whose variables strongly depend on it. In this case it will be necessary to check the selection criteria and, in case, to re-optimize them once the dataset relevant for the analysis and the corresponding MC will be available. The need for checking and validating cuts and selections with the final dataset is a true statement in general, but for specific parts of this analysis it is possible to provide qualitative information even in the absence of precise knowledge of the background. One prominent example is the BC selection (introduced in Section 7.2.2). A better variable in such a scenario is *max* nHits, namely the maximum number of hits, defined as:

$$\begin{aligned} max\,\mathrm{nHits} &= max\Big\{ \sum_{i=1}^{4} \mathrm{nHits}_i \Big\}, \\ \mathrm{nHits}_i &= \mathrm{nCDCHits}_i + \mathrm{nSVDHits}_i. \end{aligned} \tag{9.1}$$

The index i runs over the four charged tracks coming from the two Λ baryons of the event. Figure 9.7 shows the efficiency of the BC selection as a function of the generated hexaquark mass, both for the standard background scenario (eph3 BG×1, left panel) and the higher background scenario (nph3 BG×1, right panel). In each panel are represented the two BC variables $best\Lambda_s$ (defined in Eq. (7.6))

[2] Note that this is different from what was shown in Fig. 7.16, where the curves were obtained after applying the analysis selections.

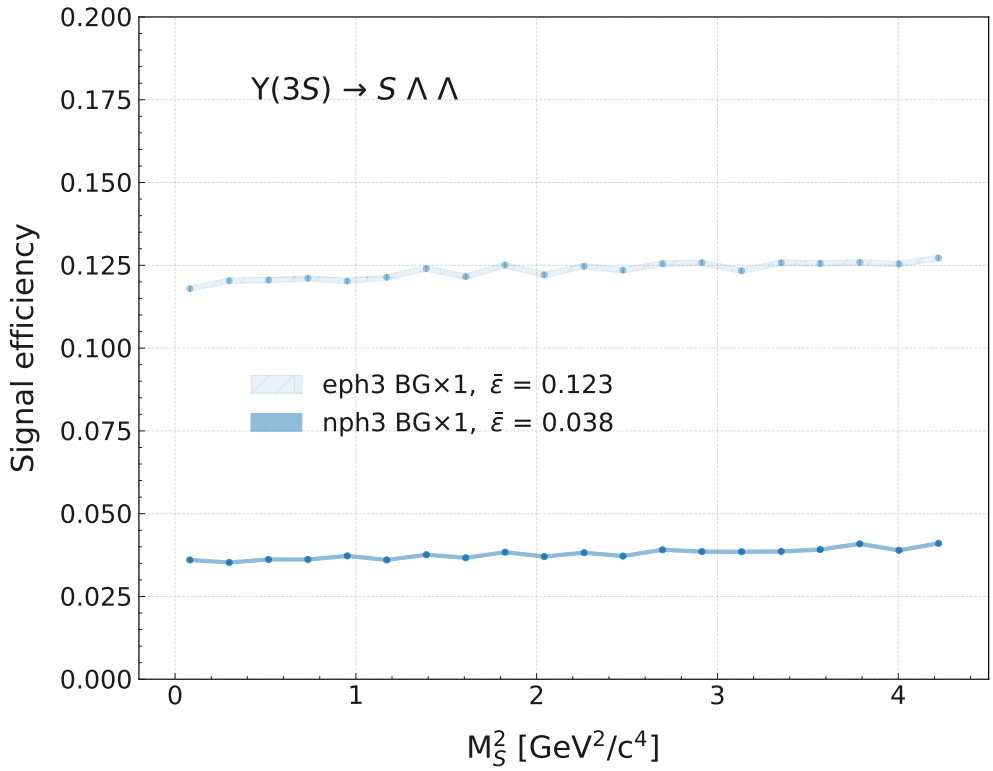

Figure 9.6: Hexaquark signal efficiency as a function of the generated hexaquark squared mass M_S^2 in two different background scenarios: standard background (eph3 BG×1) and higher background level (nph3 BG×1). The respective mean values, integrated over the mass range, are reported on each panel.

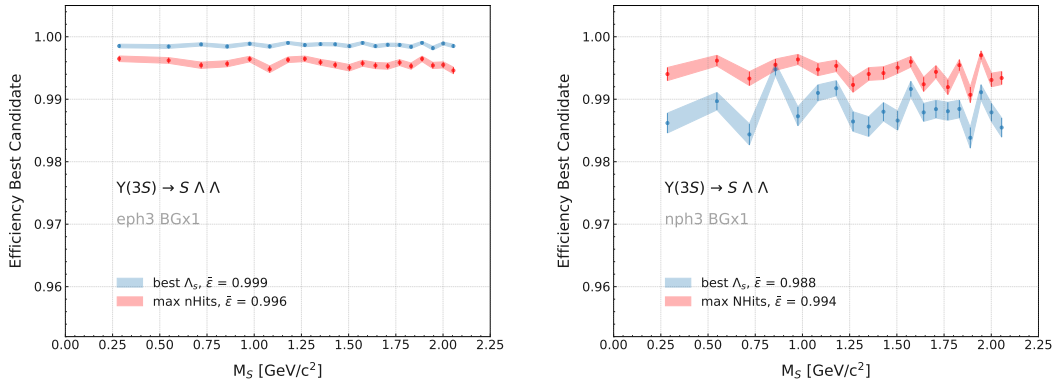

Figure 9.7: Efficiency of the BC selection as a function of the generated hexaquark mass in different background scenarios. The left panel shows the BC efficiency in the standard background scenario (eph3 BG×1), while the right panel shows it in a higher background scenario (nph3 BG×1). The definition of BC efficiency is given in Eq. (7.7). In both panels two BC variables are plotted, $best\Lambda_s$ (see Eq. (7.6)) and *max* nHits (see Eq. (9.1)).

and *max* nHits (defined in Eq. (9.1)). The definition of BC efficiency is given in Eq. (7.7). From the figure one can notice how the BC efficiency is very high in all cases (above ∼98%). However, while in the standard background conditions a selection on $best\Lambda_s$ outperforms with respect to *max* nHits, the situation is the opposite in higher background conditions, where a BC selection on *max* nHits performs better. The gain is not huge, but it is worth monitoring both variables and deciding on the best performance, especially in the case of high background.

Finally, one can estimate the possible effect of the background degradation on the final UL calculation. In order to get to a qualitative estimate without repeating the whole analysis one needs to make some assumptions. The signal efficiency $\epsilon_S(M_S)$ entering in Eq. (7.12) can be thought of as the product between the channel reconstruction efficiency and the selection efficiency, $\epsilon_S = \epsilon_{re} \times \epsilon_{se}$. The first term is exactly the signal efficiency we derived earlier in the section, $\epsilon_{re} = 0.038$ (see Fig. 9.6, nph3 BG×1). Two distinct UL were computed, starting from two different assumptions for ϵ_{se}. In the first scenario $\epsilon_{se,1}$ is assumed to be exactly 1, i.e. the selection efficiency is assumed to be perfect, capable of retaining all the signal events and cutting out all background. This assumption leads to a signal efficiency $\epsilon_{S,1} = 0.038$. Despite being too optimistic, this case provides an insight into the impact of the background on the UL by removing any effects due to further analysis steps. In the second scenario the selection efficiency is assumed to be the same as that resulting from the hexaquark analysis described in Chapter 7, $\epsilon_{se,2} = 0.585$. This assumption leads to a signal efficiency $\epsilon_{S,2} = 0.022$. Both $\epsilon_{S,1}$ and $\epsilon_{S,2}$ were assumed to be independent from the generated hexaquark mass. Furthermore, it was assumed not to find any background events in the signal region, which translates into setting F equal to 0 in Eq. (7.12). Figure 9.8 shows the UL estimation for these two cases, as well as the results obtained in Section 7.3 assuming early background conditions (eph3 BG×1). In the left panel the UL estimation is shown as a function of the hexaquark mass, with CL=90%. In the right panel the UL estimation is shown as a function of the integrated luminosity, again with CL=90%. The horizontal lines on the plot represent the limits put by the BaBar collaboration on the same channel [112], and the intersections of the curves with those give an indication of the necessary luminosity to be collected in order for the Belle II experiment to be competitive with the existing analysis. The data taking plan at the $\Upsilon(3S)$ resonance is to collect a dataset larger than 200 fb^{-1} [124], thus making this channel competitive also in such a higher background scenario.

Comparing the new results (solid and dashed lines) to those obtained with

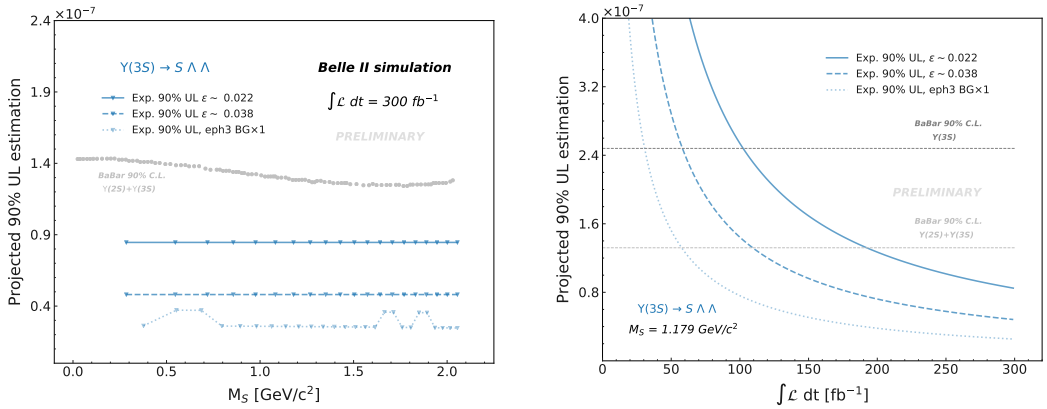

Figure 9.8: UL estimation in a higher background scenarios. In the left panel the estimation is plotted as a function of the hexaquark mass M_S. In the right panel the UL estimation is shown as a function of the integrated luminosity. Here the two horizontal lines represent the existing limits set by the BaBar collaboration on the same channel [112]. The solid and the dashed lines in each plot represent two different starting assumptions about the signal efficiency ϵ_S. The dotted curve shows the result obtained in Section 7.3 with early background conditions (eph3 BG×1). In all cases CL=90%. A description of the method used to derive the limits can be found in Section 7.3.

early background conditions (eph3 BG×1, dotted line) one can notice the severe impact that beam background can have on this analysis. In the best case scenario, assuming a perfect selection ($\epsilon_{se} = 1$), the UL value increases by a factor ∼1.7 with respect to the complete analysis, going from the original 2.8×10^{-8} to 4.8×10^{-8}. In the second more realistic scenario considered, with ϵ_{se}=0.585, the UL mean value increases by a factor ∼3, becoming 8.5×10^{-8}. This deterioration in performance naturally drives a requirement on the necessary statistics to be collected at the $\Upsilon(3S)$ resonance in order for the Belle II experiment to reach the existing limits from the BaBar collaboration: the luminosity required increases from $\int \mathcal{L}dt \sim 50$ fb^{-1} to ∼100-200 fb^{-1}, depending on the considered scenario. The Belle II plan of collecting a dataset larger than 200 fb^{-1} at the $\Upsilon(3S)$ resonance [124] would ensure the competitiveness of the analysis even in the worst-case background scenario here considered.

E quindi uscimmo a riveder le stelle.

(Thence we came forth to rebehold the stars.)

Dante Alighieri

10 Summary

This thesis presents a sensitivity study for the future search for a stable six-quark state S with the Belle II experiment considering a hexaquark mass range $0 < M_S < 2.055\ \mathrm{GeV/c^2}$. The search for a double strange state is particularly well suited at narrow $b\bar{b}$ resonances — $\Upsilon(nS)$ with $n \leq 3$ — because of their prominent decay channel in three gluons thus producing $s\bar{s}$ pairs with roughly the same probability as $u\bar{u}$ and $d\bar{d}$ pairs. The Belle II experiment started collecting data in 2019, and so far almost all data were collected at the $\Upsilon(4S)$ resonance, with no data collected at narrow resonances yet. In preparation for such a measurement, the thesis focuses on improving the Belle II reconstruction algorithms for displaced vertices and on in-depth work on Λ baryons, from the optimization of their reconstruction to the evaluation of the performance, both using MC and the available $\Upsilon(4S)$ data. The most considerable part of the work has been devoted to the subsequent sensitivity studies for the search for a double strange six quark state using the improved tools.

For the sensitivity analysis the S hexaquark was assumed to be produced in $\Upsilon(3S)$ decays together with a pair of Λ baryons: $\Upsilon(3S) \to S\,\Lambda\,\Lambda\,n\pi$. A total of five channels was considered, that differ from each other in the number of additional pions produced in the final state (n = 0, 2, 4, 6, or 8). The event selection was optimized via the maximization of the Punzi FOM using a $\Upsilon(3S)$

MC sample. A set of ULs was extracted and they represent the main result of the thesis (Figs. 7.18 and 7.19). When collecting an integrated luminosity of $\int \mathcal{L}dt = 300$ fb^{-1} at the $\Upsilon(3S)$ resonance, the existing UL — a result from the BaBar collaboration based on the final state with n=0 [112] — could be improved by a factor of ∼5, moving from the current (1.2-1.4) $\times$ 10^{-7} to 2.8 $\times$ 10^{-8}. The minimum luminosity to be collected at the $\Upsilon(3S)$ resonance in order to reach the limit set by BaBar corresponds to $\int \mathcal{L}dt \sim 50$ fb^{-1}. For the channels with additional pions in the final state there are no existing ULs, and therefore a future Belle II result would represent a novel measurement. The final part of the thesis was devoted to critically review the sensitivity study in light of the difficulties being experienced in terms of beam background level by the Belle II experiment. Even if the current goal of the collaboration is to be able to better understand the accelerator and to reduce the background via fine tuning of the machine parameters, a few sets of ULs were estimated for less favorable scenarios (Fig. 9.8). As expected the performance deteriorates, and when collecting an integrated luminosity of $\int \mathcal{L}dt = 300$ fb^{-1} the UL moves somewhere around (4.8-8.5) $\times$ 10^{-8}, depending on the initial assumptions. In this case the minimum luminosity to be collected in order to reach the limit set by BaBar corresponds to $\int \mathcal{L}dt \sim$ 100-200 fb^{-1}. However, these estimates are rather qualitative and a more critical review has to be done once the dataset will be collected and the actual background conditions will be known. This work is intended to pave the way for a future measurement, and the tools and analysis procedures developed, as well as the critical points observed, to be used on the collected $\Upsilon(3S)$ data to set world-leading ULs on the possible observation of a stable, double strange six-quark state.

A

Helix coordinates VS Cartesian coordinates

The Belle II helix representation is based on five parameters h_5, whose definitions are given in Chapter 5:

$$h_5 = (d_0, z_0, \phi_0, \omega, tan\lambda). \tag{A.1}$$

Six coordinates c_6 are commonly used to describe a trajectory in the cartesian system:

$$c_6 = (x, y, z, p_x, p_y, p_z). \tag{A.2}$$

c_6 can be expressed in terms of h_5 as following:

$$c_6 = \mathcal{F}(h_5),\ \mathcal{F} : \mathbb{R}^5 \rightarrow \mathbb{R}^6 : \begin{cases} x = +d_0\, sin\phi_0 \\ y = -d_0\, cos\phi_0 \\ z = z_0 \\ p_x = \frac{qB_z}{\omega}\, cos\phi_0 \\ p_y = \frac{qB_z}{\omega}\, sin\phi_0 \\ p_z = \frac{qB_z}{\omega}\, tan\lambda \end{cases} . \tag{A.3}$$

B

Tracking performances, additional material

B.1 Beam conditions for background simulation

Table B.1: Beam conditions used to simulate the beam background. The beam background samples are provided to the user by the Belle II data production group.

	eph3 LER (e^+) / HER (e^-)	nph3 LER (e^+) / HER (e^-)
Beam current [A]	1.2 / 1.0	3.6 / 2.6
Number of bunches	1576 / 1576	2500 / 2500
Bunch current [A]	0.761 / 0.635	1.44 / 1.04
Vertical beam size	37.3 / 35.7	23.9 / 9.4
Emittance ratio	0.01 / 001	0.0027 / 0.0028
Coulomb IR losses [MHz]	56.84 / 4.85	191.64 / 49.78
Brems IR losses [MHz]	4.78 / 0.53	8.29 / 4.28
Touschek IR losses [MHz]	32.29 / 29.17	119.41 / 1686.07
Coulomb lifetime [min]	26 / 266	19.06 / 37.21
Brems lifetime [min]	1525 / 7552	2929.74 / 2556.38
Touschek lifetime [min]	7 / 59	7.18 / 15.77

B.2 Track fitting with different hypotheses

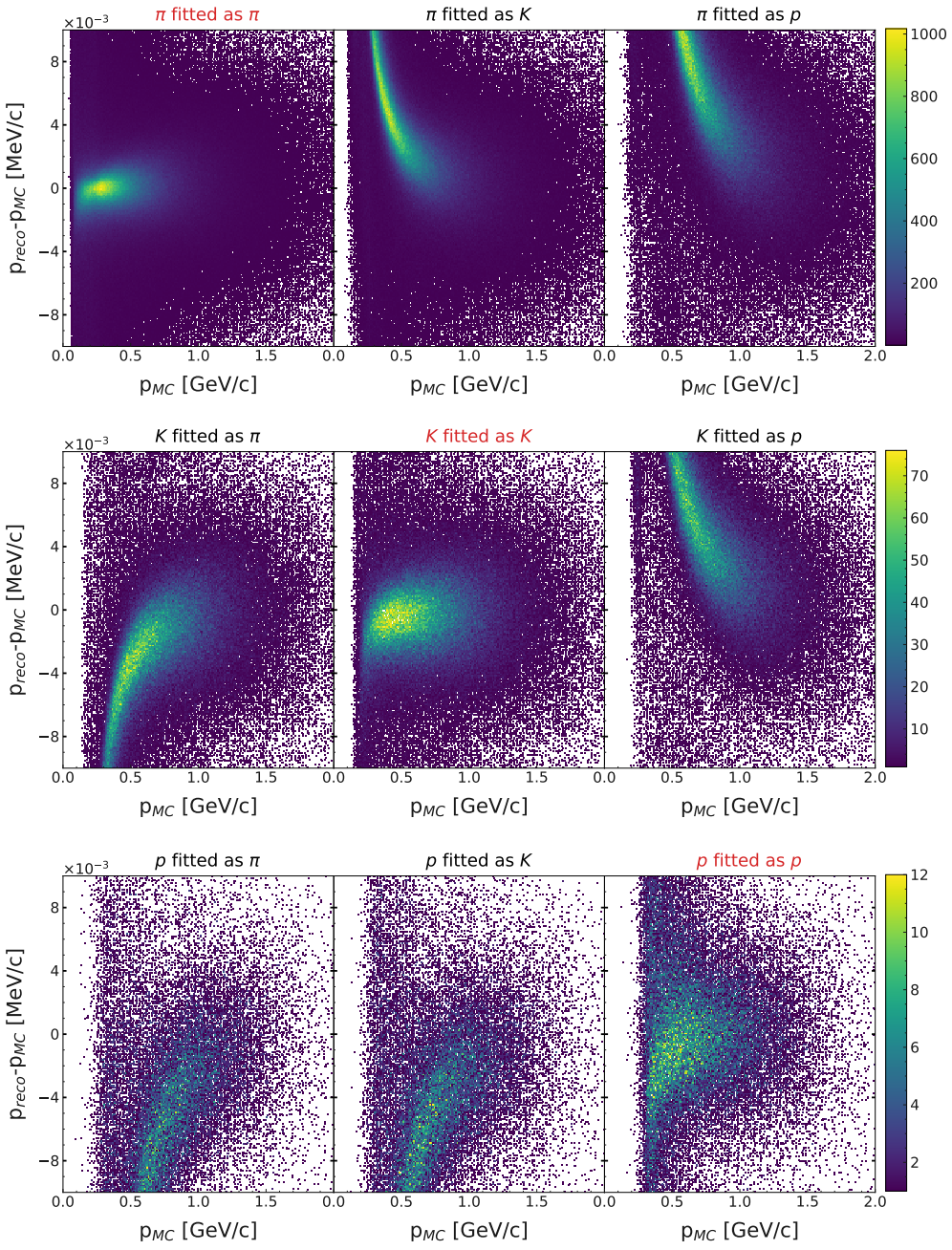

Figure B.1: Momentum dependence of tracks fitted with different hypotheses. As it can be inferred by the figure, using the correct particle hypothesis (top-left to bottom-right diagonal set of panels, with red titles) helps in improving the momentum resolution especially at low momentum.

C

2D FOM for Λ selection optimization

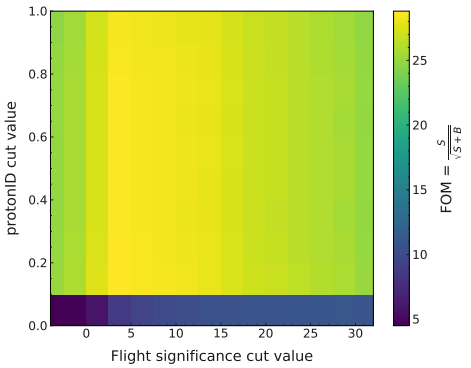

$0.0 < p_\Lambda < 0.4$ GeV/c

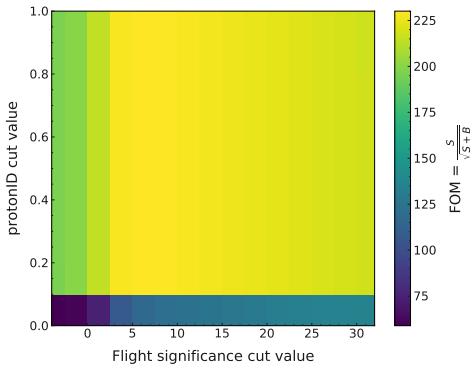

$0.4 < p_\Lambda < 1.0$ GeV/c

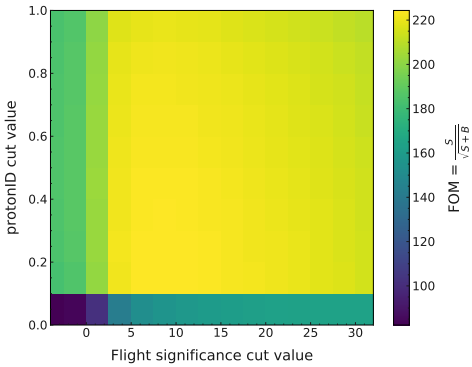

$1.0 < p_\Lambda < 1.5$ GeV/c

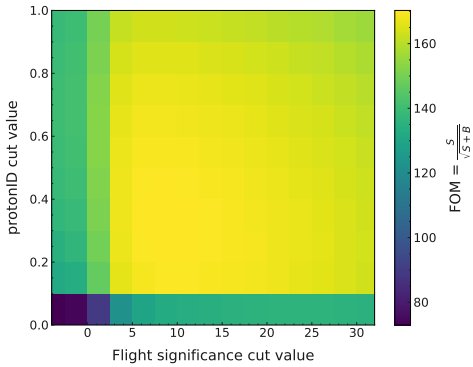

$1.5 < p_\Lambda < 2.0$ GeV/c

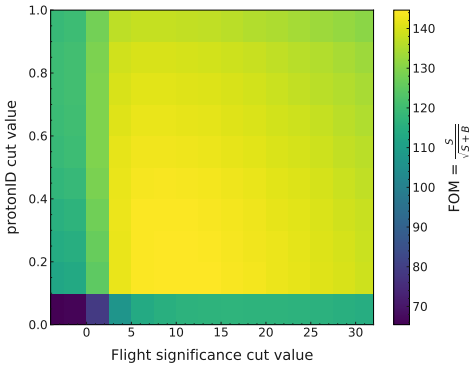

$3.0 < p_\Lambda < 2.0$ GeV/c

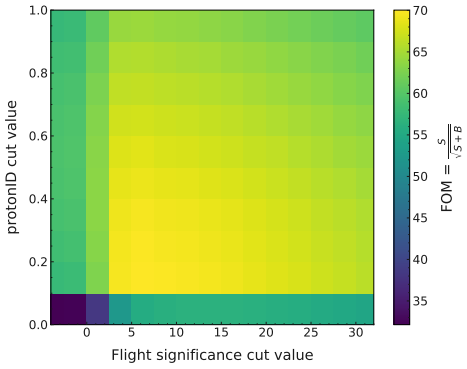

$3.0 < p_\Lambda < 4.0$ GeV/c

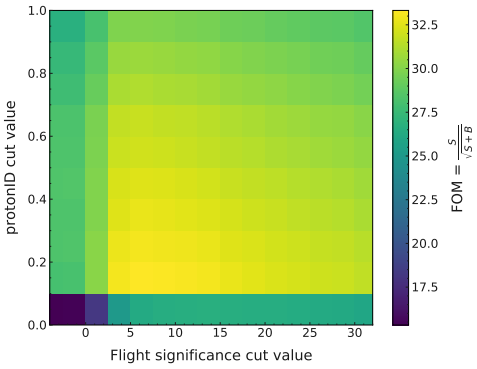

$4.0 < p_\Lambda < 6.0$ GeV/c

Figure C.1: 2D FOM computation for all the seven Λ momentum bins defined in Eq. (6.2). The definition of the FOM is given in Eq. (6.3). On the x-axis the lower cut values assigned to the Λ flight significance are shown, while on the y-axis the lower cut values assigned to the protonID are shown. The z-axis represents the computed FOM values. Blue regions have lower FOM, yellow regions have higher FOM.

D

Stable hexaquark, MC samples

D.1 Background MC

Table D.1: Summary of the official Belle II MC sample used as background for the stable hexaquark analysis. The sample is equivalent to a luminosity $\mathcal{L} = 300\ fb^{-1}$.

Mode	**MC Campaign**	**prodID**	**Events** [$\times$ $\mathbf{10^6}$]
generic	MC13a	15054	1200.00
uubar	MC13a	13266	504.22
ddbar	MC13a	13268	125.27
ssbar	MC13a	13270	119.00
ccbar	MC13a	13272	407.13

D.2 Preliminary signal MC

Table D.2: Fit results obtained with the preliminary $\Upsilon(3S) \to S\,\bar{\Lambda}\,\bar{\Lambda}$ MC samples.

$\Upsilon(3S) \to S\,\bar{\Lambda}\,\bar{\Lambda}$				
M_S [GeV/c^2]	μ [GeV^2/c^4]	ω[GeV^2/c^4]	N	0.5 $\times$ FWHM
0.4	0.161 $\pm$ 0.002	0.446 $\pm$ 0.004	36.241 $\pm$ 0.438	0.223 $\pm$ 0.002
1.6	2.560 $\pm$ 0.002	0.464 $\pm$ 0.004	38.416 $\pm$ 0.453	0.232 $\pm$ 0.002
2.2	4.223 $\pm$ 0.002	0.452 $\pm$ 0.004	37.655 $\pm$ 0.442	0.226 $\pm$ 0.002

Table D.3: Fit results obtained with the preliminary $\Upsilon(3S) \to S\,\Lambda\,\Lambda$ MC samples.

$\Upsilon(3S) \to S\,\Lambda\,\Lambda$				
M_S [GeV/c^2]	μ [GeV^2/c^4]	ω [GeV^2/c^4]	N	0.5 × FWHM
0.2	0.036 ± 0.002	0.444 ± 0.004	35.844 ± 0.438	0.222 ± 0.002
0.3	0.083 ± 0.002	0.435 ± 0.004	35.283 ± 0.427	0.218 ± 0.002
0.4	0.157 ± 0.002	0.439 ± 0.004	35.417 ± 0.430	0.220 ± 0.002
0.5	0.245 ± 0.002	0.448 ± 0.004	36.402 ± 0.446	0.224 ± 0.002
0.6	0.354 ± 0.002	0.441 ± 0.004	35.489 ± 0.428	0.221 ± 0.002
0.7	0.487 ± 0.002	0.442 ± 0.004	35.828 ± 0.433	0.221 ± 0.002
0.8	0.637 ± 0.002	0.455 ± 0.004	37.141 ± 0.447	0.227 ± 0.002
0.9	0.805 ± 0.002	0.450 ± 0.004	36.781 ± 0.447	0.225 ± 0.002
1.0	0.993 ± 0.002	0.448 ± 0.004	36.316 ± 0.440	0.224 ± 0.002
1.1	1.208 ± 0.002	0.456 ± 0.004	37.428 ± 0.447	0.228 ± 0.002
1.2	1.433 ± 0.002	0.460 ± 0.004	37.923 ± 0.452	0.230 ± 0.002
1.3	1.684 ± 0.002	0.451 ± 0.004	36.568 ± 0.442	0.226 ± 0.002
1.4	1.956 ± 0.002	0.447 ± 0.004	36.760 ± 0.441	0.223 ± 0.002
1.5	2.249 ± 0.002	0.452 ± 0.004	37.450 ± 0.441	0.226 ± 0.002
1.6	2.553 ± 0.002	0.447 ± 0.004	36.746 ± 0.454	0.224 ± 0.002
1.7	2.886 ± 0.002	0.455 ± 0.004	37.713 ± 0.444	0.227 ± 0.002
1.8	3.236 ± 0.002	0.455 ± 0.004	37.737 ± 0.448	0.227 ± 0.002
1.9	3.609 ± 0.002	0.440 ± 0.004	36.733 ± 0.432	0.220 ± 0.002
2.0	3.997 ± 0.002	0.444 ± 0.004	36.922 ± 0.434	0.222 ± 0.002
2.1	4.405 ± 0.002	0.439 ± 0.004	36.342 ± 0.430	0.219 ± 0.002
2.2	4.405 ± 0.002	0.444 ± 0.004	36.869 ± 0.434	0.222 ± 0.002

D.3 Checks with 2π sample

Table D.4: Number of events before and after the track-based requirements on the additional π_s, both for correctly (*signal*) and wrongly (*bkg*) reconstructed signal events, for all the generated hexaquark masses. In this case, the channel considered is $\Upsilon(3S) \to S\,\Lambda\,\Lambda\,\pi^+\pi^-$.

$\Upsilon(3S) \to S\,\Lambda\,\Lambda\,\pi^+\pi^-$						
M_S [GeV/C^2]	# signal before	# signal after	% signal left	# bkg before	# bkg after	% bkg left
0.285	5772	5455	0.95	4857	1582	0.33
0.547	5609	5284	0.94	4899	1612	0.33
0.719	5732	5348	0.93	4590	1424	0.31
0.857	5707	5410	0.95	4615	1507	0.33
0.976	5723	5388	0.94	4606	1501	0.33
1.082	5573	5274	0.95	4783	1596	0.33
1.179	5572	5251	0.94	4759	1551	0.33
1.268	5717	5393	0.94	5156	1745	0.34
1.351	5601	5229	0.93	4680	1544	0.33
1.429	5692	5309	0.93	4474	1343	0.3
1.504	5705	5346	0.94	5132	1689	0.33
1.574	5490	5174	0.94	4741	1437	0.3
1.642	5570	5224	0.94	4707	1446	0.31
1.707	5639	5294	0.94	4718	1497	0.32
1.77	5538	5173	0.93	4668	1510	0.32
1.831	5666	5299	0.94	4523	1383	0.31
1.889	5593	5261	0.94	4835	1499	0.31
1.946	5653	5257	0.93	5192	1741	0.34
2.001	5548	5220	0.94	4835	1488	0.31
2.055	5452	5093	0.93	4505	1491	0.33

Table D.5: Number of events before and after the track-based requirements on the additional π_s, both for correctly (*signal*) and wrongly (*bkg*) reconstructed signal events, for all the generated hexaquark masses. In this case, the channel considered is $\Upsilon(3S) \to S\,\bar{\Lambda}\,\bar{\Lambda}\,\pi^+\pi^-$.

$\Upsilon(3S) \to S\,\bar{\Lambda}\,\bar{\Lambda}\,\pi^+\pi^-$						
M_S [GeV/C^2]	# signal before	# signal after	% signal left	# bkg before	# bkg after	% bkg left
0.285	4966	4691	0.94	4502	1261	0.28
0.547	4908	4631	0.94	4523	1304	0.29
0.719	5008	4737	0.95	4763	1290	0.27
0.857	4983	4726	0.95	4543	1295	0.29
0.976	4921	4613	0.94	4752	1241	0.26
1.082	4860	4559	0.94	4591	1206	0.26
1.179	4940	4670	0.95	4659	1214	0.26
1.268	4844	4542	0.94	4720	1243	0.26
1.351	4825	4549	0.94	5041	1412	0.28
1.429	4864	4578	0.94	4958	1321	0.27
1.504	4795	4502	0.94	4612	1265	0.27
1.574	4863	4613	0.95	4806	1292	0.27
1.642	4926	4640	0.94	4628	1239	0.27
1.707	4791	4490	0.94	4636	1221	0.26
1.77	4895	4594	0.94	4535	1260	0.28
1.831	4891	4536	0.93	4715	1262	0.27
1.889	4868	4586	0.94	5117	1442	0.28
1.946	4913	4611	0.94	5207	1387	0.27
2.001	4881	4559	0.93	4580	1170	0.26
2.055	4823	4475	0.93	4970	1337	0.27

E

Λ samples, additional information

E.1 Λ from $\Lambda_c^+ \to \Lambda^0\pi^+$

The fit function for the Λ_c mass peak is define as a double Gaussian (f_a) + first order polynomial (f_b):

$$f_a = N\left(f\,\frac{e^{\frac{-(x-\mu_1)^2}{2\sigma_1^2}}}{\sigma_1\sqrt{2\pi}} + (1-f)\,\frac{e^{\frac{-(x-\mu_2)^2}{2\sigma_2^2}}}{\sigma_2\sqrt{2\pi}}\right), \tag{E.1}$$

with

$$\mu_2 = \mu_1 + \Delta\mu; \tag{E.2}$$

$$\sigma_2 = \sqrt{\sigma_1^2 + \sigma_{tail}^2}; \tag{E.3}$$

$$f_b = a + bx. \tag{E.4}$$

The σ_c used to defined signal region and sidebands is the sum in quadrature of the two σ:

$$\sigma_c = \sqrt{\sigma_1^2 + \sigma_2^2} \tag{E.5}$$

The results from the fit to both MC and data are reported in the table below.

Table E.1: Fit results for the Λ from $\Lambda_c \to \Lambda\pi$ sample, obtained both with the MC sample and with data.

	MC sample	Data sample
N	34.72 ± 0.37	29.36 ± 0.32
f	0.64 ± 0.03	0.61 ± 0.03
μ [MeV/c^2]	2.28658 ± 0.00004	2.28649 ± 0.00005
σ [MeV/c^2]	0.00323 ± 0.00007	0.00358 ± 0.00009
$\Delta\mu$ [MeV/c^2]	-0.00051 ± 0.00021	0.00013 ± 0.00022
σ_{tail} [MeV/c^2]	0.0071 ± 0.0005	0.0073 ± 0.0005
σ_c [MeV/c^2]	0.00785 ± 0.0003	0.00811 ± 0.00003
a	69.87 ± 0.40	48.49 ± 0.35
b	-0.197 ± 0.012	-0.189 ± 0.015

Table E.2: Width (σ_{68}), mass region (MR) and sidebands (S_L, S_R), both for MC and data, obtained from the $p\pi$ invariant mass distributions, and used for the Λ candidates sideband subtraction in Section 8.1.

MC sample			
σ_{68} [MeV/c^2]	MR [MeV/c^2]	S_L [MeV/c^2]	S_R [MeV/c^2]
9.02	(1114.78, 1116.58)	(1110.27, 1111.17)	(1120.19, 1121.09)

Data sample			
σ_{68} [MeV/c^2]	MR [MeV/c^2]	S_L [MeV/c^2]	S_R [MeV/c^2]
10.00	(1114.68, 1116.68)	(1109.68, 1110.68)	(1120.68, 1121.68)

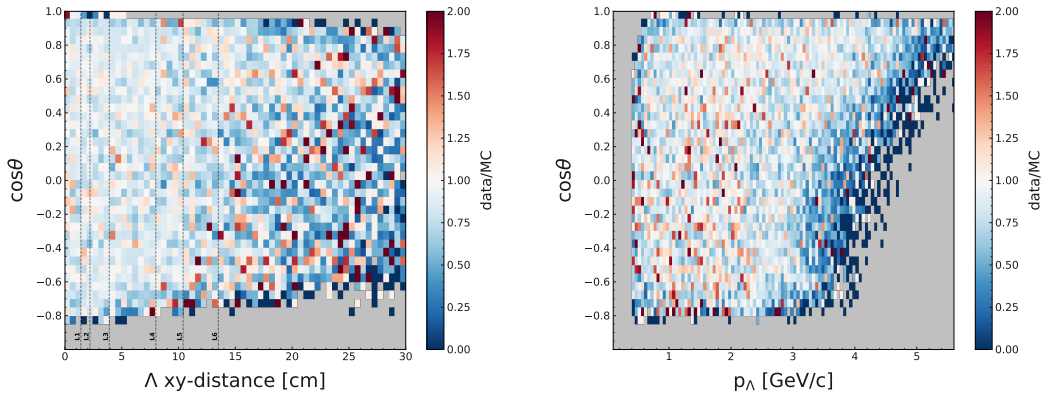

Figure E.1: 2D data-MC ratio. In the left panel, the ratio is shown as a function of the Λ polar angle (y-axis) and its transverse flight distance (x-axis). In the right panel, the ratio is shown as a function of the Λ polar angle (y-axis) and its momentum (x-axis). Red regions of the panels correspond to areas where there is an excess of data with respect to MC. Blue regions correspond to those where there is a lack of data with respect to MC. White regions correspond to those where the data-MC ratio is close to the unity. The background color of the panels has been set to gray in order to distinguish it from the white regions.

E.2 Inclusive Λ sample

Table E.3: Width (σ_{68}), mass region (MR) and sidebands (S_L, S_R), both for MC and data, obtained from the $p\pi$ invariant mass distributions, and used for the Λ candidates sideband subtraction in Section 8.2.

MC sample			
σ_{68} [MeV/c^2]	MR [MeV/c^2]	S_L [MeV/c^2]	S_R [MeV/c^2]
12.97	(1114.39, 1116.98)	(1107.90, 1109.20)	(1122.17, 1123.46)

Data sample			
σ_{68} [MeV/c^2]	MR [MeV/c^2]	S_L [MeV/c^2]	S_R [MeV/c^2]
15.78	(1114.11, 1117.26)	(1106.22, 1107.80)	(1123.57, 1125.15)

Bibliography

[1] S. K. Choi *et al.*, "Observation of a Resonancelike Structure in the $\pi^{+-}\psi'$ Mass Distribution in Exclusive $B \to K\pi^{+-}\psi'$ Decays", *Phys. Rev. Lett.*, vol. 100, p. 142001, 2008.

[2] K. Chilikin *et al.*, "Experimental constraints on the spin and parity of the $Z(4430)^+$", *Phys. Rev. D*, vol. 88, no. 7, p. 074026, 2013.

[3] R. Aaij *et al.*, "Observation of $J/\psi p$ Resonances Consistent with Pentaquark States in $\Lambda_b^0 \to J/\psi K^- p$ Decays", *Phys. Rev. Lett.*, vol. 115, p. 072001, 2015.

[4] E. Fermi, "On the Quantization of the Monoatomic Ideal Gas", 1999, arXiv:cond-mat/9912229.

[5] P. A. M. Dirac, "On the theory of quantum mechanics", *Proceedings of the Royal Society of London. Series A*, vol. 112, no. 762, pp. 661–677, 1926.

[6] W. Pauli, "The Connection Between Spin and Statistics", *Phys. Rev.*, vol. 58, pp. 716–722, Oct 1940.

[7] S. N. Bose, "Planck's law and light quantum hypothesis", *Z. Phys.*, vol. 26, pp. 178–181, 1924.

[8] J. Bernstein, "Spontaneous symmetry breaking, gauge theories, the higgs mechanism and all that", *Rev. Mod. Phys.*, vol. 46, pp. 7–48, 1974, [Erratum: Rev.Mod.Phys. 47, 259–259 (1975), Erratum: Rev.Mod.Phys. 46, 855–855 (1974)].

[9] D. Griffiths, "Introduction to elementary particles", 2008, Wiley.

[10] Wikimedia Commons, Standard model of elementary particles, accessed: 2021-04-10. [Online]. Available: https://en.wikipedia.org/wiki/File:Standard_Model_of_Elementary_Particles.svg

[11] P. Zyla *et al.*, "Review of Particle Physics", *PTEP*, vol. 2020, no. 8, p. 083C01, 2020.

[12] L. D. Faddeev and V. N. Popov, "Feynman Diagrams for the Yang-Mills Field", *Phys. Lett. B*, vol. 25, pp. 29–30, 1967.

[13] D. B. Kaplan, "Effective field theories", in *7th Summer School in Nuclear Physics Symmetries*, 1995, arXiv:nucl-th/9506035.

[14] A. V. Manohar, "Effective field theories", *Lect. Notes Phys.*, vol. 479, pp. 311–362, 1997.

[15] K. G. Wilson, "Confinement of Quarks", *Phys. Rev. D*, vol. 10, pp. 2445–2459, 1974.

[16] D. A. Spade, "Chapter 1 - Markov chain Monte Carlo methods: Theory and practice", in *Principles and Methods for Data Science*. Elsevier, 2020, vol. 43, pp. 1–66.

[17] M. Gell-Mann, "A Schematic Model of Baryons and Mesons", *Phys. Lett.*, vol. 8, pp. 214–215, 1964.

[18] G. Zweig, "An SU(3) model for strong interaction symmetry and its breaking." 1964, CERN Libraries.

[19] N. Brambilla, S. Eidelman, C. Hanhart, A. Nefediev, C.-P. Shen, C. E. Thomas, A. Vairo, and C.-Z. Yuan, "The XYZ states: experimental and theoretical status and perspectives", *Phys. Rept.*, vol. 873, pp. 1–154, 2020.

[20] S. L. Olsen, T. Skwarnicki, and D. Zieminska, "Nonstandard heavy mesons and baryons: Experimental evidence", *Rev. Mod. Phys.*, vol. 90, no. 1, p. 015003, 2018.

[21] N. Brambilla *et al.*, "Heavy Quarkonium: Progress, Puzzles, and Opportunities", *Eur. Phys. J. C*, vol. 71, p. 1534, 2011.

[22] M. B. Voloshin, "Charmonium", *Prog. Part. Nucl. Phys.*, vol. 61, pp. 455–511, 2008.

[23] S. Dubynskiy and M. B. Voloshin, "Hadro-Charmonium", *Phys. Lett. B*, vol. 666, pp. 344–346, 2008.

[24] R. L. Jaffe, "Multi-Quark Hadrons. 1. The Phenomenology of (2 Quark 2 anti-Quark) Mesons", *Phys. Rev. D*, vol. 15, p. 267, 1977.

[25] A. Ali, L. Maiani, and A. D. Polosa, "Multiquark Hadrons", 2019, Cambridge University Press.

[26] F.-K. Guo, C. Hanhart, U.-G. Meißner, Q. Wang, Q. Zhao, and B.-S. Zou, "Hadronic molecules", *Rev. Mod. Phys.*, vol. 90, no. 1, p. 015004, 2018.

[27] B. Aubert *et al.*, "Evidence of a broad structure at an invariant mass of 4.32- GeV/c^2 in the reaction $e^+e^- \to \pi^+\pi^-\psi_{2S}$ measured at BaBar", *Phys. Rev. Lett.*, vol. 98, p. 212001, 2007.

[28] X. L. Wang *et al.*, "Observation of Two Resonant Structures in e+e- to pi+ pi- psi(2S) via Initial State Radiation at Belle", *Phys. Rev. Lett.*, vol. 99, p. 142002, 2007.

[29] S. K. Choi *et al.*, "Observation of a resonance-like structure in the $pi^{\pm}\psi'$ mass distribution in exclusive $B \to K\pi^{\pm}\psi'$ decays", *Phys. Rev. Lett.*, vol. 100, p. 142001, 2008.

[30] M. Anselmino, E. Predazzi, S. Ekelin, S. Fredriksson, and D. B. Lichtenberg, "Diquarks", *Rev. Mod. Phys.*, vol. 65, pp. 1199–1234, 1993.

[31] R. L. Jaffe, "Exotica", *Nucl. Phys. B Proc. Suppl.*, vol. 142, pp. 343–355, 2005.

[32] C. Amsler and N. A. Tornqvist, "Mesons beyond the naive quark model", *Phys. Rept.*, vol. 389, pp. 61–117, 2004.

[33] N. Isgur and J. E. Paton, "A Flux Tube Model for Hadrons in QCD", *Phys. Rev. D*, vol. 31, p. 2910, 1985.

[34] D. Horn and J. Mandula, "A Model of Mesons with Constituent Gluons", *Phys. Rev. D*, vol. 17, p. 898, 1978.

[35] R. L. Jaffe, "Perhaps a Stable Dihyperon", *Phys. Rev. Lett.*, vol. 38, pp. 195–198, 1977, [Erratum: Phys.Rev.Lett. 38, 617 (1977)].

[36] G. R. Farrar, "Stable Sexaquark", 2017, arXiv:1708.08951.

[37] G. R. Farrar, "A stable H dibaryon: Dark matter candidate within QCD?" *Int. J. Theor. Phys.*, vol. 42, pp. 1211–1218, 2003.

[38] J. R. Green, A. D. Hanlon, P. M. Junnarkar, and H. Wittig, "Weakly bound H dibaryon from SU(3)-flavor-symmetric QCD", 2021.

[39] K. Sasaki *et al.*, "$\Lambda\Lambda$ and $N\Xi$ interactions from Lattice QCD near the physical point", *Nucl. Phys. A*, vol. 998, p. 121737, 2020.

[40] S. R. Beane, E. Chang, S. D. Cohen, W. Detmold, H. W. Lin, T. C. Luu, K. Orginos, A. Parreno, M. J. Savage, and A. Walker-Loud, "Light Nuclei

and Hypernuclei from Quantum Chromodynamics in the Limit of SU(3) Flavor Symmetry", *Phys. Rev. D*, vol. 87, no. 3, p. 034506, 2013.

[41] A. Chodos, R. L. Jaffe, K. Johnson, C. B. Thorn, and V. F. Weisskopf, "A New Extended Model of Hadrons", *Phys. Rev. D*, vol. 9, pp. 3471–3495, 1974.

[42] A. T. M. Aerts, P. J. G. Mulders, and J. J. de Swart, "Multi-Baryon States in the Bag Model", *Phys. Rev. D*, vol. 17, p. 260, 1978.

[43] P. J. G. Mulders, A. T. M. Aerts, and J. J. de Swart, "Negative Parity NN Resonances and Extraneous States", *Phys. Rev. Lett.*, vol. 40, p. 1543, 1978.

[44] P. J. Mulders, A. T. M. Aerts, and J. J. De Swart, "Multi - Quark States. 3. Q**6 Dibaryon Resonances", *Phys. Rev. D*, vol. 21, p. 2653, 1980.

[45] P. J. Mulders and A. W. Thomas, "Pionic Corrections and Multi - Quark Bags", *J. Phys. G*, vol. 9, p. 1159, 1983.

[46] K. F. Liu and C. W. Wong, "MIT bag model with center-of-mass correction", *Phys. Lett. B*, vol. 113, pp. 1–5, 1982.

[47] A. T. M. Aerts and C. B. Dover, "On the production of the six quark H dibaryon in the (K-, K+) reaction", *Phys. Rev. D*, vol. 28, pp. 450–463, 1983.

[48] A. P. Balachandran, A. Barducci, F. Lizzi, V. G. J. Rodgers, and A. Stern, "A Doubly Strange Dibaryon in the Chiral Model", *Phys. Rev. Lett.*, vol. 52, p. 887, 1984.

[49] M. Oka, K. Shimizu, and K. Yazaki, "The Dihyperon State in the Quark Cluster Model", *Phys. Lett. B*, vol. 130, pp. 365–368, 1983.

[50] K. Saito, "Masses of the multi-quark states in the bag model with the pion cloud", *Prog. Theor. Phys.*, vol. 72, pp. 674–677, 1984.

[51] K. Maltman, "On the Possibility of Deeply Bound Dibaryon Resonances", *Nucl. Phys. A*, vol. 438, pp. 669–684, 1985.

[52] S. A. Larin, V. A. Matveev, A. A. Ovchinnikov, and A. A. Pivovarov, "Determination of the mass of the Lambda Lambda dibaryon by the method of QCD sum rules", *Sov. J. Nucl. Phys.*, vol. 44, p. 690, 1986.

[53] P. LaFrance and E. L. Lomon, "Six Quark Resonance Structures in Nucleon-nucleon Scattering", *Phys. Rev. D*, vol. 34, p. 1341, 1986.

[54] A. E. Dorokhov and N. I. Kochelev, "Effects of QCD Vacuum and Stability of H Dihyperon", 1986, arXiv:hep-ph/0411362.

[55] M. Oka, "Flavor Octet Dibaryons in the Quark Model", *Phys. Rev. D*, vol. 38, p. 298, 1988.

[56] T. Sakai, K. Shimizu, and K. Yazaki, "H dibaryon", *Prog. Theor. Phys. Suppl.*, vol. 137, pp. 121–145, 2000.

[57] H. Clement, "On the History of Dibaryons and their Final Observation", *Prog. Part. Nucl. Phys.*, vol. 93, p. 195, 2017.

[58] J. L. Rosner, "SU(3) Breaking and the H Dibaryon", *Phys. Rev. D*, vol. 33, p. 2043, 1986.

[59] C. Gignoux, B. Silvestre-Brac, and J. M. Richard, "Possibility of Stable Multi - Quark Baryons", *Phys. Lett. B*, vol. 193, p. 323, 1987.

[60] H. J. Lipkin, "New Possibilities for Exotic Hadrons: Anticharmed Strange Baryons", *Phys. Lett. B*, vol. 195, pp. 484–488, 1987.

[61] S. Takeuchi and M. Oka, "Can the H particle survive instantons?" *Phys. Rev. Lett.*, vol. 66, pp. 1271–1274, 1991.

[62] M. Oka and S. Takeuchi, "Instanton Induced Interaction and the Strange Dibaryons", *Nucl. Phys. A*, vol. 524, pp. 649–667, 1991.

[63] N. Kodama, M. Oka, and T. Hatsuda, "H dibaryon in the QCD sum rule", *Nucl. Phys. A*, vol. 580, pp. 445–454, 1994.

[64] Y. Fujiwara, Y. Suzuki, and C. Nakamoto, "Baryon-baryon interactions in the SU(6) quark model and their applications to light nuclear systems", *Prog. Part. Nucl. Phys.*, vol. 58, pp. 439–520, 2007.

[65] G. Baym, E. W. Kolb, L. D. McLerran, T. P. Walker, and R. L. Jaffe, "Is Cygnus X-3 Strange?" *Phys. Lett. B*, vol. 160, p. 181, 1985.

[66] M. L. Marshak *et al.*, "Evidence for Muon Production by Particles from Cygnus X-3", *Phys. Rev. Lett.*, vol. 54, p. 2079, 1985.

[67] S. Bashinsky and R. L. Jaffe, "Quark states near a threshold and the unstable H dibaryon", *Nucl. Phys. A*, vol. 625, pp. 167–191, 1997.

[68] R. L. Jaffe and F. E. Low, "The Connection Between Quark Model Eigenstates and Low-Energy Scattering", *Phys. Rev. D*, vol. 19, pp. 2105–2118, 1979.

[69] N. I. Kochelev, "Ultrahigh-energy cosmic rays and stable H-dibaryon", *JETP Lett.*, vol. 70, pp. 491–494, 1999.

[70] W. J. Marciano and H. Pagels, "Quantum Chromodynamics: A Review", *Phys. Rept.*, vol. 36, p. 137, 1978.

[71] A. E. Dorokhov, Y. A. Zubov, and N. I. Kochelev, "Manifestations of QCD vacuum structure in composite quark models", *Sov. J. Part. Nucl.*, vol. 23, pp. 522–551, 1992.

[72] E. V. Shuryak and J. L. Rosner, "Instantons and Baryon Mass Splittings", *Phys. Lett. B*, vol. 218, pp. 72–74, 1989.

[73] V. A. Kuzmin and I. I. Tkachev, "Ultra-high-energy cosmic rays and inflation relics", *Physics Reports*, vol. 320, no. 1-6, p. 199–221, 1999.

[74] K. Greisen, "End to the cosmic ray spectrum?" *Phys. Rev. Lett.*, vol. 16, pp. 748–750, 1966.

[75] G. R. Farrar and G. Zaharijas, "Transitions of two baryons to the H dibaryon in nuclei", 2003, arXiv:hep-ph/0303047.

[76] G. R. Farrar, "A precision test of the nature of Dark Matter and a probe of the QCD phase transition", 2018, arXiv:1805.03723.

[77] G. R. Farrar and G. Zaharijas, "Nuclear and nucleon transitions of the H dibaryon", *Physical Review D*, vol. 70, no. 1, 2004.

[78] Y. Fukuda *et al.*, "The Super-Kamiokande detector", *Nucl. Instrum. Meth. A*, vol. 501, pp. 418–462, 2003.

[79] H. R. Gustafson, C. A. Ayre, L. W. Jones, M. J. Longo, and P. V. Ramana Murthy, "Search for New Massive Long-lived Neutral Particles", *Phys. Rev. Lett.*, vol. 37, p. 474, 1976.

[80] C. Gross, A. Polosa, A. Strumia, A. Urbano, and W. Xue, "Dark Matter in the Standard Model?" *Phys. Rev. D*, vol. 98, no. 6, p. 063005, 2018.

[81] E. W. Kolb and M. S. Turner, "Dibaryons cannot be the dark matter", *Phys. Rev. D*, vol. 99, no. 6, p. 063519, 2019.

[82] S. D. McDermott, S. Reddy, and S. Sen, "Deeply bound dibaryon is incompatible with neutron stars and supernovae", *Phys. Rev. D*, vol. 99, no. 3, p. 035013, 2019.

[83] Y. Iwasaki, T. Yoshie, and Y. Tsuboi, "The H Dibaryon in Lattice QCD", *Phys. Rev. Lett.*, vol. 60, pp. 1371–1374, 1988.

[84] Z.-H. Luo, M. Loan, and X.-Q. Luo, "H-dibaryon from lattice QCD with improved anisotropic actions", *Mod. Phys. Lett. A*, vol. 22, pp. 591–597, 2007.

[85] Z.-H. Luo, M. Loan, and Y. Liu, "Search for H dibaryon on the lattice", *Phys. Rev. D*, vol. 84, p. 034502, 2011.

[86] P. B. Mackenzie and H. B. Thacker, "Evidence Against a Stable Dibaryon from Lattice QCD", *Phys. Rev. Lett.*, vol. 55, p. 2539, 1985.

[87] A. Pochinsky, J. W. Negele, and B. Scarlet, "Lattice study of the H dibaryon", *Nucl. Phys. B Proc. Suppl.*, vol. 73, pp. 255–257, 1999.

[88] I. Wetzorke, F. Karsch, and E. Laermann, "Further evidence for an unstable H dibaryon?" *Nucl. Phys. B Proc. Suppl.*, vol. 83, pp. 218–220, 2000.

[89] I. Wetzorke and F. Karsch, "The H dibaryon on the lattice", *Nucl. Phys. B Proc. Suppl.*, vol. 119, pp. 278–280, 2003.

[90] M. Luscher, "Volume Dependence of the Energy Spectrum in Massive Quantum Field Theories. 2. Scattering States", *Commun. Math. Phys.*, vol. 105, pp. 153–188, 1986.

[91] M. Luscher, "Two particle states on a torus and their relation to the scattering matrix", *Nucl. Phys. B*, vol. 354, pp. 531–578, 1991.

[92] N. Ishii, S. Aoki, and T. Hatsuda, "The Nuclear Force from Lattice QCD", *Phys. Rev. Lett.*, vol. 99, p. 022001, 2007.

[93] S. Aoki, T. Hatsuda, and N. Ishii, "Theoretical Foundation of the Nuclear Force in QCD and its applications to Central and Tensor Forces in Quenched Lattice QCD Simulations", *Prog. Theor. Phys.*, vol. 123, pp. 89–128, 2010.

[94] S. Aoki, T. Doi, T. Hatsuda, Y. Ikeda, T. Inoue, N. Ishii, K. Murano, H. Nemura, and K. Sasaki, "Lattice QCD approach to Nuclear Physics", *PTEP*, vol. 2012, p. 01A105, 2012.

[95] S. R. Beane *et al.*, "Evidence for a Bound H-dibaryon from Lattice QCD", *Phys. Rev. Lett.*, vol. 106, p. 162001, 2011.

[96] S. R. Beane *et al.*, "Present Constraints on the H-dibaryon at the Physical Point from Lattice QCD", *Mod. Phys. Lett. A*, vol. 26, pp. 2587–2595, 2011.

[97] S. R. Beane, E. Chang, W. Detmold, H. W. Lin, T. C. Luu, K. Orginos, A. Parreno, M. J. Savage, A. Torok, and A. Walker-Loud, "The Deuteron and Exotic Two-Body Bound States from Lattice QCD", *Phys. Rev. D*, vol. 85, p. 054511, 2012.

[98] A. Francis, J. R. Green, P. M. Junnarkar, C. Miao, T. D. Rae, and H. Wittig, "Lattice QCD study of the H dibaryon using hexaquark and two-baryon interpolators", *Phys. Rev. D*, vol. 99, no. 7, p. 074505, 2019.

[99] T. Inoue, N. Ishii, S. Aoki, T. Doi, T. Hatsuda, Y. Ikeda, K. Murano, H. Nemura, and K. Sasaki, "Baryon-Baryon Interactions in the Flavor SU(3) Limit from Full QCD Simulations on the Lattice", *Prog. Theor. Phys.*, vol. 124, pp. 591–603, 2010.

[100] T. Inoue, N. Ishii, S. Aoki, T. Doi, T. Hatsuda, Y. Ikeda, K. Murano, H. Nemura, and K. Sasaki, "Bound H-dibaryon in Flavor SU(3) Limit of Lattice QCD", *Phys. Rev. Lett.*, vol. 106, p. 162002, 2011.

[101] T. Inoue, S. Aoki, T. Doi, T. Hatsuda, Y. Ikeda, N. Ishii, K. Murano, H. Nemura, and K. Sasaki, "Two-Baryon Potentials and H-Dibaryon from 3-flavor Lattice QCD Simulations", *Nucl. Phys. A*, vol. 881, pp. 28–43, 2012.

[102] S. Paul, "The H dibaryon in experimental physics", *Nucl. Phys. B Proc. Suppl.*, vol. 21, pp. 243–253, 1991.

[103] H. Takahashi *et al.*, "Observation of a (Lambda Lambda)He-6 double hypernucleus", *Phys. Rev. Lett.*, vol. 87, p. 212502, 2001.

[104] K. Nakazawa, "Double-Lambda hypernuclei via the Xi- hyperon capture at rest reaction in a hybrid emulsion", *Nucl. Phys. A*, vol. 835, pp. 207–214, 2010.

[105] J. K. Ahn *et al.*, "Enhanced ΛΛproduction near threshold in the C-12(K-,K+) reaction", *Phys. Lett. B*, vol. 444, pp. 267–272, 1998.

[106] C. J. Yoon *et al.*, "Search for the H-dibaryon resonance in C-12 (K-, K+ ΛΛX)", *Phys. Rev. C*, vol. 75, p. 022201, 2007.

[107] R. W. Stotzer *et al.*, "Search for H dibaryon in He-3 (K^-, K^+) Hn", *Phys. Rev. Lett.*, vol. 78, pp. 3646–3649, 1997.

[108] A. J. Bevan *et al.*, "The Physics of the B Factories", *Eur. Phys. J. C*, vol. 74, p. 3026, 2014.

[109] B. H. Kim *et al.*, "Search for an H-dibaryon with mass near $2m_\Lambda$ in $\Upsilon(1S)$ and $\Upsilon(2S)$ decays", *Phys. Rev. Lett.*, vol. 110, no. 22, p. 222002, 2013.

[110] H. Albrecht *et al.*, "Study of Anti-deuteron Production in e^+e^- Annihilation at 10-GeV Center-of-mass Energy", *Phys. Lett. B*, vol. 236, pp. 102–108, 1990.

[111] D. M. Asner *et al.*, "Anti-deuteron production in $\Upsilon(nS)$ decays and the nearby continuum", *Phys. Rev. D*, vol. 75, p. 012009, 2007.

[112] J. P. Lees *et al.*, "Search for a Stable Six-Quark State at BABAR", *Phys. Rev. Lett.*, vol. 122, no. 7, p. 072002, 2019.

[113] L. Adamczyk *et al.*, "ΛΛ Correlation Function in Au+Au collisions at $\sqrt{s_{NN}} = 200$ GeV", *Phys. Rev. Lett.*, vol. 114, no. 2, p. 022301, 2015.

[114] K. Morita, T. Furumoto, and A. Ohnishi, "ΛΛ interaction from relativistic heavy-ion collisions", *Phys. Rev. C*, vol. 91, no. 2, p. 024916, 2015.

[115] A. Ohnishi, K. Morita, K. Miyahara, and T. Hyodo, "Hadron–hadron correlation and interaction from heavy–ion collisions", *Nucl. Phys. A*, vol. 954, pp. 294–307, 2016.

[116] J. Adam *et al.*, "Search for weakly decaying $\overline{\Lambda n}$ and ΛΛ exotic bound states in central Pb-Pb collisions at $\sqrt{s_{\rm NN}} = 2.76$ TeV", *Phys. Lett. B*, vol. 752, pp. 267–277, 2016.

[117] Belle II Collaboration, Belle II official website, accessed: 2021-06-29. [Online]. Available: https://www.belle2.org/

[118] Belle Collaboration, Belle official website, accessed: 2021-06-29. [Online]. Available: https://belle.kek.jp/

[119] BaBar Collaboration, BaBar official website, accessed: 2021-06-29. [Online]. Available: https://www-public.slac.stanford.edu/babar/

[120] Y. Ohnishi *et al.*, "Accelerator design at SuperKEKB", *PTEP*, vol. 2013, p. 03A011, 2013.

[121] T. Abe *et al.*, "Belle II Technical Design Report", 2010, arXiv:1011.0352.

[122] K. Akai, K. Furukawa, and H. Koiso, "SuperKEKB Collider", *Nucl. Instrum. Meth. A*, vol. 907, pp. 188–199, 2018.

[123] KEK, High Energy Accelerator Research Organization, KEK official website, accessed: 2021-06-29. [Online]. Available: https://www.kek.jp/en/

[124] W. Altmannshofer *et al.*, "The Belle II Physics Book", *PTEP*, vol. 2019, no. 12, p. 123C01, 2019, [Erratum: PTEP 2020, 029201 (2020)].

[125] S. Kurokawa and E. Kikutani, "Overview of the KEKB accelerators", *Nucl. Instrum. Meth. A*, vol. 499, pp. 1–7, 2003.

[126] M. Bona *et al.*, "SuperB: A High-Luminosity Asymmetric e+ e- Super Flavor Factory. Conceptual Design Report", 2007, arXiv:0709.0451.

[127] N. Braun, A. Glazov, F. Metzer, and E. Paoloni, "Study of the collision point properties", Belle II internal note, 2018.

[128] P. M. Lewis *et al.*, "First Measurements of Beam Backgrounds at SuperKEKB", *Nucl. Instrum. Meth. A*, vol. 914, pp. 69–144, 2019.

[129] A. Abashian *et al.*, "The Belle Detector", *Nucl. Instrum. Meth. A*, vol. 479, pp. 117–232, 2002.

[130] J. Kemmer and G. Lutz, "New detector concepts", *Nucl. Instrum. Meth. A*, vol. 253, pp. 365–377, 1987.

[131] A. Campbell *et al.*, "The PXD Whitebook", Belle II internal reference (not available online).

[132] B. Spruck *et al.*, "Belle II Pixel Detector Commissioning and Operational Experience", *PoS*, vol. Vertex2019, p. 015, 2020.

[133] V. Bertacchi *et al.*, "Track finding at Belle II", *Comput. Phys. Commun.*, vol. 259, p. 107610, 2021.

[134] M. J. French *et al.*, "Design and results from the APV25, a deep sub-micron CMOS front-end chip for the CMS tracker", *Nucl. Instrum. Meth. A*, vol. 466, pp. 359–365, 2001.

[135] S. Chatrchyan *et al.*, "The CMS Experiment at the CERN LHC", *JINST*, vol. 3, p. S08004, 2008.

[136] M. Akatsu *et al.*, "Time of propagation Cherenkov counter for particle identification", *Nucl. Instrum. Meth. A*, vol. 440, pp. 124–135, 2000.

[137] V. Aulchenko *et al.*, "Electromagnetic calorimeter for Belle II", *J. Phys. Conf. Ser.*, vol. 587, no. 1, p. 012045, 2015.

[138] H. Ikeda *et al.*, "A detailed test of the CsI(Tl) calorimeter for BELLE with photon beams of energy between 20-MeV and 5.4-GeV", *Nucl. Instrum. Meth. A*, vol. 441, pp. 401–426, 2000.

[139] D. J. Lange, "The EvtGen particle decay simulation package", *Nucl. Instrum. Meth. A*, vol. 462, pp. 152–155, 2001.

[140] J. F. Krohn *et al.*, "Global decay chain vertex fitting at Belle II", *Nucl. Instrum. Meth. A*, vol. 976, p. 164269, 2020.

[141] The Belle II Collaboration, basf2 - Belle II Analysis Software Framework, accessed: 2021-08-02. [Online]. Available: https://stash.desy.de/projects/B2/repos/basf2/browse

[142] P. Billoir, "Progressive track recognition with a Kalman like fitting procedure", *Comput. Phys. Commun.*, vol. 57, pp. 390–394, 1989.

[143] T. Bilka *et al.*, "Implementation of GENFIT2 as an experiment independent track-fitting framework", 2019, arXiv:1902.04405.

[144] T. Alexopoulos, M. Bachtis, E. Gazis, and G. Tsipolitis, "Implementation of the Legendre Transform for track segment reconstruction in drift tube chambers", *Nucl. Instrum. Meth. A*, vol. 592, pp. 456–462, 2008.

[145] A. Glazov, I. Kisel, E. Konotopskaya, and G. Ososkov, "Filtering tracks in discrete detectors using a cellular automaton", *Nucl. Instrum. Meth. A*, vol. 329, pp. 262–268, 1993.

[146] T. Keck, "FastBDT: A Speed-Optimized Multivariate Classification Algorithm for the Belle II Experiment", *Comput. Softw. Big Sci.*, vol. 1, no. 1, p. 2, 2017.

[147] R. B. Leighton, S. D. Wanlass, and C. D. Anderson, "The Decay of V^0 Particles", *Phys. Rev.*, vol. 89, pp. 148–167, 1953.

[148] B. Scavino, "Lambda reconstruction at Belle II", Belle II internal note, 2020.

[149] B. Scavino, "Sensitivity studies of $\Upsilon(3S) \to S\Lambda\Lambda\, n\pi_s$ using early phase III Monte Carlo", Belle II internal note, 2021.

[150] S. Agostinelli *et al.*, "GEANT4–a simulation toolkit", *Nucl. Instrum. Meth. A*, vol. 506, pp. 250–303, 2003.

[151] G. Punzi, "Sensitivity of searches for new signals and its optimization", *eConf*, vol. C030908, p. MODT002, 2003.

[152] F. Zernike, "Beugungstheorie des Schneidenverfahrens und seiner verbesserten Form, der Phasenkontrastmethode", *Physica*, vol. 1, no. 7, pp. 689–704, 1934.

[153] S. D. Biller and S. M. Oser, "Another Look at Confidence Intervals: Proposal for a More Relevant and Transparent Approach", *Nucl. Instrum. Meth. A*, vol. 774, pp. 103–119, 2015.

[154] U. Tamponi, Private Comunication.

[155] S. Dreyer, T. Ferber, A. Gaz, B. Scavino, and U. Tamponi, "Displaced vertex reconstruction at Belle II", Belle II internal note, 2020.

[156] L. Rizzuto, "Λ_c reconstruction in 5.15 fb^{-1} of early Phase 3 Belle II data", Belle II internal note, 2020.

[157] A. Natochii, S. E. Vahsen, H. Nakayama, T. Ishibashi, and S. Terui, "Improved simulation of beam backgrounds and collimation at SuperKEKB", *Phys. Rev. Accel. Beams*, vol. 24, no. 8, p. 081001, 2021.